

U.S. DEPARTMENT OF COMMERCE  
National Technical Information Service

AD-A024 496

AN INVESTIGATION OF MECHANISMS OF INITIATION  
OF LASER-SUPPORTED ABSORPTION (LSA) WAVES

BATTELLE COLUMBUS LABORATORIES

PREPARED FOR  
ARMY MISSILE COMMAND

SEPTEMBER 1975

Reproduced From  
Best Available Copy

20000726054

REPRODUCED BY  
**NATIONAL TECHNICAL  
INFORMATION SERVICE**  
U.S. DEPARTMENT OF COMMERCE  
SPRINGFIELD, VA 22151

UNCLASSIFIED

SECURITY CLASSIFICATION OF THIS PAGE (When Data Entered)

REPORT DOCUMENTATION PAGE		READ INSTRUCTIONS BEFORE COMPLETING FORM
1. REPORT NUMBER	2. GOVT ACCESSION NO.	3. RECIPIENT'S CATALOG NUMBER
4. TITLE (and Subtitle) An Investigation of Mechanisms of Initiation of Laser-Supported Absorption (LSA) Waves		5. TYPE OF REPORT & PERIOD COVERED Final April 23, 1973-August 15, 1975
7. AUTHOR(s) C. T. Walters, R. H. Barnes, and R. E. Beverly		6. PERFORMING ORG. REPORT NUMBER
9. PERFORMING ORGANIZATION NAME AND ADDRESS Battelle Columbus Laboratories 505 King Avenue, Columbus, Ohio 43201		8. CONTRACT OR GRANT NUMBER(s) DAAH01-73-C-0776
11. CONTROLLING OFFICE NAME AND ADDRESS ARPA 1400 Wilson Boulevard Arlington, Virginia		10. PROGRAM ELEMENT, PROJECT, TASK AREA & WORK UNIT NUMBERS 62301E, ARPA-A02113, 2E20, 003D1
14. MONITORING AGENCY NAME & ADDRESS (if different from Controlling Office) U. S. Army Missile Command Redstone Arsenal, Alabama 35809		12. REPORT DATE September, 1975
		13. NUMBER OF PAGES
		15. SECURITY CLASS. (of this report) Unclassified
		15a. DECLASSIFICATION/DOWNGRADING SCHEDULE
16. DISTRIBUTION STATEMENT (of this Report) Distribution of this document is unlimited.		
17. DISTRIBUTION STATEMENT (of the abstract entered in Block 20, if different from Report)		
18. SUPPLEMENTARY NOTES		
19. KEY WORDS (Continue on reverse side if necessary and identify by block number) Laser-Supported Absorption Waves      Surface Physics Laser-Supported Detonation Waves      Plasma Diagnostics Plasma Production      Thermionic Emission Self-Shielding      TEA CO <sub>2</sub> Laser Effects Laser Interaction with Materials		
20. ABSTRACT (Continue on reverse side if necessary and identify by block number) Results of a 2-year study of initiation of laser-supported detonation (LSD) waves on solid surfaces in air are reported. Experimental measurements utilizing target emission, plasma probe, photographic, spectroscopic, and sample examination techniques were performed to isolate mechanisms of LSD-wave initiation on metals having practical surfaces. Metals studied included aluminum 2024 alloy, tungsten, lead, copper, and zinc. The experimental data confirm an initiation mechanism operative at 10.6 $\mu$ laser wavelength wherein (Continued)		

UNCLASSIFIED

SECURITY CLASSIFICATION OF THIS PAGE (When Data Entered)

electrons are emitted from the surface by thermionic or field emission at surface defects and serve as priming electrons for an air breakdown which proceeds via inverse bremsstrahlung heating. Results are also presented for nonmetallic initiation studies wherein three modes of initiation were isolated; initiation at local surface debris sites (believed to be sites of imbedded metallic debris), initiation in the vapor, initiation at metalized surface features. The first measurements of pressure response of targets to 10.6  $\mu$  TEA laser pulses are also reported. The direct effects of initiation of LSD waves on material response and a comparison of experimental data with blast wave theory are discussed.

ii

UNCLASSIFIED

SECURITY CLASSIFICATION OF THIS PAGE (When Data Entered)

## TABLE OF CONTENTS

	<u>Page</u>
SUMMARY. . . . .	1
ACKNOWLEDGEMENT. . . . .	3
INTRODUCTION . . . . .	4
LSD-WAVE INITIATION ON METALLIC SURFACES . . . . .	6
Theoretical Models of Initiation of LSD-Waves on Metallic Surfaces. . . . .	11
Surface Heating. . . . .	13
Air Breakdown by Priming Electrons . . . . .	20
Correlation of the Simple Model with Experimental Data for LSD-Wave Initiation Times. . . . .	22
Linkup of LSD Waves. . . . .	25
Measurement of LSD-Wave Initiation Times on Metals. . . . .	25
Spectroscopic Studies of LSD-Wave Initiation on Metallic Surfaces . . . . .	31
Time-Integrated Measurements . . . . .	32
Time-Resolved Measurements . . . . .	37
Conclusions Drawn from the Spectroscopy Experiments, . . . . .	45
Initiation of LSD-Waves on Aluminum Alloy at 1.06 Micron. . . . .	46
LSD-WAVE INITIATION ON NONMETALLICS. . . . .	51
LSD-Wave Initiation Time for Cellulose Acetate . . . . .	54
Debris Initiation on Nonmetallics. . . . .	55
PRESSURE RESPONSE MEASUREMENTS . . . . .	60
Description of the Experimental Configuration . . . . .	61
Laser Beam Parameters . . . . .	63
Gauge Package Designs . . . . .	65
Pressure Response of Aluminum Targets . . . . .	69
Pressure Response of Plastic Targets. . . . .	79
LSD-Wave Initiation Times on Metallic and Nonmetallic Surfaces. . . . .	86
CONCLUSIONS AND RECOMMENDATIONS. . . . .	91
LSD-Wave Initiation on Metallics. . . . .	91
LSD-Wave Initiation on Nonmetallics . . . . .	93
LSD-Wave Induced Pressure Response. . . . .	93
REFERENCES . . . . .	95
APPENDIX A . . . . .	A-1

# LIST OF TABLES

	<u>Page</u>
TABLE 1. HANDBOOK METAL PROPERTY DATA. . . . .	30
TABLE 2. PROMINENT EMISSION LINES OBSERVED IN TIME-INTEGRATED SPECTRA NEAR 3000 Å . . . . .	34
TABLE 3. PROMINENT EMISSION LINES OBSERVED IN TIME-INTEGRATED SPECTRA NEAR 4000 Å . . . . .	35
TABLE 4. INTENSITY THRESHOLD LINES AT 2800 Å . . . . .	36
TABLE 5. APPROXIMATE LSD-WAVE THRESHOLDS FOR NONMETALLIC MATERIALS .	52
TABLE 6. MATERIAL COMPOSITION AND PROPERTIES FOR QUARTZ AND CARBON GAUGE PACKAGES. . . . .	67

# LIST OF FIGURES

FIGURE 1. LSD-WAVE INITIATION TIMES ON ALUMINUM 2024 ALLOY FOR 10.6 μ TEA LASER PULSES . . . . .	8
FIGURE 2. STREAK AND FRAMING RECORDS FOR LSD-WAVE INITIATION ON ALUMINUM 2024 ALLOY AT 10.6 μ . . . . .	9
FIGURE 3. SCHEMATIC REPRESENTATION OF TYPICAL SURFACE DEFECTS . . .	14
FIGURE 4. COMPARISON OF ALUMINUM SURFACE THERMAL RESPONSE AS CALCULATED BY THE DEFECT AND BULK HEATING MODELS. . . . .	17
FIGURE 5. PREDICTED TIME TO ACHIEVE VAPORIZATION WITH PULSES HAVING A LINEAR RISE TO A CONSTANT LEVEL. . . . .	19
FIGURE 6. INVERSE BREMSSTRAHLUNG ABSORPTION COEFFICIENT FOR NORMAL DENSITY AIR. . . . .	21
FIGURE 7. ELECTRON DENSITY GROWTH IN NORMAL DENSITY AIR . . . . .	23
FIGURE 8. INITIATION TIMES FOR ALUMINUM IN NORMAL DENSITY AIR AT 10.6 μ . . . . .	24
FIGURE 9. INITIATION TIMES FOR ALUMINUM IN NORMAL DENSITY AIR AT 1.06 μ . . . . .	26

# LIST OF FIGURES

	<u>Page</u>
FIGURE 10. SCHEMATIC REPRESENTATION OF THE LINKUP PROCESS. . . . .	27
FIGURE 11. LSD-WAVE INITIATION TIMES MEASURED FOR VARIOUS METALS IN NORMAL DENSITY AIR. . . . .	29
FIGURE 12. RADIATION INTENSITIES FOR BREMSSTRAHLUNG AND N I LINE AT 3994.86 Å AT SURFACE OF ALUMINUM TARGET IN NITROGEN . . . . .	38
FIGURE 13. RADIATION INTENSITIES FOR BREMSSTRAHLUNG AND N II LINE AT 3006.83 Å AT SURFACE OF ALUMINUM TARGET IN NITROGEN . . . . .	39
FIGURE 14. RADIATION INTENSITIES FOR BREMSSTRAHLUNG AND He I LINES AT SURFACE OF ALUMINUM TARGET IN HELIUM . . . . .	40
FIGURE 15. RADIATION INTENSITIES FOR BREMSSTRAHLUNG AND Al I LINES AT SURFACE OF ALUMINUM TARGET IN NITROGEN . . . . .	41
FIGURE 16. RADIATION INTENSITIES FOR BREMSSTRAHLUNG AND Al III LINE AT 4150 Å AT SURFACE OF ALUMINUM TARGET IN NITROGEN. . . . .	42
FIGURE 17. RADIATION INTENSITIES FOR BREMSSTRAHLUNG AND Cu I LINE AT 3247.54 Å AT SURFACE OF ALUMINUM TARGET IN NITROGEN. . . . .	43
FIGURE 18. RADIATION INTENSITIES FOR BREMSSTRAHLUNG AND SPECTRAL LINE AT 2803 Å AT SURFACE OF ALUMINUM TARGET IN NITROGEN. . . . .	44
FIGURE 19. LASER PULSE HISTORIES FOR THE 1.06 μ and 10.6 μ LASERS. .	47
FIGURE 20. TARGET ELECTRON EMISSION RECORDS FOR ALUMINUM 2024 AT 1.06 μ . . . . .	48
FIGURE 21. NOMARSKI MICROGRAPH OF DAMAGE SITES ON POLISH N-TYPE SILICON (1.3 ohm-cm) IRRADIATED AT $3.2 \times 10^8$ watt/cm <sup>2</sup> . .	53
FIGURE 22. PEAK PRECURSOR SIGNAL ON ELECTROSTATIC PROBE. . . . .	56
FIGURE 23. NOMARSKI MICROGRAPHS OF LSD-WAVE INITIATION SITES ON ACRYLIC SURFACES IRRADIATED AT $2.1 \times 10^8$ watt/cm <sup>2</sup> . . . .	57
FIGURE 24. EXPERIMENTAL ARRANGEMENT FOR MEASUREMENT OF LASER- INDUCED SHOCK PRESSURES . . . . .	62

# LIST OF FIGURES (Continued)

	<u>Page</u>
FIGURE 25. BLOCK DIAGRAM OF THE ELECTRONIC CIRCUITRY EMPLOYED WITH THE CARBON PIEZORESISTIVE GAUGE MEASUREMENTS. . . .	64
FIGURE 26. OSCILLOSCOPE TRIGGER DELAY AS A FUNCTION OF PEAK POWER DENSITY ON TARGET. . . . .	66
FIGURE 27. QUARTZ PIEZOELECTRIC GAUGE ASSEMBLED GAUGE PACKAGES WITH ALUMINUM TARGETS. . . . .	68
FIGURE 28. ASSEMBLED CARBON PIEZORESISTIVE GAUGE PACKAGES . . . . .	68
FIGURE 29. REPRESENTATIVE PRESSURE HISTORIES WITH ALUMINUM TARGETS AND CARBON GAUGE PACKAGES FOR $G_p = 3.48 \times 10^8$ watt/cm <sup>2</sup> AND AMBIENT PRESSURES OF (a) 760, (b) 125, (c) 40, and (d) 2 Torr . . . . .	70
FIGURE 30. REPRESENTATIVE PRESSURE HISTORIES WITH ALUMINUM TARGETS AND QUARTZ GAUGE PACKAGES FOR $G_p = 3.48 \times 10^8$ watt/cm <sup>2</sup> ABOVE (10 Torr) AND BELOW (2 torr) THE AMBIENT PRESSURE THRESHOLD FOR LSD-WAVE INITIATION . . . . .	72
FIGURE 31. PEAK SHOCK PRESSURES IN ALUMINUM AS A FUNCTION OF AMBIENT PRESSURE FOR $G_p = 1.39 \times 10^8$ watt/cm <sup>2</sup> (a) AND $G_p = 3.48 \times 10^8$ watt/cm <sup>2</sup> (b) . . . . .	73
FIGURE 32. PEAK SHOCK PRESSURE IN ALUMINUM AS A FUNCTION OF TARGET RADIUS (CARBON GAUGE DATA) . . . . .	76
FIGURE 33. ARRIVAL TIME OF THE PEAK COMPRESSIONAL WAVE IN ALUMINUM AS A FUNCTION OF TARGET RADIUS (CARBON GAUGE DATA) . . . .	78
FIGURE 34. REPRESENTATIVE PRESSURE HISTORIES WITH PLASTIC TARGETS AND CARBON GAUGE PACKAGES. . . . .	80
FIGURE 35. COMPARISON OF GAUGE RESPONSE WITH CELLULOSE ACETATE TARGETS. . . . .	82
FIGURE 36. PEAK SHOCK PRESSURE IN CELLULOSE ACETATE AND PMMA AS A FUNCTION OF AMBIENT PRESSURE FOR $G_p = 1.39 \times 10^8$ watt/cm <sup>2</sup> AND $G_p = 3.48 \times 10^8$ watt/cm <sup>2</sup> . . . . .	84
FIGURE 37. PEAK SHOCK PRESSURE IN CELLULOSE ACETATE AS A FUNCTION OF PEAK POWER DENSITY FOR AN AMBIENT PRESSURE OF 760 Torr .	85
FIGURE 38. PEAK SHOCK PRESSURE IN CELLULOSE ACETATE AS A FUNCTION OF THE NUMBER OF SHOTS (CARBON GAUGE DATA). . . . .	87



LIST OF FIGURES (Continued)

	<u>Page</u>
FIGURE 39. INITIATION TIME FOR ALUMINUM TARGETS AS A FUNCTION OF PEAK POWER DENSITY AND AMBIENT PRESSURE AS INFERRED FROM QUARTZ GAUGE MEASUREMENTS. . . . .	88
FIGURE 40. INITIATION TIME FOR PLASTIC TARGETS AS A FUNCTION OF PEAK POWER DENSITY AND AMBIENT PRESSURE AS INFERRED FROM QUARTZ AND CARBON GAUGE MEASUREMENTS . . .	89

## SUMMARY

This report presents results of experimental effort undertaken in the study of the initiation of laser-supported absorption (LSA) waves on solid surfaces irradiated in air with pulsed laser radiation. LSA waves may be classified as either supersonic, so-called laser-supported detonation (LSD) waves, or as subsonic, so-called laser-supported combustion (LSC) waves. In either case, a hot-air plasma (1-2 eV) is formed which propagates back up in the laser beam away from the target surface and absorbs most of the laser-beam energy. The objective of this study was to provide an improved understanding of the process of LSA wave initiation. The experiments dealt exclusively with initiation of LSD waves; however, diagnostic techniques developed and experimental results obtained may be applicable to the LSC initiation problem.

During the first year of study, experiments were directed toward understanding the mechanisms of initiation of LSD waves produced on practical aluminum surfaces in air with the Battelle 80-joule TEA CO<sub>2</sub> laser. Results indicated that the initiation occurred at a large number of local surface features (laminae and pits) on a very rapid time scale (20-60 nsec). Thermionic emission at these surface features followed by air breakdown was found to be a viable mechanism for initiation of the local LSD-wave plasmas. Initial studies of nonmetallic LSD-wave initiation showed that the initiation process is also local for "first shot" irradiations of acrylic plastic and fused silica.

During the second year of research, the universality of the electron emission mechanism was investigated in experimental studies of initiation at the 10.6- $\mu$  wavelength on additional metallic materials having practical surfaces, including tungsten, lead, copper, and zinc. Electron emission and prompt (<100 nsec) initiation times for LSD-waves were observed for all metals investigated. Time-integrated and time-resolved emission spectroscopy studies were conducted which yielded

results consistent with the electron emission mechanism. A limited number of experiments were conducted with 1.06- $\mu$  laser pulses incident on practical aluminum surfaces in normal density air. Results of these experiments indicated that LSD-wave initiation at 1.06  $\mu$  occurs by breakdown of the metal vapor. A simplified theoretical model was developed to estimate LSD-wave initiation times on metals for both laser wavelengths. The model includes the effects of defect and bulk metal heating and air breakdown processes. Theoretical predictions and experimental results for LSD-wave initiation times on aluminum were found to be in good agreement for the 10.6  $\mu$  case.

Additional experimental studies of LSD-wave initiation on non-metallic materials at 10.6  $\mu$  were conducted during the second year. Three distinct modes of initiation were observed for the materials investigated. Acrylic plastic, fused silica, and polyimide were found to initiate at local sites on the surface believed to be sites of embedded metallic debris particles. Purposely embedded aluminum particles in acrylic plastic were found to produce this type of initiation. Vapor breakdown was found to dominate initiation on cellulose acetate, phenolic resin, and alumina. Initiation on polished silicon was found to be similar to that occurring on a polished metal surface.

Also during the second year, an extensive series of pressure response measurements were performed to directly assess the effects of LSD-wave initiation on response of metals and plastics to 10.6  $\mu$  radiation in normal and reduced pressure air. Metallic response was found to be dominated by the LSD-wave/blast-wave pressures above the air pressure threshold for initiation of LSD-waves. Reasonable agreement of the pressure data with blast-wave theory predictions was obtained when variations from ideal irradiance conditions and the local initiation phenomenon were considered. Pressures recorded for the cellulose acetate samples were an order of magnitude higher than those observed for aluminum as expected for a vaporization-dominated response. Initiation of an LSD wave was found to reduce the peak shock pressure in this case, presumably by blockage of laser radiation and resultant reduction in vaporization.

#### ACKNOWLEDGEMENT

The authors wish to gratefully acknowledge the excellent technical assistance of Warren B. Nicholson in the laser irradiations and diagnostic instrumentation, and Charles C. Moeller in the spectroscopy experiments.

AN INVESTIGATION OF MECHANISMS OF INITIATION  
OF LASER-SUPPORTED ABSORPTION (LSA) WAVES

by

C. T. Walters, R. H. Barnes, and R. E. Beverly, III

I - INTRODUCTION

This is the final technical report of an experimental investigation of initiation of laser-supported absorption (LSA) waves in gases in front of solid surfaces. Contract efforts were limited to experimental study of initiation of absorption waves generated by short pulses, i.e., laser-supported detonation (LSD) waves; however, results may be applicable to laser-supported combustion (LSC) waves in some cases. During the first year, (1,2)\* extensive studies of initiation of LSD waves in air in front of practical aluminum surfaces with TEA CO<sub>2</sub> laser pulses revealed a viable mechanism of initiation. The experimental data were found to be consistent with inverse-bremsstrahlung heating of surface-emitted priming electrons in the air. Thermionic or field emission at surface features such as pits and laminae is believed to be the process for production of priming electrons for the air breakdown. During the second year of research, the universality of this mechanism was studied in experiments designed to reveal initiation mechanisms on a variety of metallic and nonmetallic materials. Metallic materials studied included aluminum, titanium, tungsten, copper, stainless steel, lead, and zinc. Nonmetallic materials included acrylic plastic, fused silica, cellulose acetate, phenolic resin, polyimide, and silicon. Initial results of LSD-wave initiation experiments with some of these materials were presented in the last semiannual report. (3) Results of more recent experiments with metallic materials and a review of theoretical models for metallic initiation processes are presented in Section II of this report. Section III presents additional experimental results for nonmetallic LSD-wave initiation. In addition to the

---

\* References are listed on page 95.

initiation experiments, pressure measurements were performed in air and partial vacuum to directly assess the effects of the LSD-induced blast wave on metallic and nonmetallic target response to the TEA-laser pulse. Results of these experiments and a correlation with theory are presented in Section IV. Section V summarizes conclusions which may be drawn from the research and recommendations for future areas of investigation.

## II - LSD-WAVE INITIATION ON METALLIC SURFACES

The phenomenology of laser-supported detonation (LSD) waves propagating in air and other gases and been known for some time;<sup>(4-6)</sup> however, only in the past few years have the mechanisms of initiation of these waves on solid surfaces come under intense experimental investigation.<sup>(1-3)</sup> Several mechanisms which might be involved in the initiation process have been proposed. These mechanisms include

- Uniform target vaporization
- Metal oxide vapor absorption
- Chemical reaction
- Thermionic emission
- Planar reflection-enhanced fields
- Local target heating
- Contaminant and gas desorption
- Field emission
- Shock heating of the air by cold vapor piston
- Nonequilibrium ionization of vapor
- Defect-enhanced fields
- Shock heating of air by front surface spalled layer.
- Vaporization of impurity dielectric layer.

Uniform vaporization followed by equilibrium vapor heating was first considered by Nielson and Canavan<sup>(7)</sup> and was found by them to be inconsistent with the experimental data for initiation thresholds for aluminum and tungsten. By assuming resonance absorption in the vapor species (AlO) of the normally present aluminum oxide coating, better agreement was achieved in the case of aluminum. Several additional mechanisms were proposed by Walter,<sup>(8)</sup> which included chemical reaction of the aluminum vapor with the oxygen, thermionic emission of priming electrons, and the local electric field enhancement resulting from the reflected wave. Local plasma phenomena were observed in experiments at Battelle<sup>(9)</sup> and local target heating at surface defects was proposed. Hall<sup>(10)</sup> proposed a mechanism wherein blown-off

contaminants or desorbed gases could initiate a plasma. Additional mechanisms suggested by others included field emission in the enhanced normal component of electric field at surface protrusions,<sup>(11)</sup> shock heating of the air via a cold vapor piston expansion,<sup>(12)</sup> and electric field enhancement in the air by concentrated reflection in the vicinity of surface defects.<sup>(13)</sup>

More recently some initiation mechanisms have been suggested in the published literature. These mechanisms include shock heating of the air by a thin layer of molten metal which is spalled from the front surface<sup>(14)</sup> and heating of a vaporized impurity dielectric layer.<sup>(15)</sup>

To some extent, several of the above mechanisms may be operative or dominant in various regimes of laser beam parameters which initiate LSD waves on metals. However, research conducted during the first year of the contract shortened considerably the list of mechanisms applicable to the restricted case of LSD initiation on practical aluminum surfaces in normal density air at  $10.6\ \mu$  with a TEA-laser pulse shape.<sup>(1)</sup> The concept of uniform vaporization of target material and heating in the vapor was found invalid under the conditions studied because measured plasma initiation times (30-60 nsec) were found to be an order of magnitude shorter than calculated bulk vaporization times. Results of the initiation timing measurements performed using different techniques are presented in Figure 1. The data follow a curve corresponding to constant energy deposition prior to breakdown (dashed curve) rather than one corresponding to the time required to achieve a constant (critical) power density (solid curve). This implies that the initiation process may depend upon heating a small amount of material (such as a lamination-type surface defect) to a critical temperature. Furthermore, local initiation was observed photographically as illustrated in Figure 2. In this figure, plasma initiation on an aluminum surface is viewed from the surface normal with simultaneous streak and framing photography. The beam is at  $45^\circ$  incidence from the right. The slit orientation is indicated by the dark line in the framing photographs which are sequenced from top to bottom. Figure 2(a) shows the luminosity for peak intensity



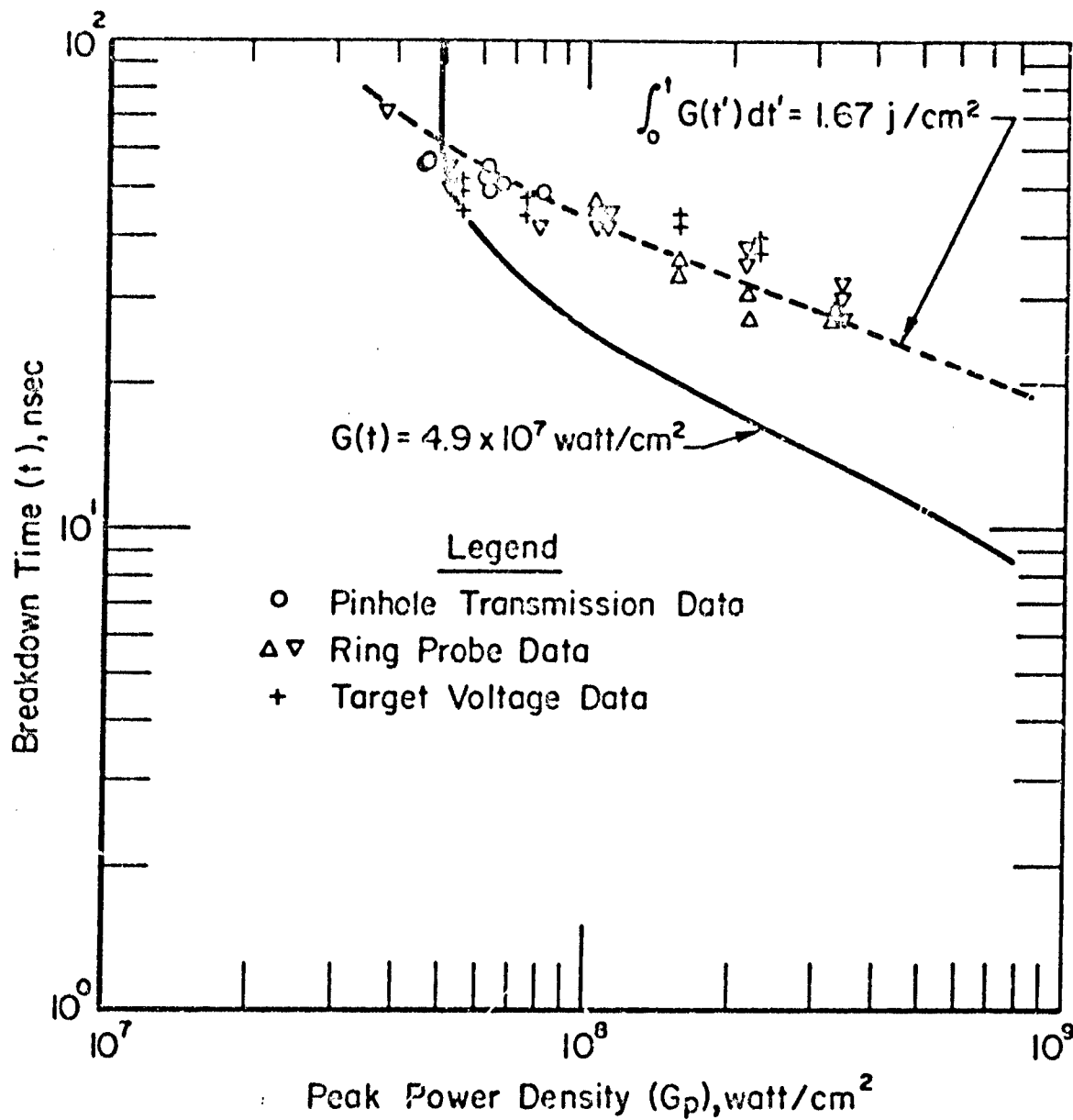
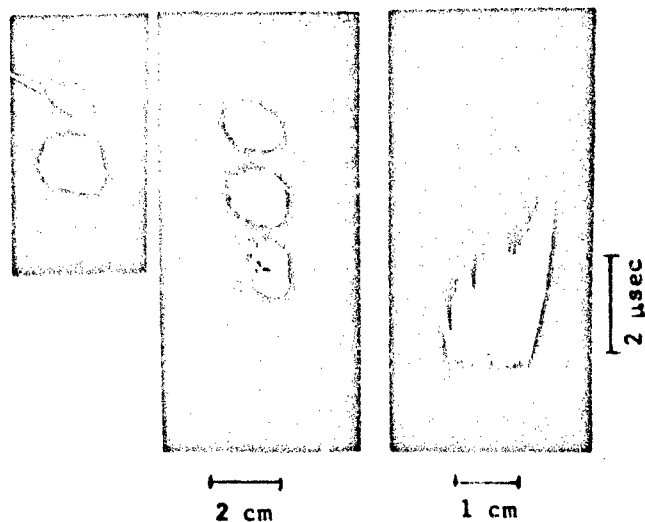
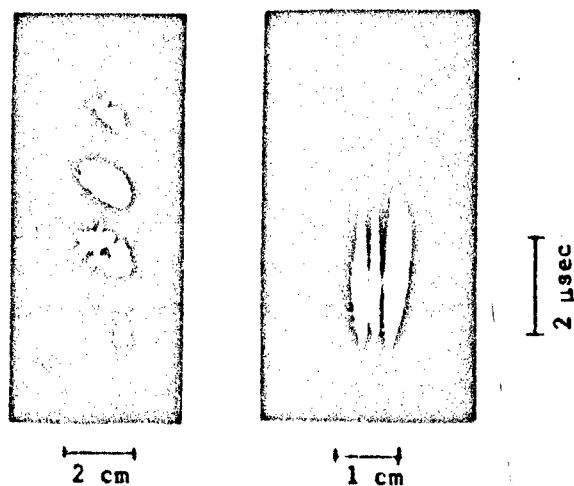


FIGURE 1. LSD-WAVE INITIATION TIMES ON ALUMINUM 2024 ALLOY FOR  $10.6 \mu$  TEA LASER PULSES



(a) Framing and Streak Photographs Viewing Normal to the Surface ( $\theta_i = 45$  degrees,  $G_p = 7.1 \times 10^7$  watt/cm<sup>2</sup>, frame separation =  $1.8 \mu$ sec)



(b) Framing and Streak Photographs Viewing Normal to the Surface ( $\theta_i = 45$  degrees,  $G_p = 3.4 \times 10^7$  watt/cm<sup>2</sup>, frame separation =  $1.8 \mu$ sec)

FIGURE 2. STREAK AND FRAMING RECORDS FOR LSD-WAVE INITIATION ON ALUMINUM 2024 ALLOY AT  $10.6 \mu$  (LASER INCIDENT FROM RIGHT)

well above threshold ( $G_p = 7.1 \times 10^7$  watt/cm<sup>2</sup>), and of particular interest are the numerous individual luminosity sites within the slit image area. These are believed to be individual initiation sites for waves which join up to form a front which moves off to the right, the direction of beam incidence. For comparison, Figure 2(b) shows the same arrangement with the beam attenuated to provide a peak intensity below LSD-wave initiation threshold ( $G_p = 3.4 \times 10^7$  watt/cm<sup>2</sup>). From the streak photograph, it is evident that only one or two plasma fronts initiated in or near the slit image area and these did not move up the beam. Postirradiation examination of targets with the scanning electron microscope (SEM) showed numerous isolated damage sites associated with surface features.

Resonance absorption in the AlO vapor layer was found to be unimportant when it was observed that LSD waves are easily generated on a practical aluminum surface freshly coated with pure aluminum and irradiated in pure nitrogen. This result is in agreement with Maher et al.<sup>(16)</sup> who found no effect of aluminum oxide layer thickness (20-2000 Å) on LSD-wave initiation threshold. Initiation experiments performed in pure nitrogen also revealed that chemical reactions of vapor with oxygen play no significant role. Irradiations of freshly deposited aluminum surfaces and other "clean surface" experiments demonstrated that contaminants are not essential to LSD-wave initiation, although it is obvious that they can affect the process. No experiments were conducted which could isolate the effects of gas desorption; however, absorption of the laser radiation by the desorbed layer is believed to be insufficient to initiate the plasma on the observed time scale. The fact that aluminum is highly reflective at 10.6  $\mu$  gives rise to an enhanced electric field at planes of constructive interference between the incident and reflected wave. This results in a lowering of the clean-air breakdown threshold by a factor of four for planar reflection and perhaps more near surface defects. While this effect most likely dominates initiation at peak power densities greater than  $6 \times 10^8$  watt/cm<sup>2</sup>, it was not found to be significant in the lower intensity regime studied. It should be noted that the reflected component would be reduced considerably over the hot surface associated with a local surface defect. The notion of shocking the air

up to plasma temperatures by the cold vapor or a spalled layer appears to be inconsistent with the observed short initiation times. An apparent error in the assumed radiation absorption depth in Reference (14) calls into question the possibility of front surface spallation in this case.

The observation of local plasma initiation and target electron emission in irradiations of practical aluminum surfaces at  $10.6 \mu^{(1)}$  was found to be consistent with surface defect heating and associated emission of priming electrons either by thermionic or high field emission processes. However, it was also shown in a detailed one-dimensional calculation by Edwards et al.<sup>(17)</sup> that if the initial absorptance of the aluminum surface were adjusted to a value of 0.10, initiation on the observed time scale could occur by a nonequilibrium breakdown in the vapor and subsequent shock heating of the air by hot vapor ions. Further, their results of two-dimensional calculations revealed that initiation can occur at a  $10\text{-}\mu$ -diameter initiation site on a surface. These being the likely initiation mechanisms operative at  $10.6 \mu$ , additional experimental effort was devoted to determining their role in initiating LSD waves on practical aluminum surfaces and other metals of interest possessing differing physical properties. The following subsections present an outline of the theoretical modeling of the initiation process and additional experimental results for metallic surfaces.

#### Theoretical Models of Initiation of LSD Waves on Metallic Surfaces

Theoretical modeling of the initiation of LSD waves on metallic surfaces has been reported by Walters and Barnes,<sup>(1)</sup> Thomas and Musal,<sup>(18-21)</sup> and Edwards et al.<sup>(17)</sup> In Reference (1) it was shown that surface defects could heat to temperatures at which thermionic emission of electrons would be expected on a time scale consistent with observed initiation times. It was further shown that the electrons would diffuse into the air a distance of the order of the Debye length and provide a local priming electron density near the surface of the order of  $10^{14}$  electrons/cm<sup>3</sup>. This priming density was believed to be sufficient to cause cascade breakdown in the air within

the observed initiation times. This assumption will be substantiated subsequently. The thermionic emission model was developed further by Thomas and Musal<sup>(21)</sup> and excellent agreement was achieved with our initiation time data over a range of peak power densities. This agreement was achieved with only one adjustable parameter,  $d$ , the characteristic thickness of the model lamination defect. The value of  $d$  providing a good fit was  $d = 3 \times 10^{-5}$  cm, a value consistent with sample examination data.

In earlier work, Thomas and Musal<sup>(19)</sup> also developed the field emission model of LSD-wave initiation, in which a protrusion-type defect with a height-to-diameter ratio of 10 to 1 is found to create sufficient enhancement of the normal component of the laser radiation electric field (at  $45^\circ$  beam incidence angles) to cause field emission of electrons. These electrons may be directly accelerated to energies sufficient to ionize air molecules or may serve as priming electrons for a breakdown in a manner similar to the case of thermionically emitted electrons. In the initial form of the model<sup>(19)</sup> they predicted a very strong dependence of the initiation time on peak power density which yielded agreement with the experimental data only at high peak power densities ( $2 \times 10^8$  watt/cm<sup>2</sup>). More recently, inclusion of protrusion heating in the model<sup>(21)</sup> has permitted a better fit to the experimentally measured initiation times. Other experiments, however, tend to rule out field emission as a dominating mechanism. Because the normal component of electric field is predominantly the component inducing field emission at a protrusion, an anomalous effect would be expected wherein a lower threshold for initiation would occur at off-normal incidence than for normal incidence. This anomalous effect was not observed in experiments conducted with practical aluminum surfaces.<sup>(1)</sup> Furthermore, the extent to which the high aspect-ratio protrusions must be present on a surface for LSD-wave initiation is inconsistent with our scanning electron microscope (SEM) examination of samples. Attempts to resolve the issue regarding the nature of the emitted electrons are reported in Reference (3). In these experiments, emitted electron energies were measured in vacuum; however, the strong background of electrons apparently resulting from plasma-u.v.-induced target-photoemission made the results inconclusive with respect to the origin of priming electrons.

As noted previously, a detailed calculation of the initiation and propagation of LSD waves has been performed by Edwards et al.<sup>(17)</sup> Computer calculations were performed using the computer code LASNEX which accounted for detailed aluminum and air equations-of-state, hydrodynamics, energy exchange between plasma components, thermal energy transport, thermal radiation transport, and laser radiation transport. No electron emission from the surface was assumed. The electron population was determined from a detailed equilibrium ionization model. In calculations with electrons and ions in equilibrium (for both the air and the metal vapor), initiation of an LSD wave in air was not achieved with the TEA laser pulse at  $7 \times 10^7$  watt/cm<sup>2</sup> peak power density. However, when the electron temperature was allowed to separate from the ion temperature, an LSD wave was initiated following breakdown of the metal vapor. By adjusting the initial laser radiation absorptance to a value of 0.10, an LSD-wave initiation time was calculated which was in agreement with our experimental value. While this mechanism appears to be viable, no evidence of breakdown in the aluminum vapor for atmospheric pressure irradiations has been observed in extensive time-integrated and time-resolved spectroscopic experiments with 10.6- $\mu$  TEA laser pulses. For longer pulse rise times and shorter laser wavelengths, breakdown in the metal vapor may dominate the thermionic emission mechanism as will be discussed subsequently.

The following subsections present a brief discussion of the various phases of the LSD-initiation process for aluminum and relevant simple theoretical results which may be used to correlate experimental data.

#### Surface Heating

Simple models for surface heating by the laser radiation can be utilized to yield approximate times to achieve emitting and vaporization temperatures at surface defects and for bulk material. From extensive examination of SEM data on target samples before and after irradiation, lamination-and pit-type defects were found to be the most common potential initiation sites on practical aluminum surfaces. Figure 3 presents a



(a) Lamination Defect (b) Lamination Defect  
(before irradiation) (after irradiation)



(c) Pit Defect (d) Pit Defect  
(before irradiation) (after irradiation)

FIGURE 3. SCHEMATIC REPRESENTATION OF TYPICAL SURFACE DEFECTS

schematic representation of these types of defects. In both cases, a layer of material is thermally isolated from the bulk material and can heat quite rapidly relative to the normal surface which is cooled by conduction. A characteristic thickness,  $d$ , can be ascribed to the defect layer to permit simple calculations of thermal response. While a distribution of such thicknesses exists, a value of  $10^{-4} - 10^{-5}$  cm appears to be consistent with SEM data. It is important to note that the defect model is still valid on second and subsequent shots on a surface although less emitting area is available. This latter effect is consistent with the observation of less emission current on second shots and offers an explanation for the "cleanup effect" wherein the initiation threshold is raised slightly on second and subsequent shots on a practical surface. For the purposes of estimating heating times, a simple one-dimensional isolated layer of thickness  $d$  is assumed in the defect calculations that follow.

The temperature rise at a surface with constant properties and constant heat input is easily calculated.<sup>(22)</sup> For a semi-infinite region the surface temperature rise is

$$\Delta T = \left[ \frac{4}{\pi k \rho C_p} \right]^{\frac{1}{2}} \alpha G t^{\frac{1}{2}}, \quad (1)$$

where  $k$  is thermal conductivity,  $\rho$  is density,  $C_p$  is specific heat,  $\alpha$  is absorptance,  $G$  is power density, and  $t$  is time. For constant power density heating of a finite region (defect) of thickness  $d$  the surface temperature rise is simply

$$\Delta T = \frac{1}{\rho C_p d} \alpha G t, \quad (2)$$

provided  $d \ll [kt/\rho C_p]^{\frac{1}{2}}$  for the times of interest. This condition holds for the postulated defects and they may be assumed to be isothermal. For a linearly rising incident power density with rate of increase  $\dot{G}$ , the surface temperature rise is

$$\Delta T = \left[ \frac{16 \alpha^2}{9 \pi k \rho C_p} \right]^{\frac{1}{2}} \dot{G} t^{\frac{3}{2}}. \quad (3)$$



For the same rising power density incident on a finite layer of thickness  $d$ ,

$$\Delta T = \frac{\alpha G}{2 \rho C_p d} t^2 \quad (4)$$

Values of thermal properties for aluminum 2024 alloy used in the calculations were  $\rho = 2.7 \text{ gm/cm}^3$ ,  $C_p = .9 \text{ J/gm}$ , and  $k = 1.6 \text{ watt/cm C}$ . The melt temperature and vaporization temperature were assumed to be 660 C and 2520 C, respectively. The laser radiation absorptance,  $\alpha$ , was found experimentally to be 0.029 at room temperature and 10.6  $\mu$ . This value was used for the bulk material and was assumed to be constant up to the melt temperature. A value of 0.05 was used for a defect layer below the melt temperature. Data on metallic reflection above the melt point are sparse;<sup>(23)</sup> however, absorption values are believed to increase with temperature after a jump increase at the melt point. An assumption of a high average value over the melt region is believed to be more realistic than using the room-temperature value. A value of 0.48 for absorptance was found by Bergel'son et al.<sup>(24)</sup> to provide good agreement of their theoretical response model with experimental impulse data at 1.06  $\mu$ . This value was used for the present calculations at 10.6  $\mu$  and 1.06  $\mu$  above the melt temperature. Below the melt temperature,  $\alpha = 0.12$  was used for both defect and bulk heating at 1.06  $\mu$ .

Figure 4 presents representative surface heating curves for a peak incident power density of  $10^8 \text{ watt/cm}^2$  at 10.6- $\mu$  and 1.06- $\mu$  wavelengths for a TEA laser pulse shape (40-nsec risetime) calculated using the simple models for defect and bulk material response. At 10.6  $\mu$  it is noted that the bulk surface temperature does not reach the melt temperature while the defect temperature rises to emitting and vaporization levels within 30 nsec. This is consistent with the observation of negligible surface damage at 10.6  $\mu$ . At 1.06  $\mu$ , both the defect and bulk surface temperature reach vaporization levels prior to the pulse maximum at  $10^8 \text{ watt/cm}^2$  peak power density, which is also consistent with experiment as will be shown subsequently. It should also be noted that under the assumptions of the model most of the time prior to vaporization is accounted for by the time required to reach the melt temperature.

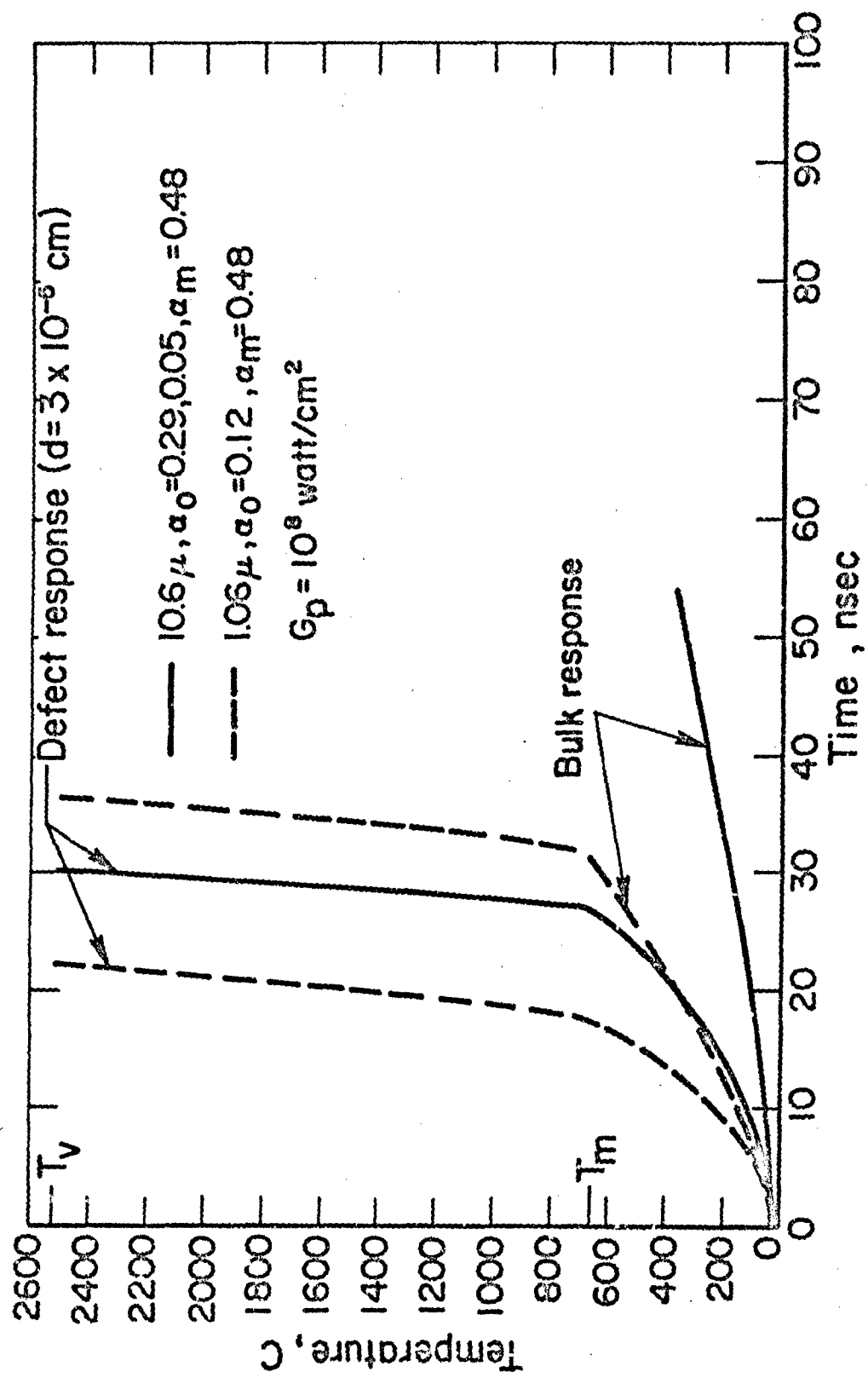


FIGURE 4. COMPARISON OF ALUMINUM SURFACE THERMAL RESPONSE AS CALCULATED BY THE DEFECT AND BULK HEATING MODELS

To illustrate the thermal effects over a broader range of conditions, the time to reach the vaporization temperature is presented in Figure 5 as function of peak power density for pulse shapes which rise linearly for a period  $\tau$  to the peak value and remain constant thereafter. Results for both models are presented for  $10.6 \mu$  (solid curves) and  $1.06 \mu$  (dashed curves) with values of  $\tau = 40, 400, \text{ and } 2500 \text{ nsec}$ . The four power-law dependencies which are given by Equations (1)-(4) are revealed by the four limiting slopes of the curves appearing in the figure. Only the regime of peak power densities greater than  $10^6 \text{ watt/cm}^2$  is shown in the figure. Below  $10^6 \text{ watt/cm}^2$  initiation times have been correlated very well with the vaporization time calculated with a bulk material heating model.<sup>(21)</sup> While the times calculated using the defect model are orders of magnitude less than those calculated with the bulk heating model in this region, at some point lateral conduction in the defect layer invalidates the one-dimensional defect heating assumption and the model does not apply. If lateral dimensions of the order of  $3 \times 10^{-4} \text{ cm}$  are assumed, then at times greater than a few hundred nanoseconds (for aluminum defects), the defects can lose heat by conduction and the initiation process becomes dominated by bulk heating effects. As can be seen in the figure, this leads to breakdown of the defect model for peak power densities less than about  $3 \times 10^6 \text{ watt/cm}^2$  and a transition to bulk heating occurs. A transition curve has been drawn schematically in the figure for the  $10.6 \mu$  case. Also noted in the figure is the important effect of pulse risetime on surface heating. It is this effect which is likely responsible for considerable differences in initiation times and thresholds reported by investigators using different laser devices. It should also be noted that for the 40-nsec risetime case at  $1.06 \mu$ , little difference between bulk and defect vaporization times is predicted and, in fact, at  $10^9 \text{ watt/cm}^2$  the defect heat transfer becomes conduction limited (crossover point).

While the times discussed above are those required to reach vaporization, it is clear from Figure 4 that the times required to reach thermionic emitting temperatures are not much different. In the following subsection, the additional time required to breakdown the air is estimated so that the total time for plasma initiation can be correlated with experimental data.

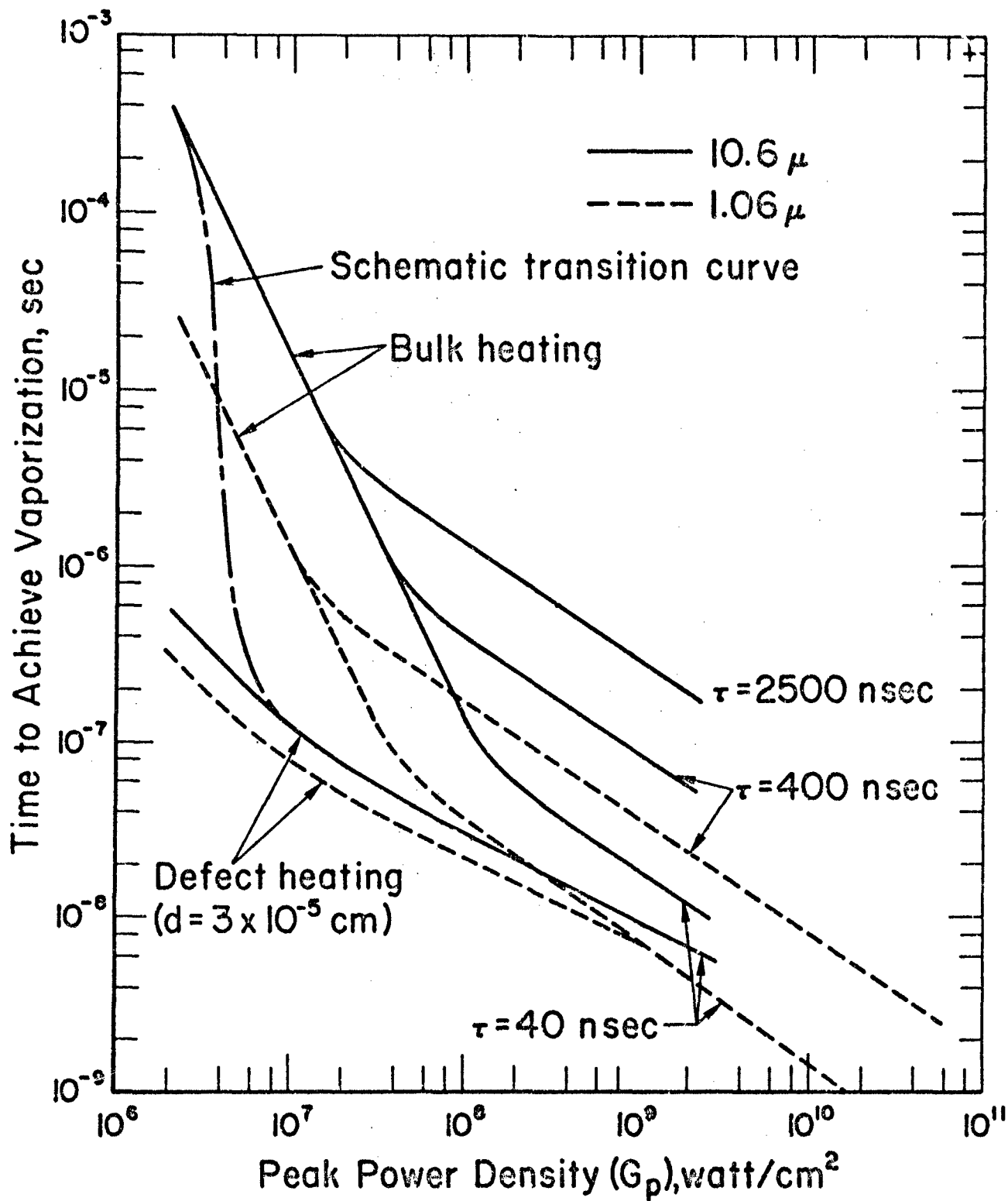


FIGURE 5. PREDICTED TIME TO ACHIEVE VAPORIZATION WITH PULSES HAVING A LINEAR RISE TO A CONSTANT LEVEL

### Air Breakdown by Priming Electrons

In Reference (1), it was shown that thermionic emission of electrons from an aluminum surface into normal density air could result in a significant buildup of free electron density in an air layer having a thickness of the order of the Debye length. The electron density was of the order of  $10^{13}$  to  $10^{15} \text{ cm}^{-3}$  depending on the work function selected and the surface temperature. These electrons are heated via the inverse bremsstrahlung mechanism in the field of neutral and ionized atoms. Estimates of heating times have been made using the absorption coefficient used in LASNEX<sup>(17)</sup> with the exception that a Gaunt factor of 1.0 and only singly ionized species are assumed for the ion component. This results in the coefficient

$$K = 2.61 \times 10^{-41} \left( \frac{Rd}{h\nu} \right)^3 \left( \frac{Rd}{kT_e} \right)^{\frac{1}{2}} \left[ 1 - \exp \left( -\frac{h\nu}{kT_e} \right) \right] \\ \times \left[ n_e^2 + n_e n_a \langle Z^2 g \rangle \right] \text{ cm}^{-1}, \quad (5)$$

where  $Rd = 13.59 \text{ eV}$ ,  $h\nu$  is the laser photon energy in eV,  $kT_e$  is the electron temperature in eV,  $n_e$  is electron density in  $\text{cm}^{-3}$ ,  $n_a$  is the neutral atom density in  $\text{cm}^{-3}$ , and  $\langle Z^2 g \rangle$  is tabulated in Reference (17) for various  $kT_e$ . The reduced absorption coefficient,  $K/n_e$ , is presented in Figure 6 as a function of electron temperature. A differential equation for growth of the electron density at constant power density can be written for the case where all of the absorbed energy goes into ionization and heating of electrons.

$$\frac{1}{n_e} \frac{dn_e}{dt} = \frac{K G_0}{n_e \left( \frac{3}{2} kT_e + I \right) \left[ 1 + 3 \left( \frac{kT_e}{\frac{3}{2} kT_e + I} \right)^2 \right]}, \quad (6)$$

where  $G_0$  is a constant power density and  $I$  is the effective ionization potential of air, assumed to be 14 eV. Since the temperatures reached in the breakdown are of order 1-2 eV, it is a good approximation to let

$$\frac{1}{n_e} \frac{dn_e}{dt} = \frac{K G_0}{n_e I}, \quad (7)$$

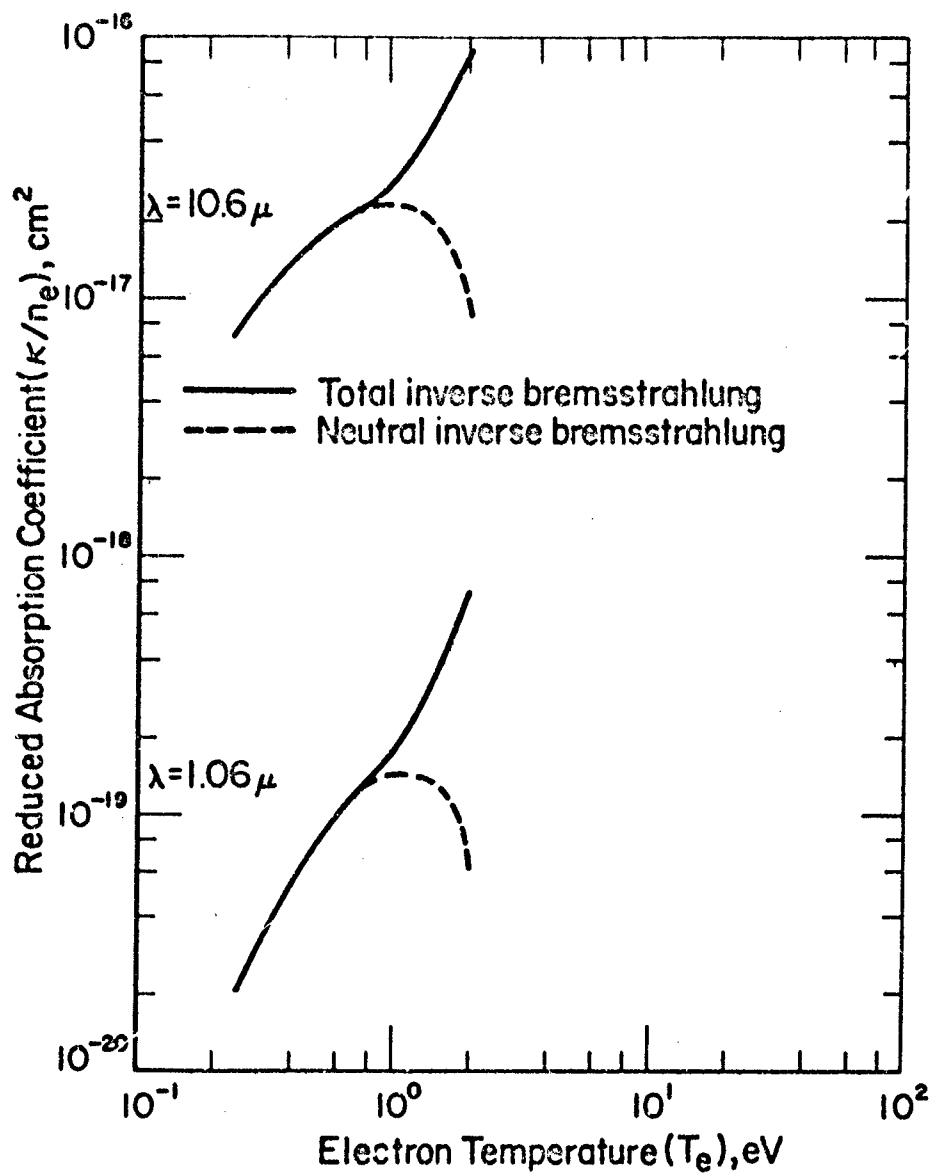


FIGURE 6. INVERSE BREMSSTRAHLUNG ABSORPTION  
COEFFICIENT FOR NORMAL DENSITY AIR

which simply says that almost all of the absorbed energy is used to ionize the gas. Using Equation (5) and assuming Saha equilibrium, Equation (7) was integrated numerically. Results for 1.06- and 10.6- $\mu$  laser wavelengths are presented in Figure 7 for an initial electron temperature of 0.25 eV. The quantitative results should not be taken as being rigorous because of the gross assumptions of the model. Departures from a Maxwellian energy distribution and the Saha equilibrium and the loss of energy by several mechanisms are known to occur. The results do show, however, the very rapid breakdown of the air which occurs for priming electron densities of order  $10^{14}$   $\text{cm}^{-3}$ . Also noted is some departure from exact  $\lambda^2$  wavelength scaling of absorption which apparently occurs because of a significant stimulated emission component at 1.06  $\mu$ .

#### Correlation of the Simple Model with Experimental Data for LSD-Wave Initiation Times

Results of the simple model have been used to predict LSD initiation times for various pulse risetimes assuming the initiation time to be the sum of the time required to achieve emitting temperatures and the time for the electron density in air to go from  $10^{14}$  to  $10^{18}$   $\text{cm}^{-3}$ . These results are presented in Figure 8 for aluminum at 10.6  $\mu$  in normal density air. As was found by Thomas and Husal,<sup>(21)</sup> the model for thermionic emission at a lamination defect yields very good agreement with the experimental values measured at Battelle with aluminum. The observed small disagreement is within the error inherent in the model. Very few additional data have been found on LSD-wave initiation times. Maher et al.<sup>(16)</sup> report initiation near the peak of their laser pulse (0.5  $\mu\text{sec}$ ) when the intensity is well above threshold. Barchukov et al.<sup>(15)</sup> report initiation on magnesium in the range 0.5-1.5  $\mu\text{sec}$  for their slowly-rising pulse. They note an approximate inverse relationship between initiation time and peak power density. The unadjusted data for magnesium have been plotted although corresponding values of initiation time for aluminum would be about a factor of two higher. Even with these corrections, the data appear to be well below the bulk heating predictions as is the case for the data of Maher et al. This

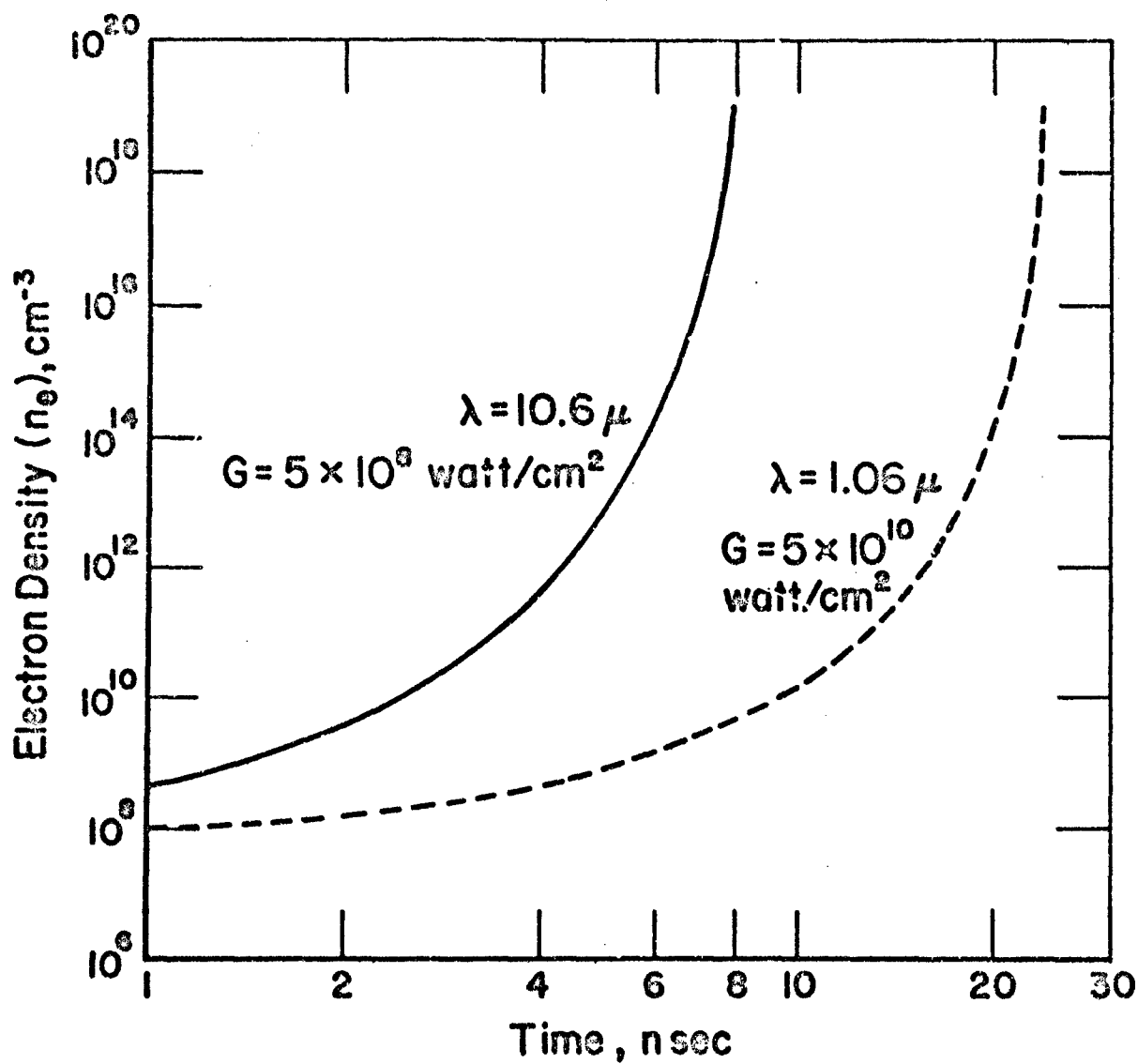


FIGURE 7. ELECTRON DENSITY GROWTH IN NORMAL DENSITY AIR



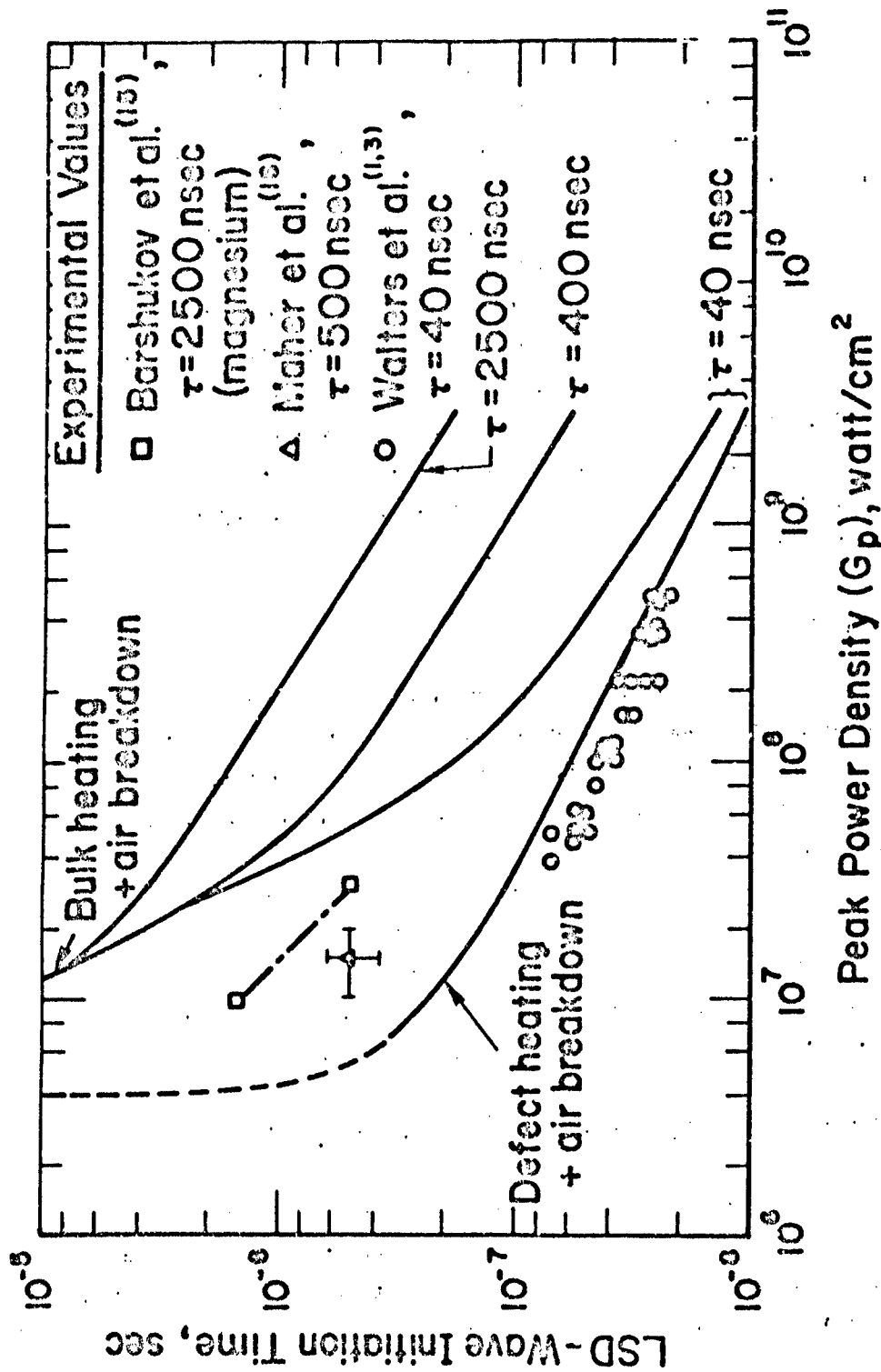


FIGURE 8. INITIATION TIMES FOR ALUMINUM IN  
NORMAL DENSITY AIR AT 10.6  $\mu$

discrepancy may result from operation in the regime of transition from defect heating to bulk heating. Initiation data in this regime should be particularly sensitive to the first-shot "cleanup effect" as has been noted in Reference (16).

Similar results for aluminum at  $1.06 \mu$  are presented in Figure 9. The two data points are from the work of Rudder<sup>(25)</sup> and our work discussed in a subsequent section of this report. Since the times to vaporization in defects and in the bulk are about the same and both very much less than the air breakdown time, no effect of the heating model is observed in the theoretical predictions. The experimental values are substantially lower than predictions based on breaking down the air by priming electrons. As will be discussed in a subsequent section, breakdown in the vapor is believed responsible for initiation at  $1.06 \mu$ .

#### Linkup of LSD Waves

The models for LSD-wave initiation discussed in the previous sections apply to the very early stages of the initiation process when 1-2 eV plasmas are first formed in the air. At  $10.6 \mu$ , these miniature LSD waves do not cover the surface, but exist only at the defect initiation sites. An exhaustive theory of LSD initiation should account for the propagation and growth of the miniature LSD waves and the "linkup" process wherein they merge to form a continuous front which completely blocks the surface. The linkup process is shown schematically in Figure 10. This theory has not been developed, but the effect is noted here because of its importance in initiation on surfaces having various initiation site densities.

#### Measurement of LSD-Wave Initiation Times on Metals

As noted in the previous sections, the time of LSD initiation is an important measure which is useful in understanding the process of LSD-wave initiation. In the second year of the contract, techniques developed for study of initiation on aluminum were applied to the study of LSD initiation

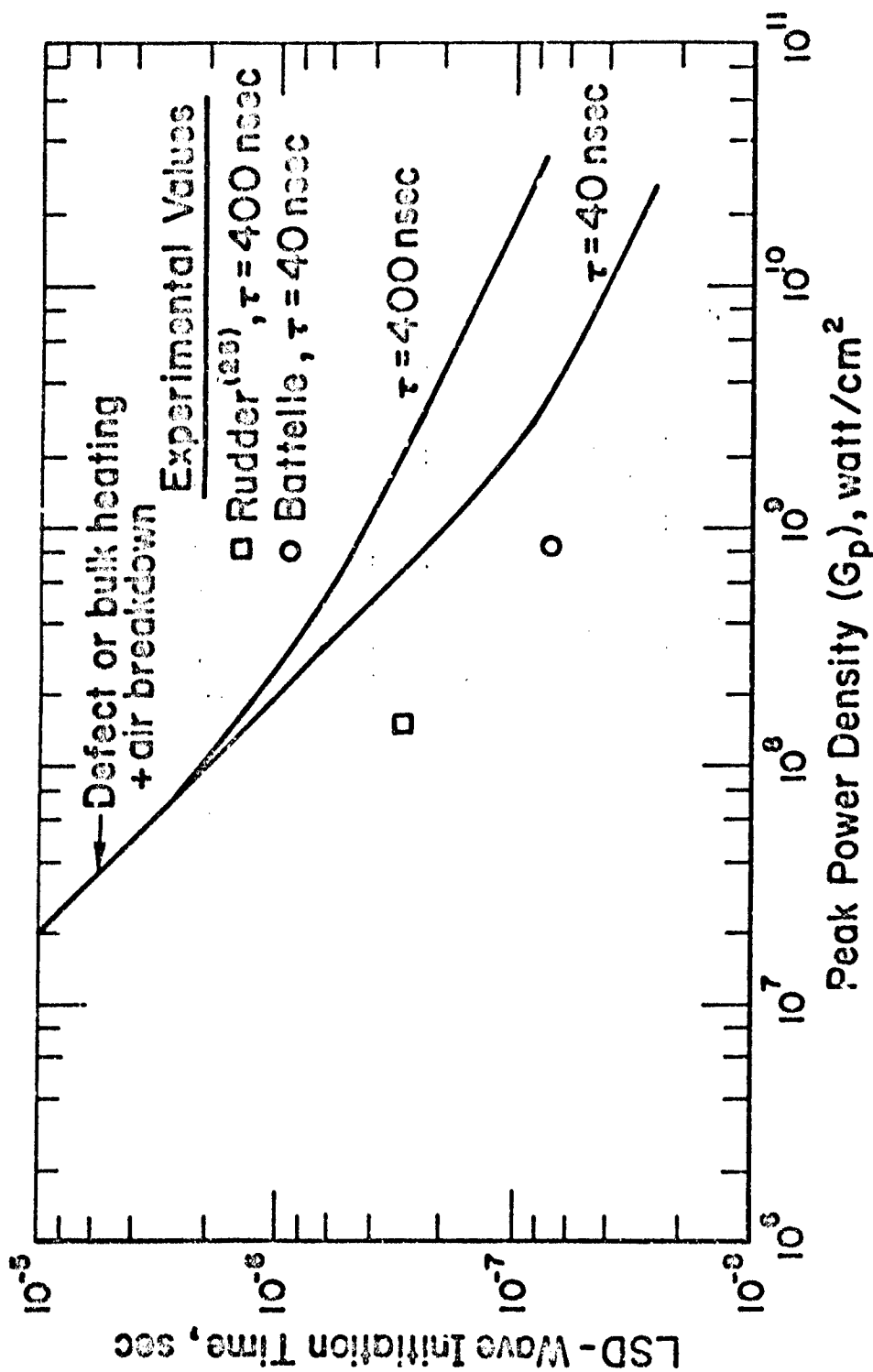


FIGURE 9. INITIATION TIMES FOR ALUMINUM IN  
NORMAL DENSITY AIR AT  $1.06 \mu$

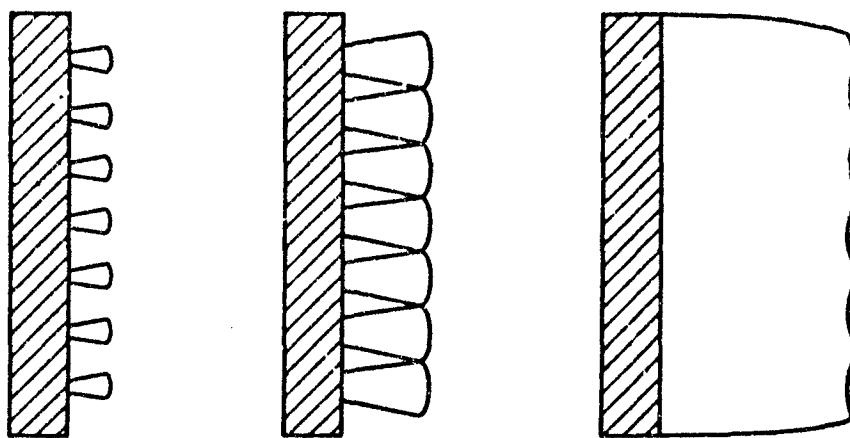


FIGURE 10. SCHEMATIC REPRESENTATION OF THE LINKUP PROCESS

on metallic surfaces in general. These techniques include observation of changes in the target electron emission signal and electrostatic probe detection of the u.v. radiation associated with initiation. These techniques are discussed in detail in Reference (3). Irradiations of several metals in the as-received and cleaned condition were conducted with the 10.6- $\mu$  TEA laser pulse focused to provide peak power densities in the range of  $5 \times 10^7$  to  $5 \times 10^8$  watt/cm<sup>2</sup> in normal density air. Metals studied included aluminum 2024, tungsten, lead, copper, and zinc. Target electron emission and electrostatic probe records were obtained in separate experiments.

Measured LSD-wave initiation times for these experiments are presented in Figure 11 (curves drawn in the figure are for reference only). As in previous work, good agreement was achieved for measurements made by the two techniques. Most of the metals had LSD initiation characteristics similar to those observed previously for aluminum, with the exception of tungsten. A significant delay in initiation on tungsten relative to initiation on other metals was observed. Using the property data of Table 1 and the bulk heating model discussed in the previous sections, it was found that the time to reach melt on a tungsten surface was much greater than the measured initiation time as was the case for aluminum. Again, it is believed that defects on the tungsten surface served as LSD-wave initiation sites. The only other significant deviation from the aluminum data was the observation of very fast initiation on lead surfaces in the lower intensity regime. Rapid heating on lead surfaces results from the low melting temperature and the low volumetric heat capacity (see Table 1). The bulk heating model predicts surface melt for lead at 24 nsec for  $7 \times 10^7$  watt/cm<sup>2</sup> peak power density and 7.4 nsec for  $4 \times 10^8$  watt/cm<sup>2</sup> peak power density. In each case, the vaporization temperature is reached within a few nanoseconds of melting. It is believed to be significant that LSD-wave initiation does not occur on lead earlier than about 27 nsec in the higher intensity regime. If the initiation were occurring in the lead vapor, it would likely occur within 5 nsec of vaporization at  $4 \times 10^8$  watt/cm<sup>2</sup> peak power density. The fact that the initiation time for lead does not decrease significantly with increasing peak power density may be a result of some

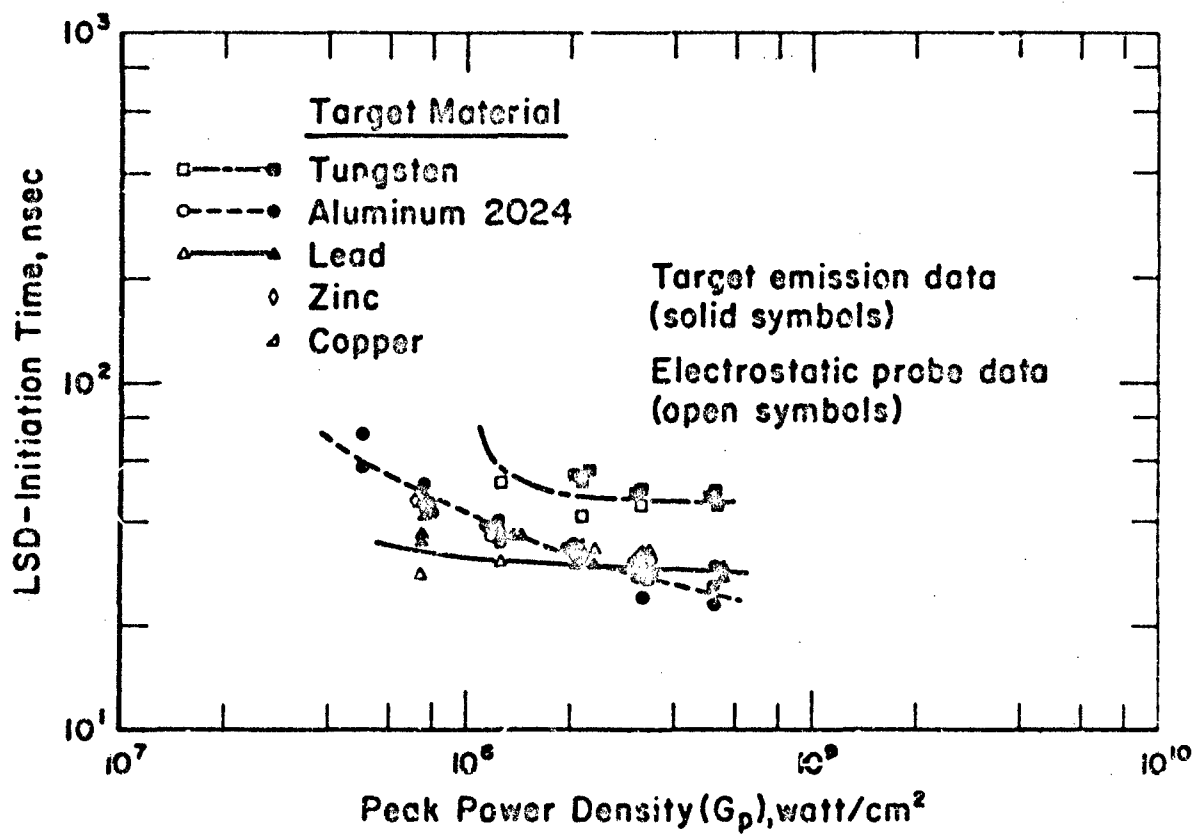


FIGURE 11. LSD-WAVE INITIATION TIMES MEASURED FOR VARIOUS METALS IN NORMAL DENSITY AIR

TABLE 1. HANDBOOK METAL PROPERTY DATA

Metal	Work Function, $\phi$ (eV)	Melting Temperature, $T_m$ (C)	Vaporization Temperature, $T_v$ (C)	First Ionization Potential, $I$ (eV)	Absorbance at $10 \mu$ $\alpha_0$	Density, $\rho$ (gm/cm <sup>3</sup> )	Specific Heat, $C_p$ (J/gm C)	Thermal Conductivity $k$ (watt/cmC)
Al	3.7-4.36	660	2520	5.99	0.029	2.7	0.90	1.6*
Cu	4.4-4.6	1083	2566	7.73	0.012	8.9	0.39	3.9
Mg	3.66	650	1090	7.65	0.07	1.74	1.04	1.6
Tl	4.0-4.45	1670	3289	6.82	0.096	4.5	0.53	0.21
W	4.3	3380	5555	7.98	0.052	19.3	0.13	1.7
Zn	4.2	420	911	9.39	--	7.0	0.38	1.1
Pb	3.49-3.83	327	1750	7.42	0.045	11.3	0.13	0.35

\*Measured for Al 2024.

inhibition of electron emission caused by the fast vaporization or by the presence of vapor. The prediction that bulk vaporization does occur for lead is confirmed by SEM examination of samples.<sup>(3)</sup> Of the metals studied, bulk vaporization was observed only for lead targets. As will be noted in a subsequent section, no ionized lead species were observed at atmospheric pressure.

For all metals studied, significant emission of electrons was observed prior to initiation of the LSD wave. All surfaces were covered with natural defects as in the case of aluminum and the initiation time data are consistent with local initiation at these defect sites, except in the case of lead at the higher values of peak power density.

#### Spectroscopic Studies of LSD-Wave Initiation on Metallic Surfaces

Both time-integrated and time-resolved spectral measurements were performed for targets irradiated at different gas pressures using several different intensity levels from the 10.6- $\mu$  (0.118-eV) CO<sub>2</sub> TEA laser. One of the primary objectives of the spectroscopy effort was to look for evidence of aluminum line emission adjacent to the target surface during the early time regime which could be used to discriminate between the vapor breakdown and thermionic emission initiation mechanisms for LSD waves. The time-resolved measurements dealt only with aluminum targets in nitrogen and helium, while the time-integrated studies also included aluminum targets in dry air along with copper, zinc, tungsten, and lead targets which were irradiated in nitrogen. The pressure covered ranged from below  $1 \times 10^{-5}$  to 1 atm.

Earlier spectroscopic studies are presented in the previous reports<sup>(1,2,3)</sup> on this program. In the earlier work, time-integrated spectra were obtained for irradiations of type 2024 aluminum alloy, fused silica, cellulose acetate, acrylic plastic, zinc, tungsten, lead, copper, titanium, graphite, and type 304 stainless steel targets in air at various pressures between one atmosphere and vacuum. In general, the time-integrated spectra at atmospheric pressure were characterized by spectra associated with oxygen



and nitrogen from the air and some vaporized target materials. At pressures below about 10 torr, the spectra were characterized by emissions from target materials. These observations also hold true for the work reported here.

In the case of the earlier time-resolved measurements with aluminum-alloy targets, the bremsstrahlung radiation typically appeared first at the target surface about 40 nsec after the arrival of the laser pulse. Atomic and ionic radiation was observed at the target surface about 170 nsec after the bremsstrahlung appeared. Neutral aluminum radiation appeared about 700 nsec after the bremsstrahlung. This late appearance of aluminum vapor may result from material boiled off, blown off, or sputtered by the hot air left by the LSD wave. These facts appear to be consistent with the initiation mechanism based on emission of electrons from the target which then couple to the laser field and increase in energy through inverse bremsstrahlung processes. Ion pairs are then created through electron-impact collision with the neutral gas molecules generating additional electrons, which in turn are pumped by the laser beam as discussed previously. Many of the excited atomic and molecular species produced require excitation energies in excess of 20 eV. Additional spectroscopic experiments were conducted to confirm this mechanism and investigate its general applicability to other metals.

#### Time-Integrated Measurements

Spectra were obtained with type 2024 aluminum alloy targets in dry air, nitrogen, and helium, and with copper, zinc, tungsten and lead targets in nitrogen over the spectral ranges from 2450 to 3350 Å and 3450 to 4350 Å. Representative spectra are presented in Appendix A in Figures A1 through A14. The spectrometer slit was oriented perpendicular to the target surface with the viewing direction transverse to the beam axis. For these laser irradiations, the targets were tilted with respect to the line of sight viewed by the spectrometer so as to ensure sampling of the emission at the surface. The lower portion of the spectra shown in Figures A1 through A14 corresponds to the target surface region. The spectra were calibrated using lines from a small mercury lamp.

Prominent lines noted on the spectra are listed in Tables 2 and 3. At 1 atmosphere pressure, the spectra are dominated by bremsstrahlung and a few lines from gas species. In the case of all targets, excited target species were observed at 1 atmosphere, and in most cases the first negative bands of  $N_2^+$  at 3914.4 Å and the second positive bands of  $N_2$  at 3371.3 Å were also present. Typically, the spectra for pressures of 100 torr and 10 torr were dominated by gas species while at 2 torr and  $<1 \times 10^5$  torr, i.e., below the pressure threshold for LSD waves, only lines associated with target materials were identified. The CI carbon line at 2478 Å was observed with all gases and target materials indicating carbon contamination, possibly from the vacuum system. Evidence of carbon contamination was also apparent with copper, zinc, and tungsten which showed strong CN bands at 3883.4, 3871.4, 3861.9, 3854.7, and 3851 Å at atmospheric pressure. All target materials also showed evidence of atomic copper emissions. This would be expected with the type 2024 aluminum alloy which contains copper (4.5% Cu, 1.5% Mg, 0.6% Mn, 0.5% Si, 0.5% Fe, 0.1% Cr, and 0.25% Zn); however, the other targets such as tungsten would not be expected to contain copper. The source of the copper is not known, but may have been the target holder or hold down screws which consisted of brass. Sputtering of copper by the blast wave might be directly responsible for the radiation or deposited copper from a previous blast wave might be excited by the laser beam.

In general, spectral lines from target atoms involved excitation energies less than 10 eV while the lines from the nitrogen and helium atoms were associated with excitation energies well above 10 eV. Except in the case of tungsten, as the laser beam intensity was increased to the emission threshold at a given pressure, the first spectral lines to appear in the wavelength regions recorded were three lines at 2803.3, 2802.5, and 2796.1 Å. With increasing laser intensity two other lines also appeared near 2800 Å. These five lines were observed with all the target materials: Al, Cu, Zn, W, and Pb. In the case of tungsten, however, W lines were the first to appear near threshold. The wavelengths and tentative identifications for these lines are given in Table 4. A strong candidate to associate

TABLE 2. PROMINENT EMISSION LINES OBSERVED IN  
TIME-INTEGRATED SPECTRA NEAR 3000 Å

<u>Wavelength, Å</u>	<u>Emitter</u>	<u>Energy of Lower Level, eV</u>	<u>Energy of Upper Level, eV</u>
3331.310	N II <sup>(a)</sup>	20.64	24.38
3330.314	N II	20.61	24.38
3329.705	N II	17.88	21.60
3328.730	N II	20.56	24.38
3006.830	N II	20.41	24.53
2885.273	N II	23.14	27.44
2709.837	N II	21.60	26.17
2522.227	N II	21.16	26.07
2520.791	N II	21.15	26.06
2520.222	N II	21.15	26.06
3187.745	He I	19.82	28.71
3203.104	He II <sup>(b)</sup>	48.37	52.24
2733.32	He II	48.37	52.40
2478.556	C I	2.68	7.68
3092.8386	Al I	0.01	4.02
3092.7099	Al I	0.01	4.02
3082.1529	Al I	0.00	4.02
2852.127	Mg I	0.00	4.35
3273.957	Cu I	0.00	3.79
3247.540	Cu I	0.00	3.82
2882.934	Cu I	1.39	5.69
3282.33	Zn I	4.01	7.78
3302.59	Zn I	4.03	7.78
3302.94	Zn I	4.03	7.78
3345.02	Zn I	4.08	7.78
3345.57	Zn I	4.08	7.78
3345.93	Zn I	4.08	7.78
2770.88	W I	0.37	4.84
2573.53	W I	1.65	6.46
2613.65	Pb I	0.97	5.71
2614.18	Pb I	0.97	5.71
2663.17	Pb I	1.32	5.97
2801.99	Pb I	1.32	5.74
2823.19	Pb I	1.32	5.71
2833.07	Pb I	0	4.37
2873.32	Pb I	1.32	5.63

(a) The ionization energy of N I is 14.548 eV.

(b) The ionization energy of He I is 24.586 eV.

TABLE 3. PROMINENT EMISSION LINES OBSERVED IN  
TIME-INTEGRATED SPECTRA NEAR 4000 Å

<u>Wavelength, Å</u>	<u>Emitter</u>	<u>Energy of Lower Level, eV</u>	<u>Energy of Upper Level, eV</u>
4224.74	N I	10.33	13.26
4223.04	N I	10.34	13.27
4241.784	N II <sup>(a)</sup>	23.24	26.17
4237.05	N II	23.24	26.17
4236.91	N II	23.24	26.17
3994.998	N II	18.50	21.60
3437.147	N II	18.50	22.10
4026.1912	He I	20.96	24.04
3888.648	He I	19.82	23.01
3961.5200	Al I	0.01	3.14
3944.0058	Al I	0.00	3.14
3964.16	Cu I	5.69	8.81
3933.027	Cu I	5.78	8.93
4095.70	W I	2.11	5.13
4102.70	W I	0.77	3.79
4234.35	W I	2.39	5.31
4241.45	W I	1.92	4.84
3572.73	Pb I	2.66	6.13
3639.58	Pb I	0.97	4.37
3683.48	Pb I	0.97	4.33
3739.95	Pb I	2.66	5.97
4057.82	Pb I	1.32	4.37
4150.138	Al III <sup>(b)</sup>	20.55	23.54
4149.917	Al III	20.55	23.54
4149.897	Al III	20.55	23.54

(a) The ionization energy of N I is 14.548 eV.

(b) The ionization energies for Al I and Al II are 5.985 and 18.827 eV, respectively.

TABLE 4. INTENSITY THRESHOLD LINES AT 2800 Å

Observed Wavelength, Å	Tentative Identification		Other Possible Identifications		
	Spectral Line	Energy of Lower Level, eV	Energy of Upper Level, eV	Spectral Line	Energy of Lower Level, eV      Energy of Upper Level, eV
2803.3	Cu I 2803.686	5.24	9.67		
2802.5	Cu I 2802.556	5.10	9.52	Mg II <sup>(b)</sup> 2802.69	0.00      4.42
				Mn I 2801.06	0.00      4.42
				Zn I 2800.87	4.08      8.50
2795.4	Cu II <sup>(a)</sup> 2799.536	14.34	18.77	Mg II <sup>(b)</sup> 2799.06	4.43      8.86
				Mn I 2798.27	
2796.0	Cu II <sup>(a)</sup> 2795.31	14.34	18.77	Mg II <sup>(b)</sup> 2795.53	0.00      4.43
				Mn I 2794.82	
2791.4	Cu II <sup>(a)</sup> 2791.748	14.34	18.77	Mg II <sup>(b)</sup> 2790.79	4.42      8.86

(a) The ionization energy of Cu I is 7.726 eV.

(b) The ionization energy of Mg I is 7.646 eV.

these lines is copper. It is difficult, however, to unequivocally identify these as copper lines because they are usually less prominent relative to the strong resonance lines in conventional arc and spark spectra. Similar lines at 2802.7 and 2795.5 Å were observed by Wei and Hall<sup>(26)</sup> for a masking-tape target irradiated with a 10.6-μ CO<sub>2</sub> TEA laser. They identified these lines as Mg II lines. The good wavelength correspondences with copper lines and the presence of the 2803.3-2802.5 Å doublet do tend, however, in the present case, to lend weight to the suspicion of copper. The results may indicate that something common to all sample materials such as the brass target holder may be playing a role in the radiation observed at low intensity. It is certainly interesting to note that spectral lines with lower excitation energies did not appear first.

#### Time-Resolved Measurements

Results of the time-resolved measurements are presented in Figures 12 through 18. The time-integrated measurements involved only aluminum targets with nitrogen and helium. These measurements were performed using the SPEX 3/4-meter Czerny-Turner spectrometer with an EMI Type 6256 photomultiplier as a detector. Output from the detector was displayed using a Tektronix 7704 oscilloscope and recorded photographically. The transient curves in the figures have been corrected for a photomultiplier delay of 55 nsec and a scope trigger delay of ~50 nsec. Specific spectral lines were monitored by setting the grating angle to pass the desired wavelength. The bremsstrahlung in the region of a line was determined by measurements performed on both sides of the line. The bremsstrahlung contribution was then subtracted to give the corrected line radiation which is given in the figures. Targets were used for multiple irradiations and were not replaced for each irradiation as was done in some of the earlier studies.

In general, the initial rise of the atomic nitrogen and helium emissions came after the rise of bremsstrahlung. Both the Al I and Al III showed a delay in their appearance after the rise of the bremsstrahlung. No Al I line radiation was found to precede the bremsstrahlung or to appear within the first microsecond following the arrival of the laser pulse at the

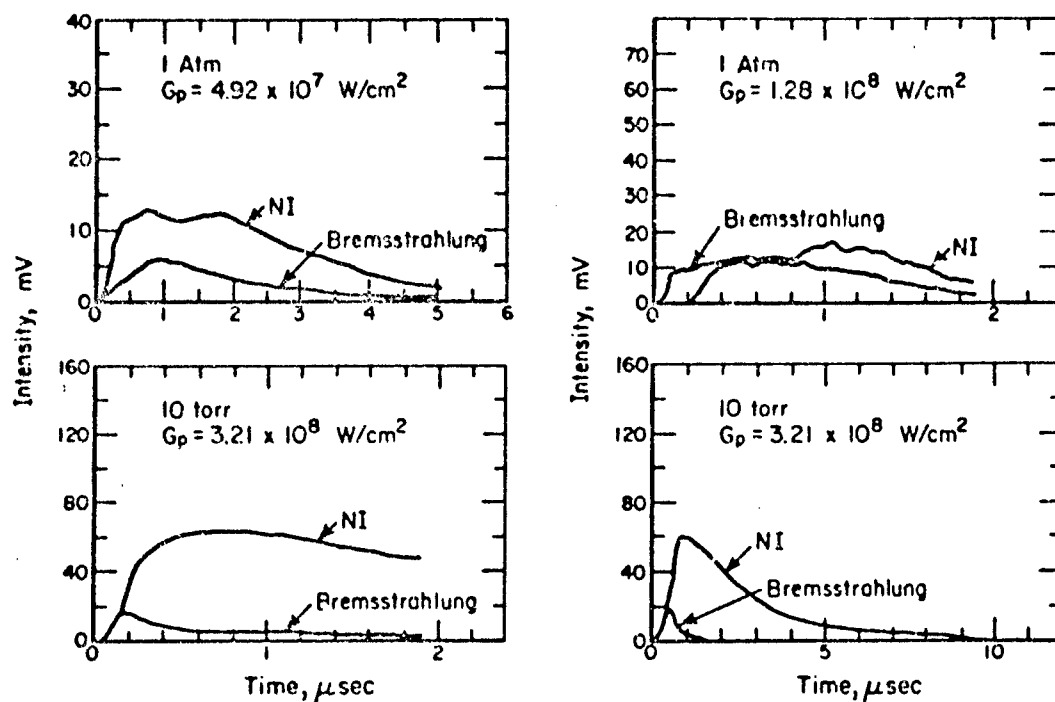


FIGURE 12. RADIATION INTENSITIES FOR BREMSSTRAHLUNG AND N I LINE AT 3994.86 Å AT SURFACE OF ALUMINUM TARGET IN NITROGEN

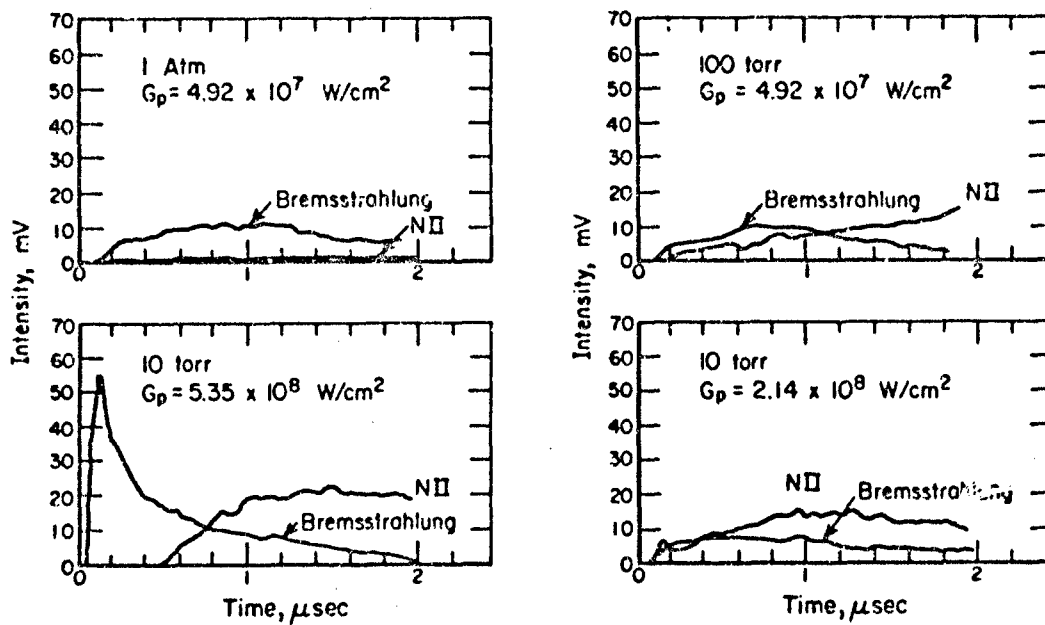


FIGURE 13. RADIATION INTENSITIES FOR BREMMSTRAHLUNG AND N II LINE AT 3006.83 Å AT SURFACE OF ALUMINUM TARGET IN NITROGEN



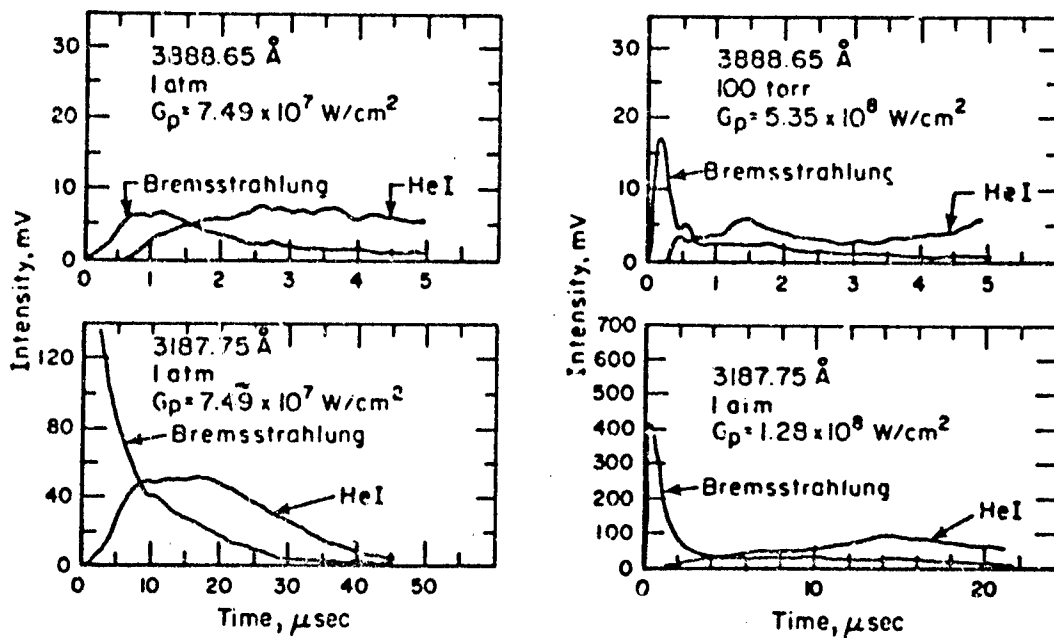


FIGURE 14. RADIATION INTENSITIES FOR BREMSSTRAHLUNG AND He I LINES AT SURFACE OF ALUMINUM TARGET IN HELIUM

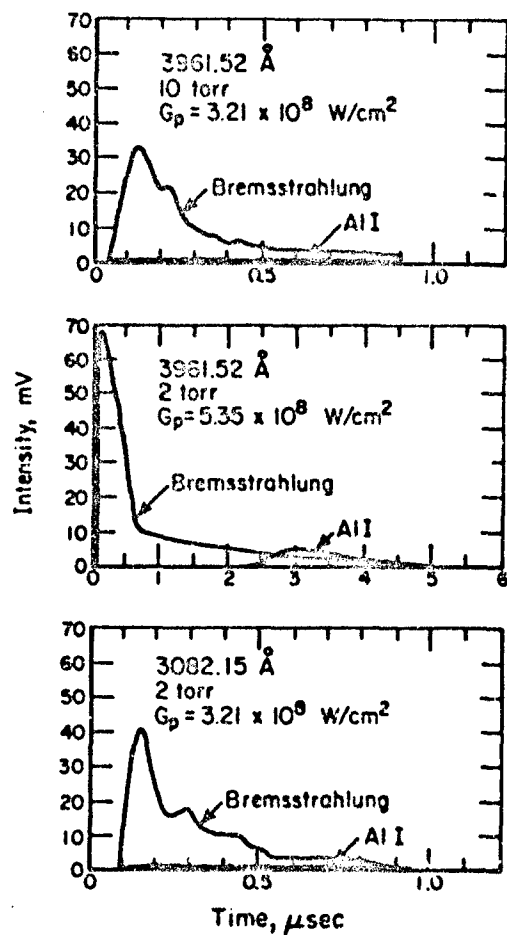


FIGURE 15. RADIATION INTENSITIES FOR BREMSSTRAHLUNG AND Al I LINES AT SURFACE OF ALUMINUM TARGET IN NITROGEN

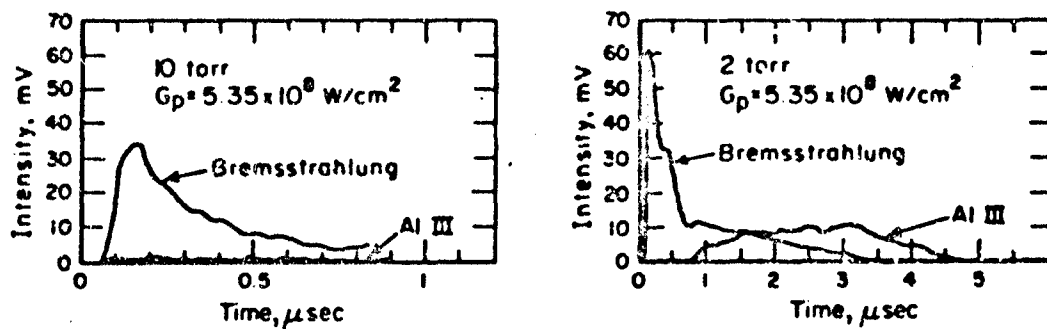


FIGURE 16. RADIATION INTENSITIES FOR BREMSSTRAHLUNG AND Al III LINE AT 4150 Å AT SURFACE OF ALUMINUM TARGET IN NITROGEN

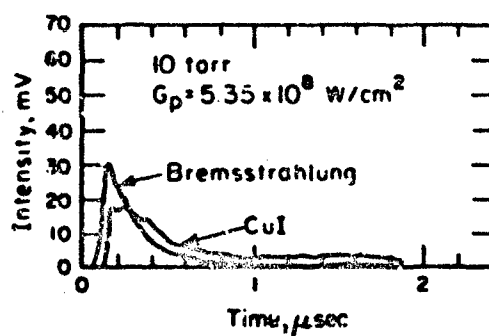
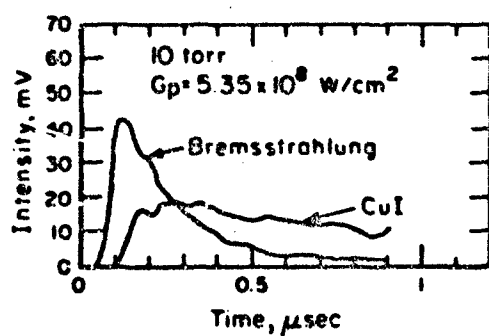


FIGURE 17. RADIATION INTENSITIES FOR BREMSSTRAHLUNG AND  
 Cu I LINE AT 3247.54 Å AT SURFACE OF ALUMINUM  
 TARGET IN NITROGEN

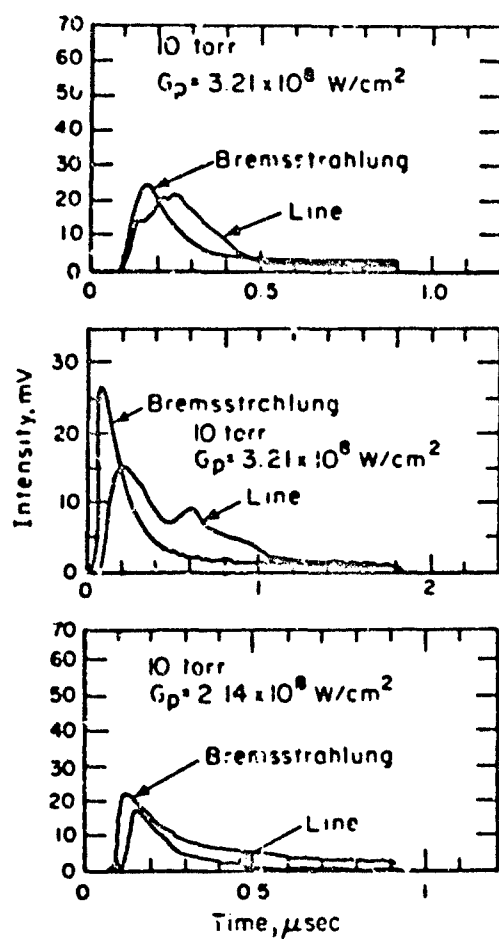


FIGURE 18. RADIATION INTENSITIES FOR BREMSSTRAHLUNG AND SPECTRAL LINE AT 2803 Å AT SURFACE OF ALUMINUM TARGET IN NITROGEN

target surface as shown in Figure 15. The C I radiation and the radiation at 2803 Å, tentatively associated with Cu I emission, did appear less than 100 nsec after the rise of the bremsstrahlung as shown in Figures 17 and 18, although their appearance is still well after plasma initiation.

Al III line radiation at 4150 Å was observed at a pressure of 2 torr. This line emission as shown in Figure 16, followed the appearance of the bremsstrahlung by about 700 nsec as observed earlier for the neutral Al I line emission at the target surface.

#### Conclusions Drawn from the Spectroscopy Experiments

Time-integrated spectra obtained with type 2024 aluminum alloy targets in dry air, nitrogen and helium, and with copper, zinc, tungsten, and lead targets in nitrogen all showed evidence of excited target vapors at both atmospheric and reduced pressures. Spectra involving pressures from 10 torr to one atmosphere were dominated by lines associated with gas species while only target lines were observed at pressures below 10 torr.

Time-resolved spectral measurements with type 2024 aluminum alloy targets in air showed that the bremsstrahlung radiation at the target surface preceded in time radiation from the nitrogen which in turn preceded the radiation from excited aluminum vapor. At pressures near 2 torr, i.e., below the LSD-wave pressure threshold Al III ( $\text{Al}^{++}$ ) radiation was observed which followed the same temporal response as the neutral Al I emission. No aluminum radiation was detected, however, during the early initiation period at times of less than 100 nsec after the arrival of the 10.6- $\mu$  TEA laser pulse at the target. The results indicate that the laser field couples with the free electrons which then excite, dissociate, and ionize the nitrogen species. This is then followed by excitation of the target material. Aluminum could be present in the vapor at early times, but not excited. However, this does not seem likely, as the excited nitrogen species observed require considerably more excitation energy than the aluminum transitions that were observed.

Initiation of LSD Waves on  
Aluminum Alloy at 1.06 Micron

While the major effort under this contract was devoted to the study of LSD wave initiation at the 10.6- $\mu$  wavelength, a series of irradiations were performed at 1.06 $\mu$  to preliminarily assess some of the effects of laser wavelength on the initiation physics. A six-joule, Q-switched, neodymium-glass laser having a 40 nsec pulse width was used for the irradiations. The output pulse history is very similar to that of the TEA-CO<sub>2</sub> laser on the rising portion of the pulse as can be seen in Figure 19. This feature enables convenient comparison of LSD-initiation results for the two lasers, however, the fast fall of the 1.06 $\mu$  laser pulse leads to the disadvantage of limited propagation distance for the LSD wave. The beam was focused with a 100-cm-focal-length lens onto an aluminum alloy (2024) target placed in front of focus in laboratory air and tilted to provide a 20° incidence angle. The target was supported in the target emission sample holder in a geometry identical to that used for target emission measurements at 10.6 $\mu$ .<sup>(3)</sup> The beam profile was approximately gaussian with a 1/e area of 0.18 cm<sup>2</sup>. Intensity was varied by introducing calibrated attenuators and, in some cases, by reducing the spot size. A fast photodiode and calorimeter monitored a reflection from a glass beam splitter placed in the beam. The photodiode was used to trigger the oscilloscope which recorded the target voltage response. The plasma luminosity was recorded by open shutter photography through a broadband green filter (maximum transmission 2.5 percent).

The target emission records for irradiations with peak power densities in the range of  $1-8 \times 10^8$  watt/cm<sup>2</sup> and constant spot size are presented in Figure 20 (laser beam on target at 40 nsec). As can be seen, a positive-going signal is observed indicating electron emission from the target surface. The signal rises much earlier in the pulse than was observed in the 10.6- $\mu$  experiments, which is consistent with the higher absorption at 1.06  $\mu$ . The target voltage levels are considerably lower than those measured at 10.6  $\mu$  on

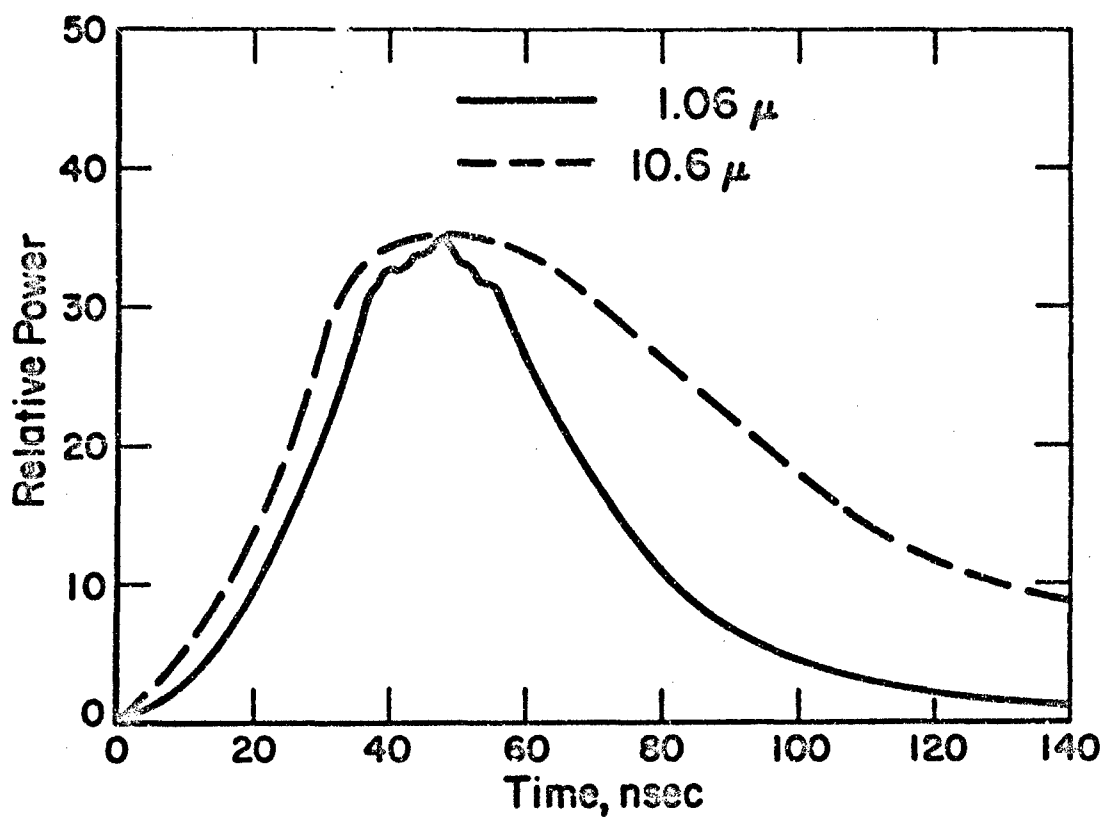


FIGURE 19. LASER PULSE HISTORIES FOR THE  
1.06- $\mu$  AND 10.6- $\mu$  LASERS



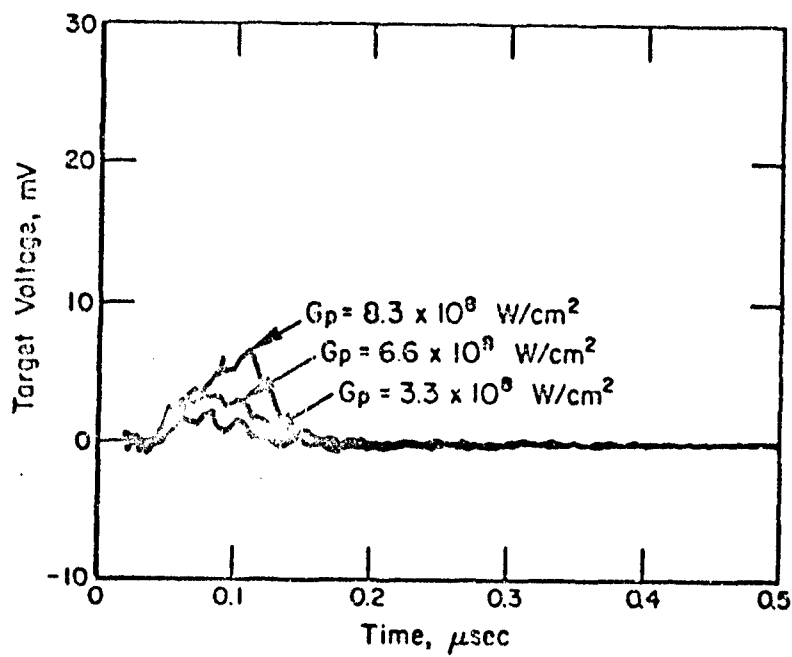


FIGURE 20. TARGET ELECTRON EMISSION RECORDS  
FOR ALUMINUM 2024 at  $1.06 \mu$

aluminum 2024. This may result, in part, from fewer emitting sites being active with the smaller spot size of the 1.06- $\mu$  experiment. No "break" in the target emission signal was observed in the lower intensity irradiations, however, at  $8.3 \times 10^8$  watts/cm<sup>2</sup> peak power density, a well-defined drop in the signal was observed 78 nsec after laser pulse arrival. In the 10.6- $\mu$  experiments, this characteristic "break" in the target emission signal has been correlated with the plasma initiation time or breakdown time determined by other means. (3) In all cases, plasma luminosity was observed photographically; however, the short LSD-wave trajectory, if present, was indistinguishable from the aluminum vapor cloud which was oriented normal to the target surface. Sample examination revealed that the threshold for bulk vaporization occurred at  $10^8$  watts/cm<sup>2</sup> and damage got progressively worse with increasing intensity until peak power densities on the order of  $1.5 \times 10^{10}$  watts/cm<sup>2</sup> were attained. At this level presumably the initiation occurs sufficiently early to provide some radiation blockage and reduction in damage.

While additional experimental work is needed to confirm the breakdown timing measurement, the present data appear to fit into a consistent picture of LSD-wave initiation as discussed in a previous section. For the pulse rise time and peak power density regime investigated, the breakdown is expected to occur in the metal vapor. From Figure 4, it is noted that both defect and bulk metal vaporization are predicted to occur prior to the pulse maximum at  $10^8$  watts/cm<sup>2</sup> which is consistent with the experimental observation of bulk vaporization at this level. For a peak power density of  $8.3 \times 10^8$  watts/cm<sup>2</sup>, the predicted times for a model defect vaporization and bulk vaporization are 8 and 9 nsec, respectively. If the plasma breakdown time is 78 nsec as inferred from the target emission probe, then the metal vapor heating time is of order 70 nsec under these conditions. According to the LASNEX calculation for the TEA laser pulse<sup>(17)</sup>, the time to heat the metal vapor from the vaporization temperature to 1.0 eV at 10.6  $\mu$  and  $7 \times 10^7$  watts/cm<sup>2</sup> peak power density is approximately 2 nsec for a

high-density Mott transition ( $\rho = 1.0 \text{ gm/cm}^3$ ) and 7 nsec for a low-density Mott transition ( $\rho = 0.1 \text{ gm/cm}^3$ ). Corrected for wavelength scaling and intensity, these times are 34 and 118 nsec, respectively, at  $1.06\mu$  and  $8.3 \times 10^8 \text{ watts/cm}^2$ . These values bracket the heating time of 70 nsec inferred from the experiments. It is important to note that electron emission did occur in the experiments and, according to the model discussed in Reference (1), it is reasonable to assume that primary electron densities on the order of  $10^{14} \text{ cm}^{-3}$  were produced in the air in front of the target. However, according to the air cascade heating results presented in Figure 7 (scaled appropriately to the present case), the time to achieve  $10^{18} \text{ cm}^{-3}$  electron density in air with a priming density of  $10^{14} \text{ cm}^{-3}$  would be 230 nsec. Since this time is much longer than the pulse length, it is reasonable to conclude that the initiation process in the regime studied at  $1.06\mu$  is dominated by breakdown in the vapor. Furthermore, the short times for both defect and bulk metal vaporization infer that initiation is not particularly defect oriented.

### III - LSD-WAVE INITIATION ON NONMETALLICS

A limited number of experiments were conducted in the program to assess mechanisms which might be operative in the initiation of LSD waves on nonmetallic materials at  $10.6\ \mu$ . In early work,<sup>(2,27)</sup> fused silica and acrylic plastic were found to initiate LSD waves in a similar way. Initiation was found to be local as in the case of practical aluminum surfaces; however, the initiation site density was two orders of magnitude lower. The sites of initiation were easily identified by small protected areas on the surface where the "miniature" LSD waves blocked the laser radiation and prevented vaporization. Associated with the sites were characteristic interference-fringe damage patterns indicating the existence of an embedded debris particle acting as a scattering center. If the embedded particles are metallic in nature, then the metallic initiation mechanism might apply in this case. Irradiations of cellulose acetate revealed much more uniform damage patterns with no evidence of protected regions.

Several additional nonmetallic materials were irradiated in atmospheric pressure air at  $10.6\ \mu$  to survey the extent to which local initiation occurs in other nonmetallic materials. Sample materials irradiated included phenolic resin, polyimide, high-density alumina, and silicon. Time-integrated photography and post irradiation sample examination were utilized to assess LSD-wave initiation behavior. The approximate thresholds for LSD-wave initiation (as determined by photography) and the damage characteristics are presented in Table 5 along with data obtained previously for other nonmetallics. Only the polyimide samples exhibited isolated protected areas similar to the initiation sites observed for fused silica and acrylic plastic. It should be noted, however, that all of the luminosity records revealed a considerably more coarse structure (miniature LSD-wave trajectories) than occurs for metallic irradiations. This is consistent with the low initiation site density observed for fused silica, acrylic plastic, and polyimide, but may also infer a localized breakdown occurring in the vapor or on unvaporized ejected constituents. The silicon samples exhibited quite different damage characteristics as shown in the Nemarski photomicrograph of Figure 21. The

TABLE 5. APPROXIMATE LSD-WAVE THRESHOLDS  
FOR NONMETALLIC MATERIALS

Material	LSD-Wave Threshold Peak Power Density ( $10^8$ watt/cm <sup>2</sup> )	Damage Characteristic
Acrylic Plastic	0.8	Protected areas
Fused Silica	1.5	Protected areas
Phenolic Resin	1.5	Extensive uniform vaporization
Polyimide	0.6	Protected areas
Alumina	<1	Uniform vaporization
Cellulose Acetate	1.5	Uniform vaporization
Silicon (polished)	0.6	Local spots

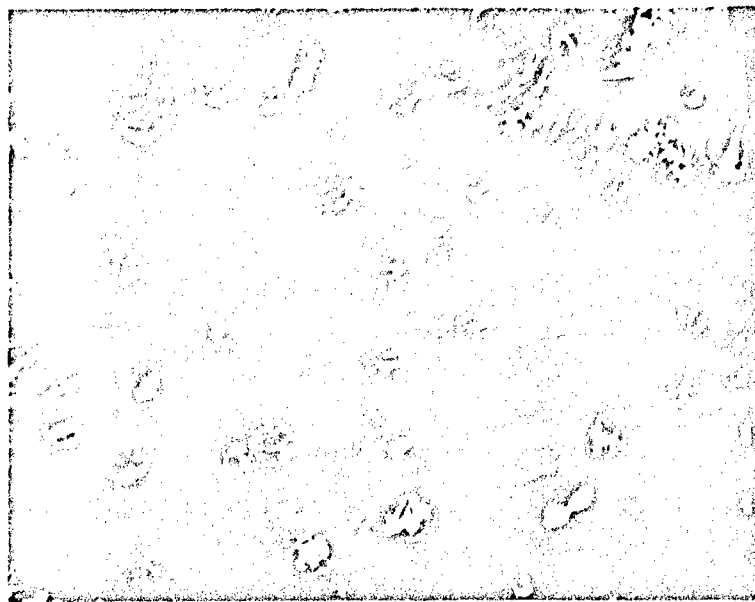


FIGURE 21. NOMARSKI MICROGRAPH OF DAMAGE SITES ON  
POLISHED N-TYPE SILICON (1.3 ohm-cm)  
IRRADIATED AT  $3.2 \times 10^8$  watt/cm<sup>2</sup>

damage shown is for a peak power density well above threshold ( $3.2 \times 10^8$  watt/cm<sup>2</sup>) and consists of isolated areas approximately 20  $\mu$  in diameter which have melted or vaporized. As can be seen, the regions between the damage sites are very smooth, but do have submicron-sized surface features. Heating may initiate at these defects and lead to the observed damage in a manner similar to that occurring in metals. This may be contrasted to the plastic materials which heat more uniformly and are protected locally by debris-initiated LSD waves in some cases. Because of the high electrical and thermal conductivity relative to the plastics and the observed damage characteristics, silicon is believed to initiate LSD waves in a manner similar to that occurring on a metal only with a lower initiation site density. The initial stages of defect heating are quite different, however, because the silicon is fairly transparent to 10.6- $\mu$  radiation at room temperature. Near 500 C, the absorption rises and thermal runaway followed by "metalization" occurs. The two basic types of initiation process observed on the plastic materials were investigated further as discussed below.

#### LSD-Wave Initiation Time for Cellulose Acetate

It is somewhat surprising that the LSD-initiation threshold for cellulose acetate is  $1.5 \times 10^8$  watt/cm<sup>2</sup>, while the threshold for damage is of order  $7 \times 10^6$  watt/cm<sup>2</sup>. It is widely believed that breakdown in organic vapors is relatively rapid because of low ionization potentials. All of the experimental evidence for cellulose acetate indicates vapor heating and subsequent breakdown of the vapor; however, the threshold intensity is high and the initiation time is much longer than observed for metallic and debris initiated LSD waves. The initiation time was measured using the electrostatic probe technique,<sup>(3)</sup> which records the time of first appearance of strong bremsstrahlung radiation, i.e., the u.v. precursor photoionization of air around the probe. The initiation times recorded for cellulose acetate at 2.1 and  $3.2 \times 10^8$  watt/cm<sup>2</sup> were 55 and 53 nsec, respectively, which were the longest initiation times ever measured by this technique at these intensities. Below  $2.2 \times 10^8$  watt/cm<sup>2</sup> some precursor signal was recorded but it was uncharacteristic of full initiation. The peak of the precursor signal occurs about 70 nsec

after laser pulse arrival. Its magnitude is related to the intensity of the u.v. radiation produced. For LSD waves which initiate early, there is time for the miniature LSD waves to grow significantly and provide more u.v. emitting area than in the case of late initiation. This effect is shown in Figure 22 which presents peak precursor signals observed under the same conditions for several metals and cellulose acetate. The differences in the metallic behavior appear to be completely consistent with observed differences in initiation times. The low signal for cellulose acetate confirms the weak development of LSD waves in the vapor. These data also tend to confirm the importance of surface-emitted electrons in prompt initiation on metal surfaces.

#### Debris Initiation on Nonmetallics

In the previous studies of LSD-wave initiation on fused silica and acrylic plastic,<sup>(2,27)</sup> it was conjectured that embedded metallic debris might be the source of the scattered-wave interference-fringe damage pattern associated with the local LSD-wave initiation sites. Further, it was suggested that the prompt initiation mechanisms might result from thermionic emission from these particles. To assess whether metallic debris particles could cause the observed effect, acrylic samples were prepared with purposely-embedded aluminum particles. Particle size distributions were not measured, but average diameters were estimated to be of order  $1\ \mu$  and  $20\ \mu$  for the two conditions studied. The particles were mechanically embedded and the non-adhering particles were removed with a gas jet. The specially prepared surfaces and normal acrylic surfaces were irradiated with the  $10.6\text{-}\mu$  laser pulse in air under identical conditions at  $2.1 \times 10^8$  watt/cm<sup>2</sup>. Post-irradiation Nomarski micrographs taken near the center of the irradiance areas of these samples are presented in Figure 23. The untreated acrylic surface exhibited several isolated protected areas as observed previously. A typical protected area is shown in Figure 23(a). For the case of normal incidence in these experiments, circular incipient damage fringes would be expected rather than elliptical fringes observed earlier on acrylic. At the particular site shown, there appear to be several debris particles on the surface which may have destroyed the coherent pattern. Figures 23(b)



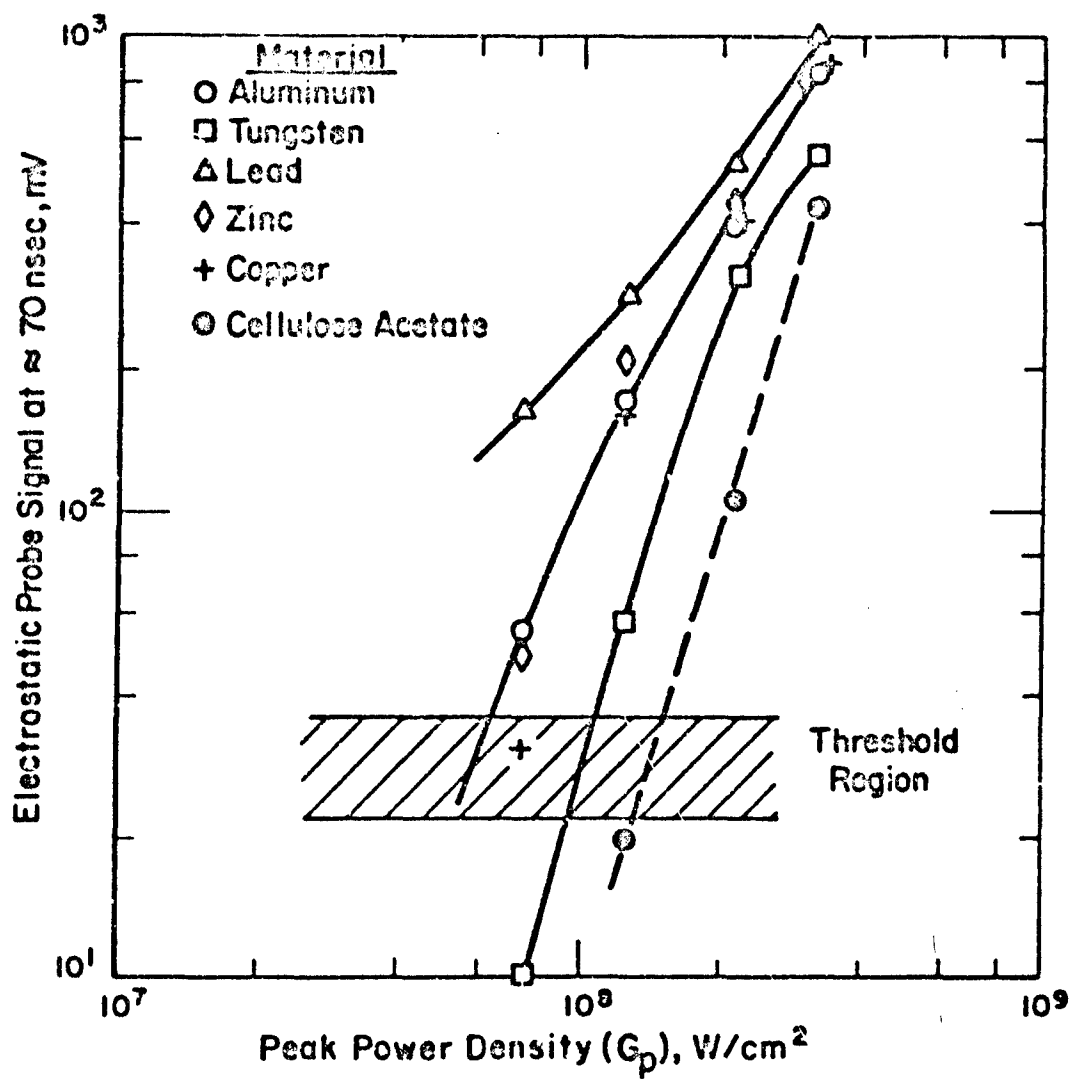
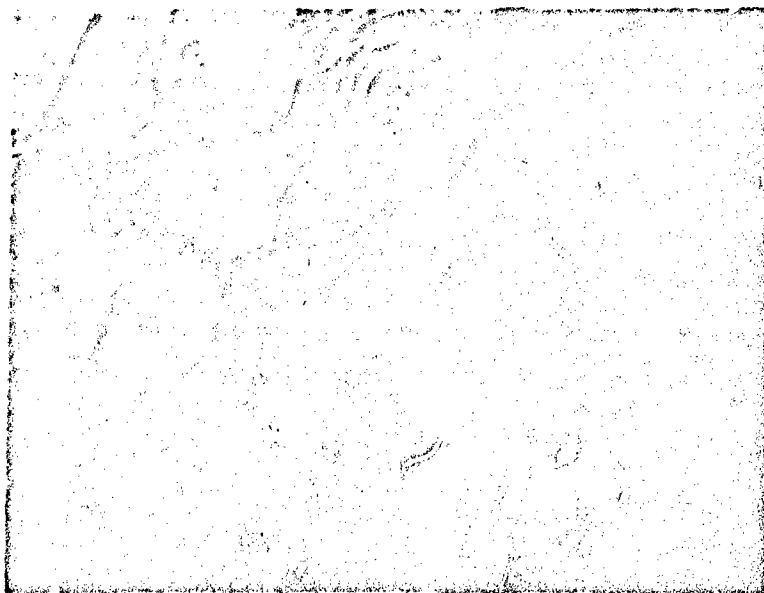


FIGURE 22. PEAK PRECURSOR SIGNAL ON ELECTROSTATIC PROBE

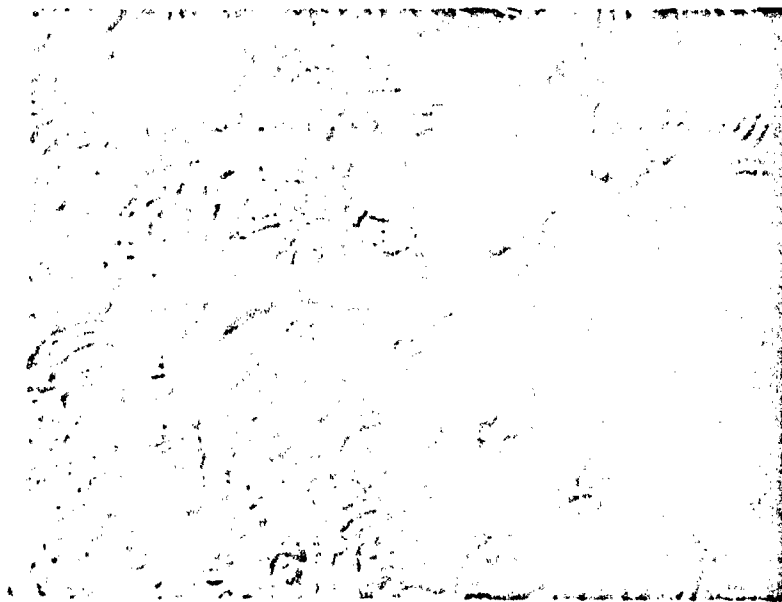


(a) Untreated Surface



(b)  $2.2\text{-}\mu$  Aluminum Particles Embedded in Surface

FIGURE 23. NOMARSKI MICROGRAPHS OF LSD-WAVE INITIATION  
SITES ON ACRYLIC SURFACES IRRADIATED AT  
 $2.1 \times 10^8$  watt/cm<sup>2</sup>



(c) 1- $\mu$  Aluminum Particles Embedded in Surface

FIGURE 23. (Continued)

and (c) present corresponding Nomarski micrographs for surfaces with embedded aluminum particles having 1 and 20- $\mu$  diameters, respectively. The dark areas are the heavily vaporized regions and the light rippled areas are protected regions. The Nomarski technique enhances the surface topography and enables identification of the incipient damage fringe patterns. These fringes do occur and are observed to be circular and apparently centered on aluminum debris remnants. The effect of the debris-initiated LSD waves is dramatic, with very little damage visible to the unaided eye. It is concluded that embedded metallic debris particles are likely responsible for one observed type of nonmetallic LSD-wave initiation.

#### IV - PRESSURE RESPONSE MEASUREMENTS

The prediction and measurement of momentum transfer and shock pressure associated with laser irradiation of solid surfaces has received much attention in recent years. Experiments have been performed with a variety of target materials under ambient pressure conditions ranging from hard vacuum to atmospheric pressure and with various laser systems and wavelengths. The earliest experiments utilized either ruby<sup>(28-30)</sup> or neodymium<sup>(31-38)</sup> lasers, although interest in CO<sub>2</sub>-laser experiments<sup>(39-47)</sup> has increased dramatically with the development of large electron-beam and TEA-type devices. One recent paper<sup>(48)</sup> describes the impulsive loading on aluminum targets when irradiated by an electron-beam-initiated HF laser. A critical issue not addressed in the previous studies is the direct effect of LSD-wave initiation on pressure response as assessed by varying ambient pressure and peak power density through the threshold levels for LSD initiation.

This section describes the first measurements of pressure profiles induced by a TEA CO<sub>2</sub> laser. The experiments employed both metallic and non-metallic targets, and the irradiations were conducted both above and below the thresholds for initiation of laser-supported detonation (LSD) waves. Aluminum alloy (3003) and two plastics were irradiated with TEA laser pulses having a peak power density of  $3.2 \times 10^7$  -  $5.8 \times 10^8$  watt/cm<sup>2</sup> with ambient pressures ranging from hard vacuum to 760 torr dry air. Both back-surface and in-material pressure measurements were performed for each set of data. We note that of all the CO<sub>2</sub>-laser experiments referenced above, only Ready<sup>(40)</sup> employed a TEA-type laser having a submicrosecond pulse duration. In most of his experiments, no nitrogen was used in the laser gas mixture, resulting in pulse lengths of order 100 nsec and hence, short-lived LSD waves. The experiments were restricted to impulse measurements which were found to differ considerably from results obtained using long-pulse CO<sub>2</sub> lasers. In the present experiments, long-lived LSD waves were observed, often with the cylindrical plasma column exceeding 5 cm in length. Ample laser energy and peak power were available for the initiation and propagation of LSD waves from both metallic and nonmetallic surfaces for a relatively large spot area ( $\approx 0.3$  cm<sup>2</sup> for an effective spot diameter  $D_s \approx 0.61$  cm).

The shock pressure and resultant impulse imparted to a solid surface which initiates an LSD wave have been successfully predicted by cylindrical blast wave theory,<sup>(49-51)</sup> and numerous computer simulations<sup>(52-57)</sup> have been based on this approach. Ready<sup>(40)</sup> modeled his experimental TEA-laser results with a spherical blast wave originating a few millimeters above the target surface. Because of the short duration of the LSD wave in his experiments, this approach is justifiable and reasonably accurate. Ready<sup>(40)</sup> could not, however, obtain agreement with the experimental results using the cylindrical blast wave theory of Pirri.<sup>(49)</sup> We have compared our results with the theory of Pirri,<sup>(49)</sup> and believe that the adjustments required by the spherical blast wave theory are artificial and not descriptive of the physical processes dominant in our experiments. The need for explicit treatment of the temporal and spatial characteristics of the laser beam in any analytical theory of short-pulse CO<sub>2</sub>-laser interactions is confirmed by our experiments.

#### Description of the Experimental Configuration

The general arrangement of beam optics, target, and diagnostics is shown schematically in Figure 24. The laser beam is focused by mirrors M<sub>1</sub> and M<sub>2</sub> and transported into the target chamber through a KCl flat whose surface normal is tilted with respect to the beam axis. The two reflections from the KCl flat are incident on a photon drag detector (Rofin model 7411) for triggering the oscilloscope used in the pressure measurements. A cone calorimeter may be substituted at either the photon drag or target location for energy measurement. The target chamber is of stainless steel construction and can be evacuated to 10<sup>-7</sup> torr by a standard mechanical pump/diffusion pump arrangement. The target and pressure gauge assemblies were placed near the center of the chamber and were attached to a translatable holder which is externally controllable. Open-shutter photographic diagnostics were set up at the indicated port. Additional ports (not shown) were used for electrical feedthroughs, ambient pressure gauges, and visual observation.

Both quartz piezoelectric and carbon piezoresistive gauges were employed in the experiments, and since precise timing relationships are required, considerable care was exercised in the electronic triggering

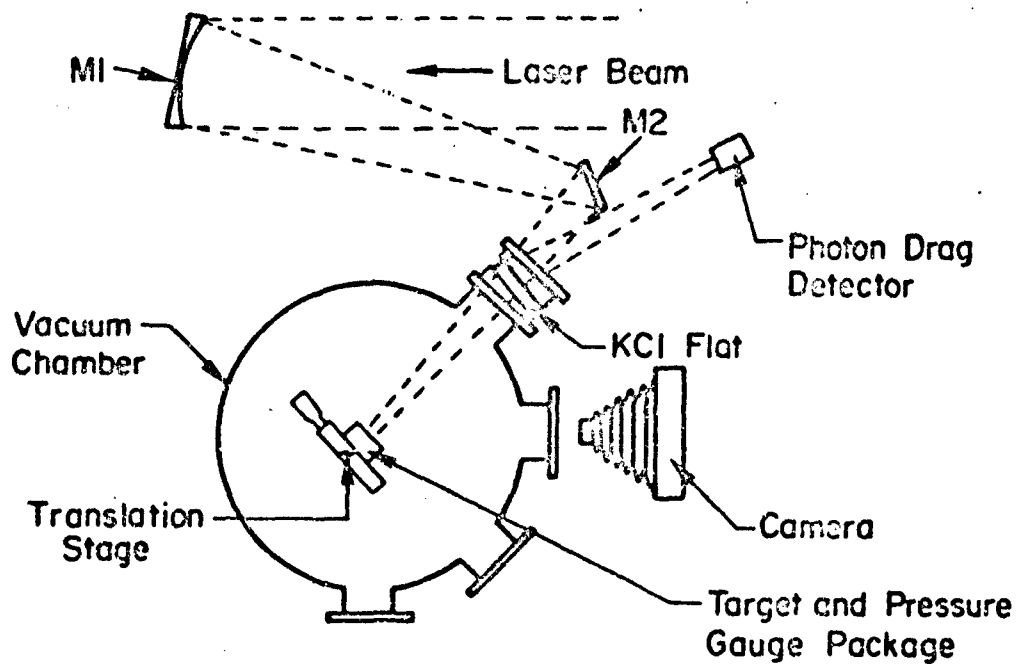


FIGURE 24. EXPERIMENTAL ARRANGEMENT FOR MEASUREMENT OF LASER-INDUCED SHOCK PRESSURES

circuitry. Measurements involving the quartz gauges were relatively straightforward as they did not involve the use of a gauge power supply; the signal cable was terminated by 50  $\Omega$  at the oscilloscope (TEK 7704) which was triggered by the photon drag detector as previously described. The carbon gauge measurements involved the use of considerably more circuitry as shown by the block diagram in Figure 25. When externally triggered, the laser has a delay of 3.9  $\mu$ sec until peak optical output, with a jitter of  $\approx 0.3$   $\mu$ sec. Furthermore, the pulsed constant-voltage power supply (Pulsar Associates model 151) has a "settling time" of  $\approx 4$   $\mu$ sec. To avoid having any laser energy on target during the power supply settling duration, a fixed electronic delay of 2  $\mu$ sec was introduced in the laser trigger cable. The oscilloscope was again triggered by the photon drag detector giving the same timing relationships as with the quartz gauge measurements; in this manner relevant timings are unaffected by laser trigger jitter. The pulsed constant-voltage power supply employs a balanced bridge circuit with the 50  $\Omega$  carbon gauge forming one arm of the bridge. The change in gauge resistance under stress unbalances the bridge and gives an output signal proportional to the instantaneous pressure. To minimize gauge ohmic heating, the 100 V supply was crowbarred after 60  $\mu$ sec. Under these conditions the gauge dissipates 3 mJ of electrical energy and negligible baseline drift was observed.

#### Laser Beam Parameters

All experiments were performed with Battelle's 80 J-TEA CO<sub>2</sub> laser which has a peak power of  $1.7 \times 10^8$  watt. The pulse shape (see Figure 19) is characterized by an intense spike of width 80 nsec (FWHM) followed by a N<sub>2</sub>-deexcitation tail lasting several microseconds. The spot size and intensity distribution for the present experiments were the same as reported previously in Reference (2). The effective 1/e area was 0.29 cm<sup>2</sup> and the peak power density,  $G_{p2}$ , ranged from a maximum of  $5.8 \times 10^8$  watt/cm<sup>2</sup> to  $3.2 \times 10^7$  watt/cm<sup>2</sup>.

Of particular importance is the delay time between laser light first on target and oscilloscope trigger. Because of the particular experimental arrangement using the photon drag detector as an external trigger source,



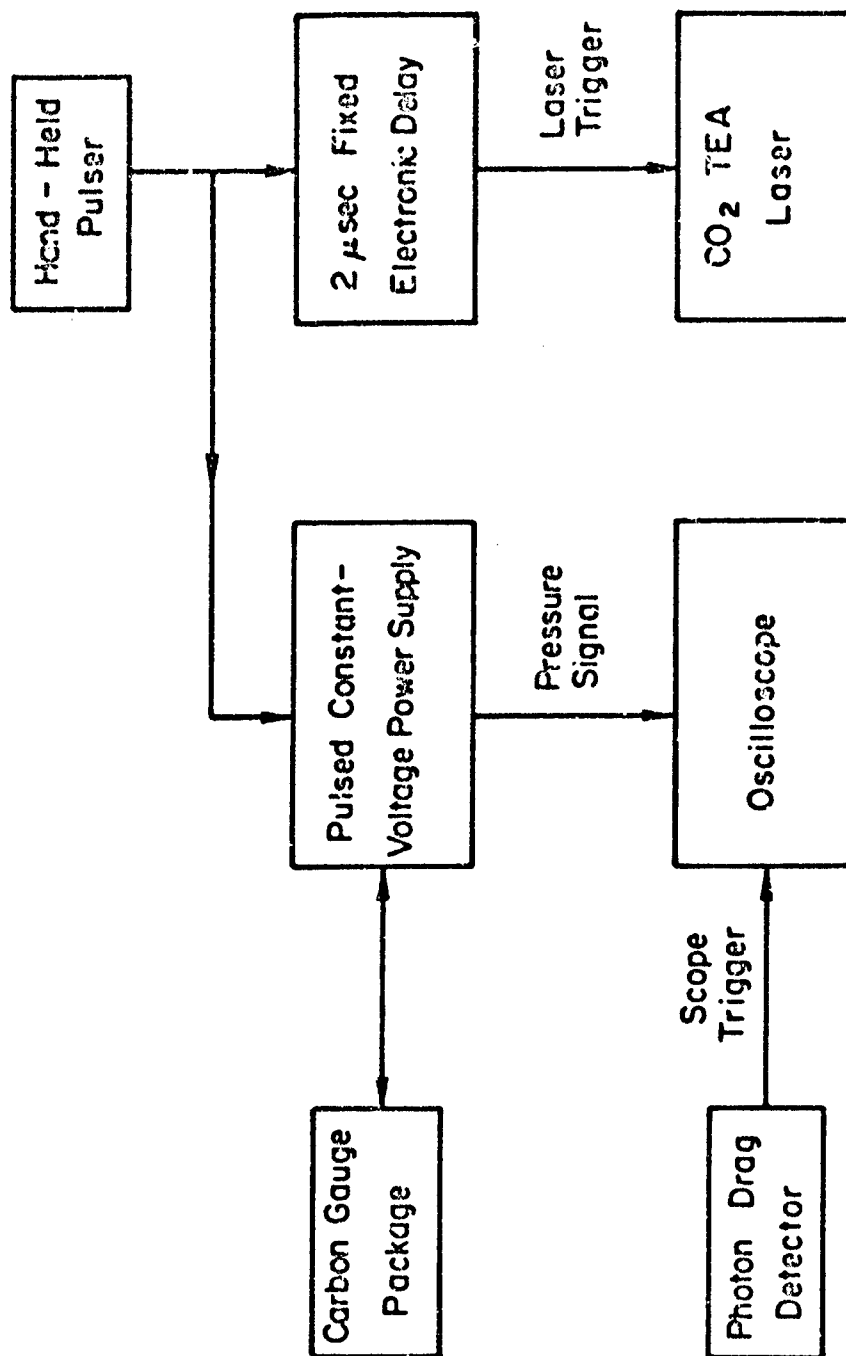


FIGURE 25. BLOCK DIAGRAM OF THE ELECTRONIC CIRCUITRY EMPLOYED WITH THE CARBON PIEZORESISTIVE GAUGE MEASUREMENTS

delay time is not constant, but is rather a function of peak power density, as shown in Figure 26. This delay was accounted for in analysis of the data.

#### Gauge Package Designs

Back-surface and in-material pressure measurements were performed with quartz piezoelectric<sup>(58,59)</sup> and carbon piezoresistive<sup>(60)</sup> gauges, respectively. Quartz gauges are well-matched acoustically<sup>(61)</sup> to aluminum alloys, give fast response, and do not suffer from baseline shift problems encountered with piezoresistive devices due to ohmic heating. They are, however, limited in usefulness to their characteristic writing time. When a back-up plate is not employed, this writing time is equal to the single-pass acoustic transit time. Carbon gauges may, on the other hand, have long writing times limited in principle only by the target dimensions in which they are embedded. Although slower in response time than quartz gauges,<sup>(43)</sup> they are especially well-matched acoustically<sup>(61)</sup> to most plastic materials. We have attempted to strengthen our confidence in these data by performing both back-surface and in-material measurements. Gauge package materials used in the experiments with relevant properties are listed in Table 6.

The quartz gauge and target package are shown in Figure 27. Right-circular cylindrical disks of X-cut quartz are employed as the active elements in a shorted guard-ring design. The discs are 0.70 cm in diameter x 0.127 cm thick with an inner electrode diameter of 0.318 cm. Reference (59) shows that shorted gauges do not respond in an equivalent manner to the more widely-used shunted gauges until  $w \geq 3.0 l$  is achieved, where  $w$  is the guard-ring width and  $l$  is the disk thickness. For these gauges  $w/l = 1.5$ , a necessary compromise to obtain useful output signals for low-pressure shots while maintaining the inner electrode diameter less than the characteristic laser focal spot size. For this configuration, a writing time of 220 nsec was obtained. Targets were gently held against the gauges by a three-point spring-loaded holder as shown in Figure 27 with a thin layer of Dow Corning high-vacuum silicone grease applied to the interface.

Carbon gauge packages are shown in Figure 28. The carbon gauges have active elements 1.3 x 1.5 mm square which are bonded between Kapton<sup>®</sup> insulating films 0.01 mm thick giving an overall thickness of 0.036 mm.

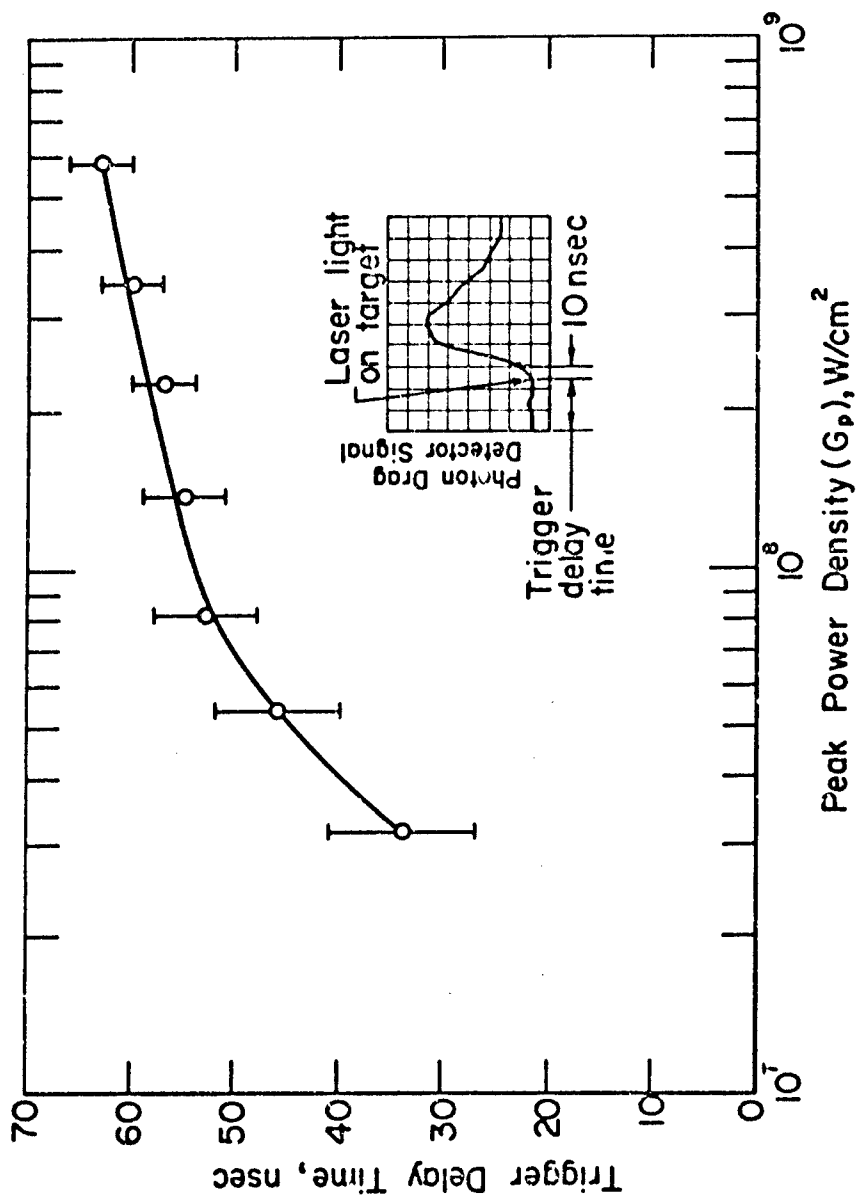


FIGURE 26. OSCILLOSCOPE TRIGGER DELAY AS A FUNCTION OF  
PEAK POWER DENSITY ON TARGET

TABLE 6. MATERIAL COMPOSITION AND PROPERTIES FOR QUARTZ AND CARBON GAUGE PACKAGES. ACOUSTIC VELOCITY AND IMPEDANCE DATA TAKEN FROM REFERENCE 61.

Material	Thickness	Diameter	Acoustic Transit Time (thickness dimension)	Acoustic Impedance, $Z$ ( $\text{gm}/\text{cm}^2\text{-}\mu\text{sec}$ )
Quartz Gauge Packages:				
3003-H14 (a) Aluminum Targets	0.406 mm	11.4 mm	77±6 nsec	1.46
Cellulose Acetate (b) Targets	0.356 mm	11.4 mm	162±20 nsec	0.3
X-cut Quartz Gauge	1.27 mm	7.0 mm	220±5 nsec	1.518
Carbon Gauge Packages:				
3003-H14 (a) Aluminum Targets	0.406 mm	5 cm	77±6 nsec	1.46
6061-T6 Aluminum Backup Discs	3.18 cm	5 cm	6.1 $\mu\text{sec}$	1.41
Cellulose Acetate (b) Targets	0.356 mm	5 cm	162±20 nsec	0.3
PMMA Targets	1.50 mm	5 cm	546±20 nsec	0.326
PMMA Backup Discs	3.18 cm	5 cm	11.6 $\mu\text{sec}$	0.326

(a) Acoustic velocity and impedance assumed approximately equal to those values for 2024 aluminum.

(b) Acoustic velocity and impedance assumed approximately equal to those values for mylar.

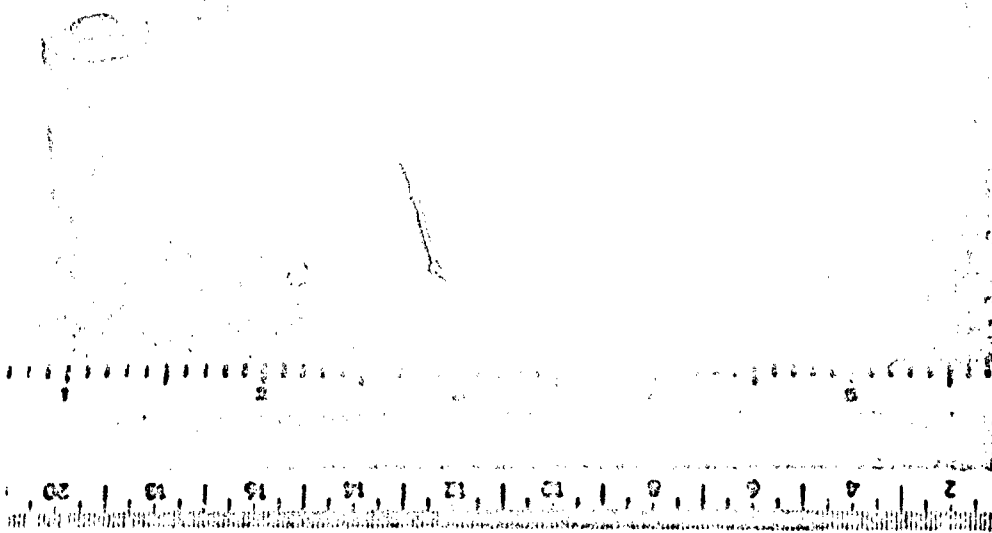


FIGURE 27. QUARTZ PIEZOELECTRIC GAUGE AND ASSEMBLED  
GAUGE PACKAGES WITH ALUMINUM TARGETS

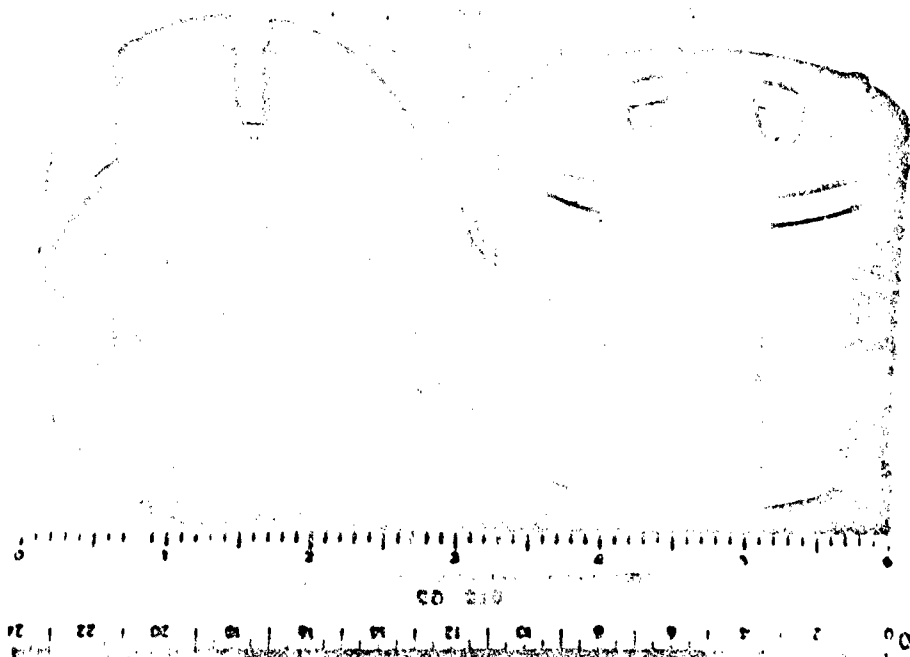


FIGURE 28. ASSEMBLED CARBON PIEZORESISTIVE GAUGE PACKAGES

The gauges are epoxied into a 0.1-mm deep groove on one end of the backup discs (5 cm dia. x 3.2 cm thick) such that the active carbon elements are centered with respect to the axis of the cylindrical disc. The backup discs are then lapped smooth and the target overlays are mated with a thin layer of Dow Corning 710 silicone fluid or epoxy in the case of packages used at low pressures. The carbon elements are within 0.08 mm of the target overlay-backup disc interface. The assembly is then installed in a shielded holder. Both aluminum and plastic gauge packages were prepared in this manner. Gauge responses were found to be identical for packages with the target overlay epoxied or mated with silicone fluid. Only at low ambient pressures was it necessary to use the epoxied target overlays due to bubble formation at the silicone fluid interface in the gauge packages with replaceable target overlays.

#### Pressure Response of Aluminum Targets

Representative pressure histories in aluminum measured with carbon gauge packages are shown in Figure 29. Above LSD-wave threshold [Figure 29 (a-c)], the pressure response is characterized by a large compressional stress followed by a tensile relief wave and then an overpressure response as the blast wave pressure decreases to the ambient pressure. For these data, the width of the compressional wave is  $\approx 600$  nsec (FWHM) for the 0.406-mm targets at 760 torr ambient pressure and  $3.48 \times 10^8$  watt/cm<sup>2</sup> peak power density; for the same conditions and  $G_p = 1.39 \times 10^8$  watt/cm, the width is  $\approx 800$  nsec (FWHM). For the quartz gauges under similar experimental conditions, the peak pressure is barely reached before the writing time (220 nsec), which implies that the carbon gauges have a response time of 50-100 nsec. This estimate is consistent with the observations of Lowder and Pettingill.<sup>(43)</sup> We performed one experiment using a 0.025-mm foil target with a quartz gauge to assess the effect of pressure wave attenuation in the target on the peak pressures recorded. For an ambient pressure of 760 torr and a peak power density of  $1.39 \times 10^8$  watt/cm<sup>2</sup>, the peak pressures were in close agreement with those obtained with 0.406-mm thick targets [see Figure 31 (a)]; however, the recorded width of the compressional wave was only 190 nsec (FWHM). In general, the width decreases

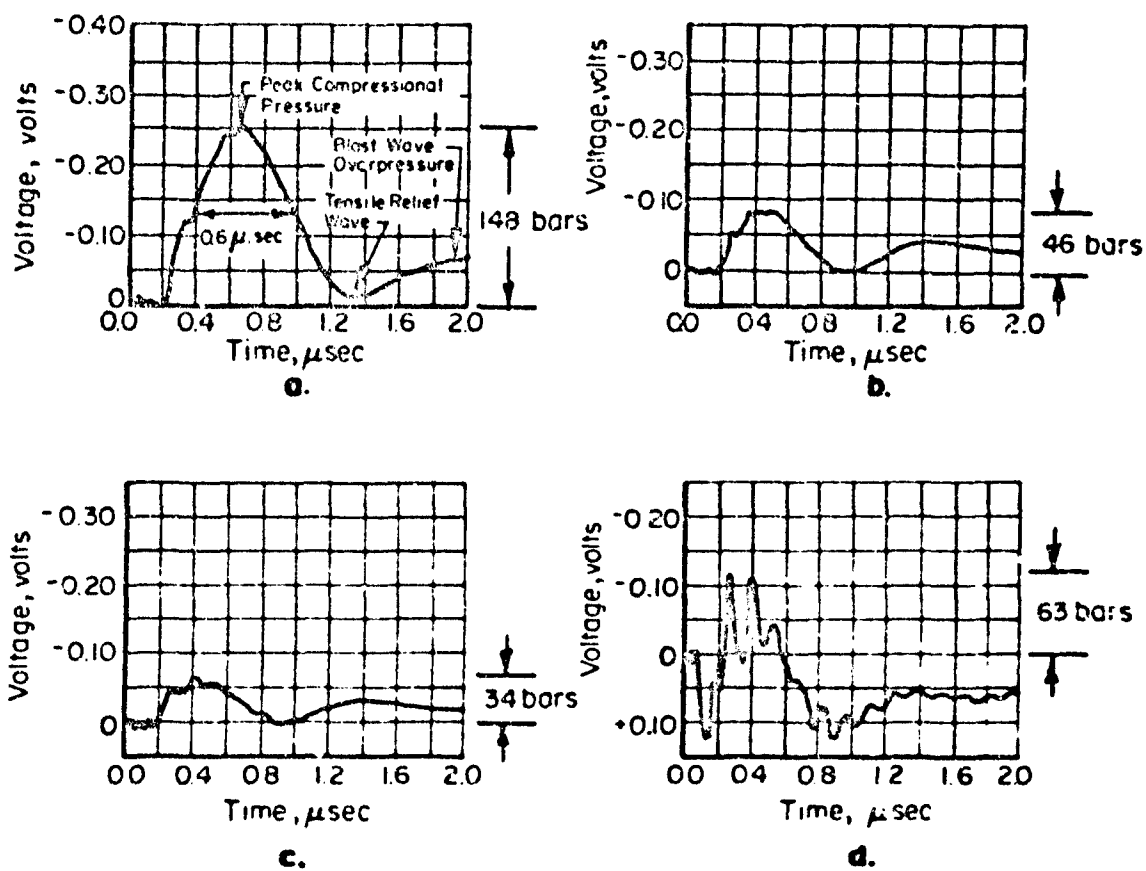


FIGURE 29. REPRESENTATIVE PRESSURE HISTORIES WITH ALUMINUM TARGETS AND CARBON GAUGE PACKAGES FOR  $G_p = 3.48 \times 10^8 \text{ watt/cm}^2$  AND AMBIENT PRESSURES OF (a) 760, (b) 125, (c) 40, and (d) 2 TORR

with decreasing ambient pressure and with increasing peak power density. For irradiations below LSD-wave threshold, the pressure is generated by hydrodynamic blowoff of target material. The pressure spike is of much shorter duration than observed above LSD-wave threshold, and the output of the carbon gauge package rings due to the acoustic mismatch of the embedded carbon element and surrounding plastic insulation with respect to the aluminum host. A typical pressure history in aluminum at 2 torr ambient pressure is shown in Figure 29(d).

The direct effect of LSD-wave initiation on aluminum pressure response is seen more clearly in the quartz gauge records for 2 and 10 torr ambient pressure at  $3.48 \times 10^8 \text{ watt/cm}^2$ , i.e., below and above the pressure threshold for initiation, respectively. These data are presented in Figure 30. Below threshold, the pressure rises rapidly to half maximum on a time scale of order 20 nsec and exhibits a double maximum which is characteristic of vacuum irradiations. Above threshold, the pressure rises gradually to half maximum at 90 nsec. The change in pressure signature is believed to result from reduction in vaporization by LSD-wave blockage of the laser radiation.

Analyses of these data are shown in Figure 31 where the peak shock pressure is shown as a function of ambient pressure for  $G_p = 1.39 \times 10^8$  and  $3.48 \times 10^8 \text{ watt/cm}^2$ . Both quartz and carbon gauge measurements are shown, but because of the limited response time of the carbon gauges, the peak pressure is not well-resolved and the carbon gauge measurements lie below those which employed quartz gauges. At low pressures, the carbon gauges are completely inadequate for resolving the peak pressure which results from the short-duration metal-vapor blowoff. Since very little material is removed for shots above the LSD threshold, repeated use of the same target introduces negligible scatter in the data. Below LSD threshold, however, the surface condition influences the coupling of laser light. The repeated use of targets when below LSD-wave thresholds may explain the scatter in the quartz data in this regime.

An effort was made to relate these data to simple theoretical models based on a cylindrical blast wave. According to the theory of Pirri,<sup>(49)</sup> the maximum surface pressure occurs when the laser pulse is on and the flow



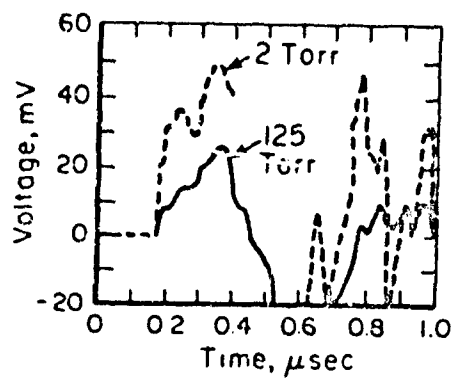


FIGURE 30. REPRESENTATIVE PRESSURE HISTORIES WITH ALUMINUM TARGETS AND QUARTZ GAUGE PACKAGES FOR  $G_p = 3.48 \times 10^8 \text{ watt/cm}^2$  ABOVE (10 torr) AND BELOW (2 torr) THE AMBIENT PRESSURE THRESHOLD FOR LSD WAVE INITIATION

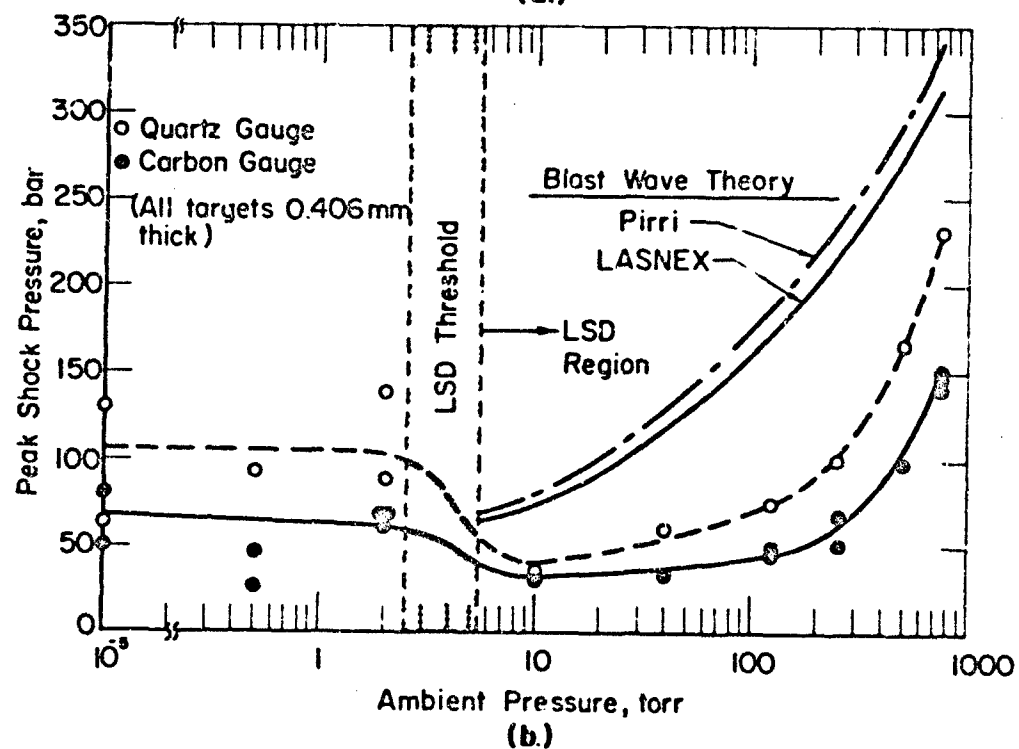
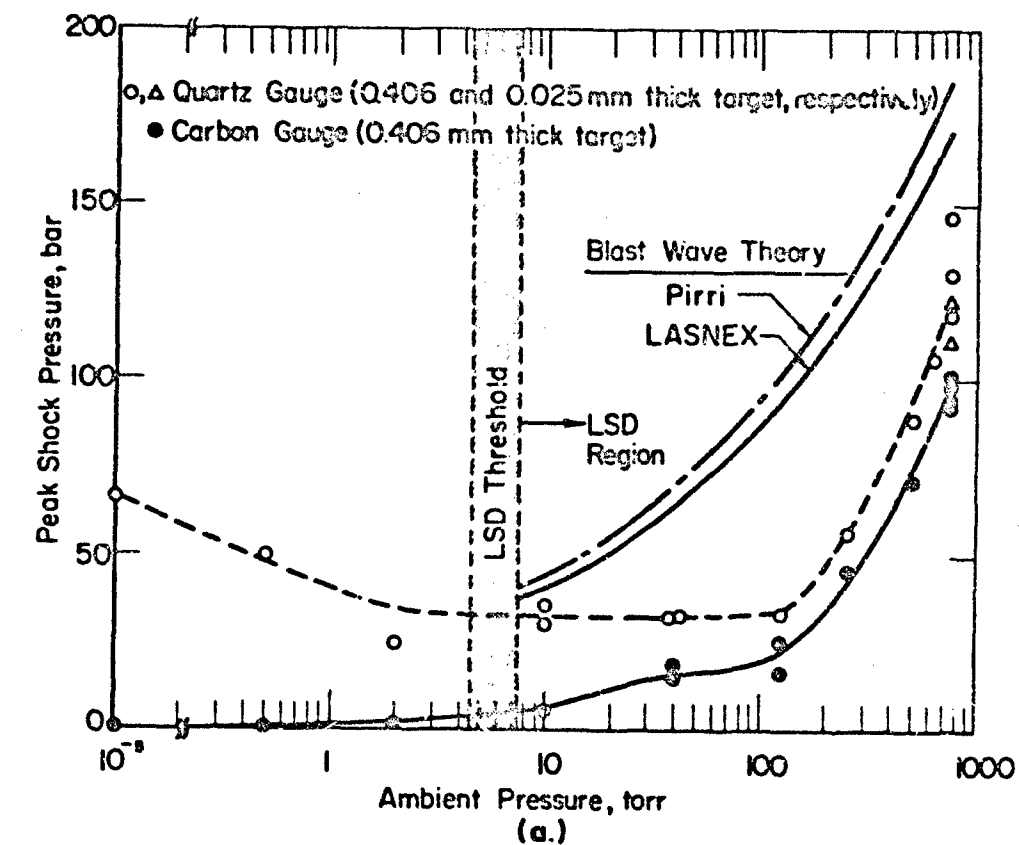


FIGURE 31. PEAK SHOCK PRESSURES IN ALUMINUM AS A FUNCTION OF AMBIENT PRESSURE FOR  $G_p = 1.39 \times 10^8 \text{ watt/cm}^2$  (a) AND  $G_p = 3.48 \times 10^8 \text{ watt/cm}^2$  (b)

geometry is one-dimensional. This surface pressure,  $P$ , is related to the pressure behind the detonation wave,  $P_{DW}$ , by

$$P = [(\gamma+1)/(2\gamma)]^{2\gamma/(\gamma-1)} P_{DW}, \quad (8)$$

where

$$P_{DW} = \rho_0 V_{DW}^2 / (\gamma+1). \quad (9)$$

The velocity with which the detonation wave moves away from the surface was first derived by Raizer<sup>(62)</sup> as follows:

$$V_{DW} = [2(\gamma^2-1)G/\rho_0]^{1/3}, \quad (10)$$

where  $\gamma$  is the ratio of specific heats of the air behind the detonation,  $G$  is the laser power density, and  $\rho_0$  is the ambient gas density in front of the wave. Performing the algebra and setting  $\gamma = 1.1814$ , we find that the surface pressure (bars), ambient density ( $\text{gm}/\text{cm}^3$ ), and laser power density ( $\text{watt}/\text{cm}^2$ ) are related by

$$P = 6.43 \times 10^{-3} \rho_0^{1/3} G^{2/3}. \quad (11)$$

The results of Edwards et al.<sup>(57)</sup> obtained by a parameter study employing the LASNEX code in one dimension with constant power density may be summarized by

$$P = 5.83 \times 10^{-3} \rho_0^{1/3} G^{2/3}, \quad (12)$$

where the units are identical to those in Equation (11). Equations (11) and (12) are plotted in Figure 31 with  $G = G_p$  and  $\rho_0$  (760 torr) =  $1.29 \times 10^{-3} \text{ gm}/\text{cm}^3$  for conditions above LSD-wave thresholds.

The cylindrical blast wave theory overpredicts the measured surface pressure. We note that the measurement of peak pressures with small but finite thickness targets is representative of the peak surface pressure, and minimal attenuation is observed as evidenced by comparisons using 0.025- and 0.406-mm thick targets. Implicit in the theory<sup>(49)</sup> are the assumptions

of an ideal square-wave laser pulse (constant intensity for the pulse width  $\tau_p$ ), uniform intensity over the focal spot, and uniform surface initiation. None of these conditions hold in our experiments, but it is probably the latter assumption which causes the greatest discrepancy for the experiments discussed here. It is now well established by LSD-initiation studies that initiation is highly local on a practical aluminum surface at defect sites. Individual "micro-LSD waves" propagate out from the surface, spread laterally, and presumably "linkup" to form a front at a small, but finite distance from the surface. While the local pressure behind each micro-LSD wave front might be well-characterized by theory, the average surface pressure (that which is ultimately recorded by the gauge) would be expected to be lower than in the case of uniform initiation on the surface because of the large fraction of unheated air in the former case. This effect also appears to explain the slow rise of pressure to its maximum value which occurs at 200-300 nsec at atmospheric pressure well after the laser pulse maximum at 55 nsec.

Information about the blast wave can be obtained also by an analysis of the pressure histories measured as a function of radius. Surface pressures should be generated by the expanding cylindrical blast wave outside of the focal spot region, for instance. The effect of power density distributions within the focal spot should be observed. Maps of the peak shock pressure as a function of radial position are shown in Figure 32, where the entire carbon gauge package and aluminum target were translated horizontally across and beyond the focal region. The procedure was begun at the origin, and, once the radial translation for given conditions was completed, the micrometer setting was returned to the origin to check for positioning accuracy. Within a very small experimental error, the pressure histories were identical. To confirm the alignment procedure for locating the origin, the gauge package was translated 0.635 mm in the opposite direction. Shots taken in this position gave less peak pressure than when located at the origin thus lending credibility to the alignment. At 1 atm, these data show large spatial pressure gradients within the focal region behind the LSD wave and an almost constant peak pressure for the surface outside of the focal spot due to the radially expanding cylindrical blast wave. At lower ambient pressures, the peak shock pressures and their spatial gradients are lower

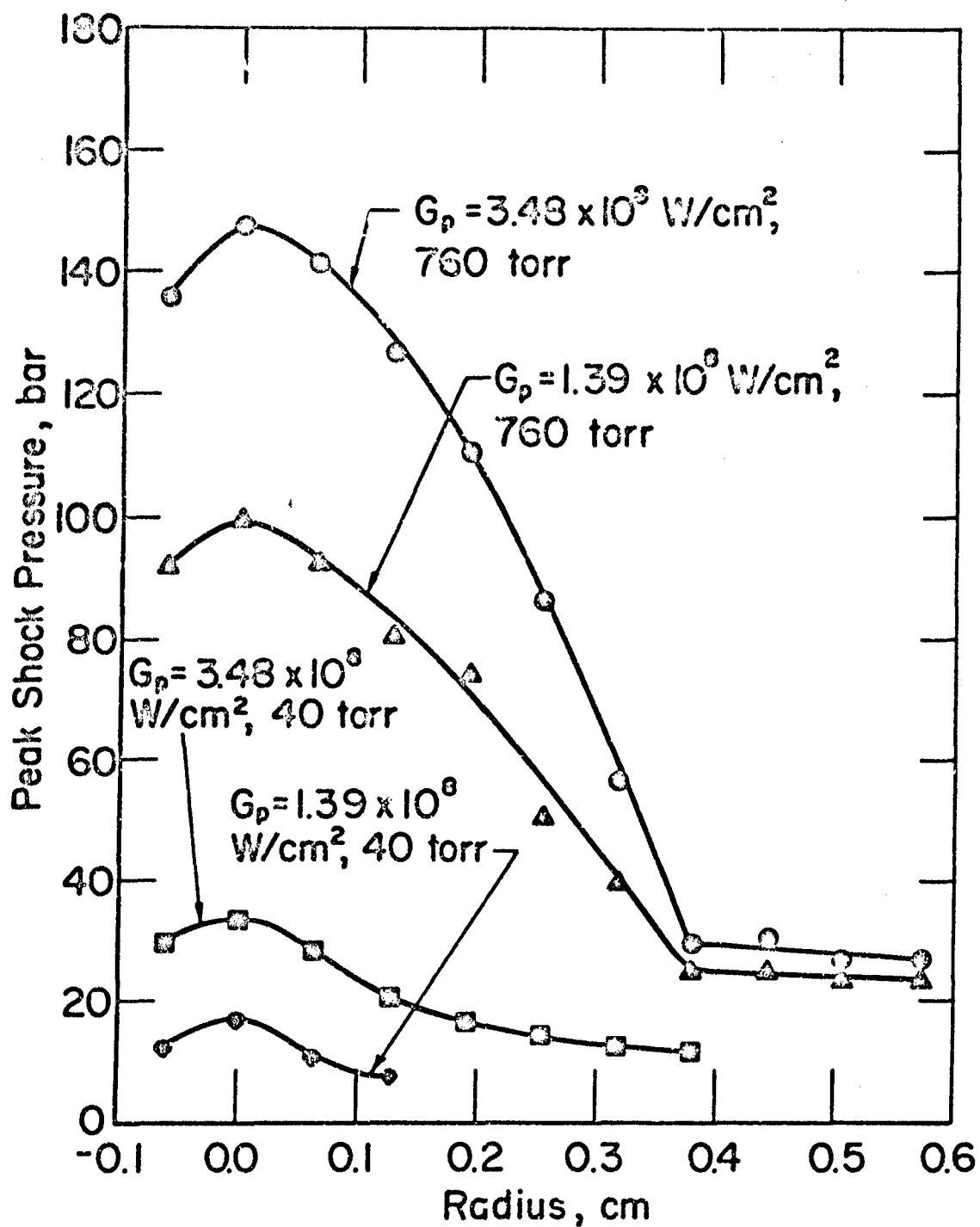


FIGURE 32. PEAK SHOCK PRESSURE IN ALUMINUM AS A FUNCTION OF TARGET RADIUS (CARBON GAUGE DATA)

than those at atmospheric conditions. The need for accurate spatial characterization of the laser focal spot when using computer simulation models is confirmed by these data.

Additional diagnostic information regarding the cylindrical blast wave can be obtained from the temporal characteristics of the pressure histories as a function of radius. In particular, we have plotted the arrival time of the peak compressional wave relative to the onset of laser radiation as a function of radius in Figure 33. Data were analyzed from the same shots as in Figure 32, and since the symbol usage in Figures 32 and 33 is the same, data from one figure may be readily related to the other. A comparison of these data and predictions based on simple, analytical cylindrical blast wave models was again sought. Nielsen<sup>(51,56)</sup> has derived a simple expression for the time at which the blast wave arrives at the radial coordinate  $r$ , namely

$$t_b(r) = (r^2 - r_0^2) / (2cr_0) \quad r \geq r_0, \quad (13)$$

where  $r_0$  is the focal spot radius and  $c$  is the acoustic speed behind the detonation wave, i.e.,

$$c = (\gamma P_{DW} / \rho_{DW})^{1/2}, \quad (14)$$

where  $P_{DW}$  and  $\rho_{DW}$  are the gas pressure and density behind the wave.  $P_{DW}$  is given by Equation (9), and the density behind the detonation wave and the unshocked density are related by<sup>(62)</sup>

$$\rho_{DW} = (\gamma + 1) \rho_0 / \gamma. \quad (15)$$

Now we have plotted the time of the peak compressional wave,  $t_c$ , and not the blast wave arrival time, so we assume that

$$t_c(r) = t_b(r) + t_0 \quad r \geq r_0, \quad (16)$$

where  $t_0$  is the experimentally measured delay between laser onset and the peak compressional wave at  $r = 0$  measured at the surface for given conditions of ambient pressure and peak power density. To first approximation, the

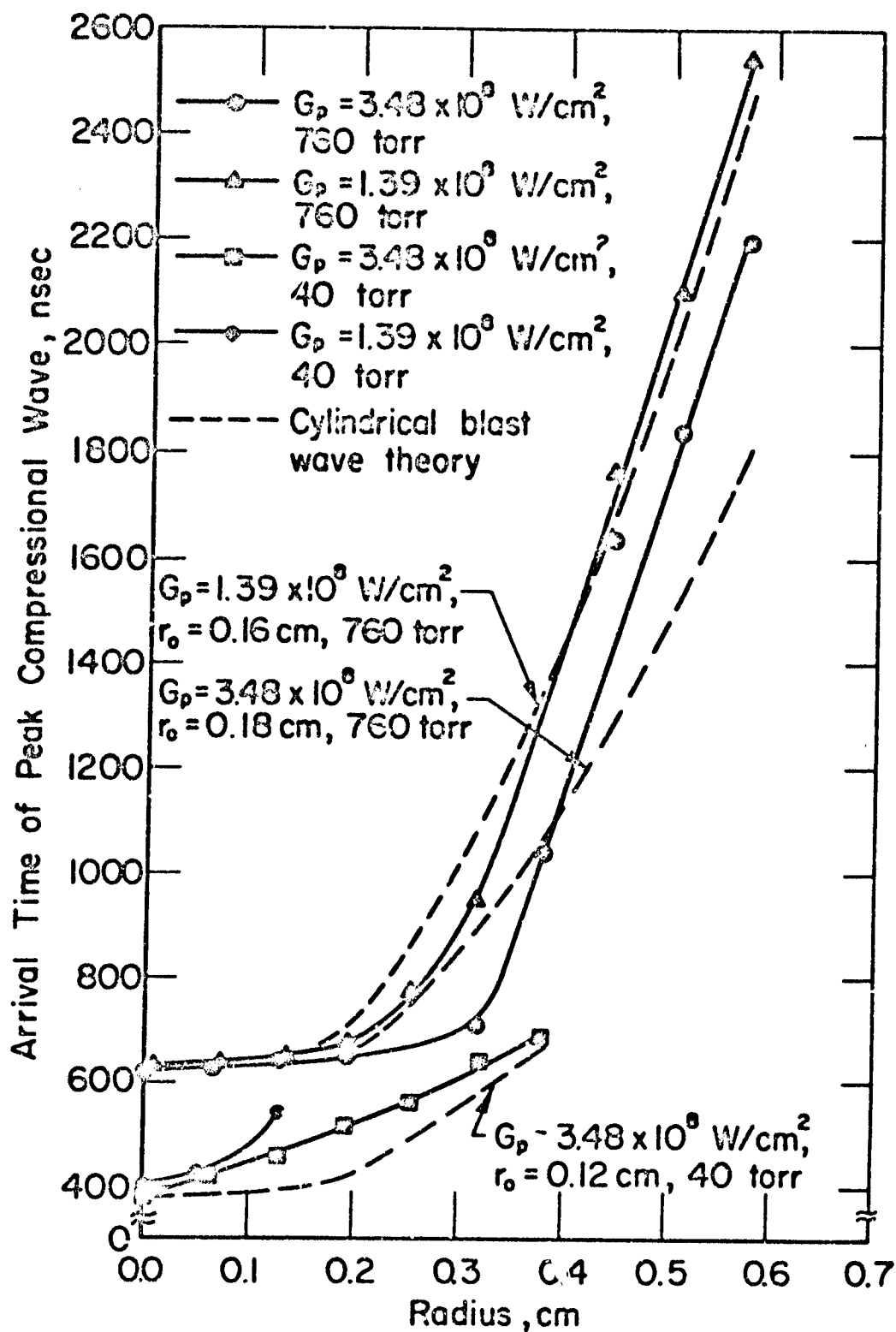


FIGURE 33. ARRIVAL TIME OF THE PEAK COMPRESSONAL WAVE IN ALUMINUM AS A FUNCTION OF TARGET RADIUS (CARBON GAUGE DATA)

response time of the carbon gauge does not affect the comparison between theory [Equation (16)] and experiment since this additional delay is accounted for in the value of  $t_0$ . As shown in Figure 33, the agreement between theory and experiment is good only when values of the laser focal spot radius smaller than the effective  $1/e$  radius are assumed, i.e.,  $r_0 < D_g/2$  where  $D_g/2 = 0.31$  cm. If we set  $r_0 = 0.31$  cm in the calculations, then expansion velocities much larger than experimentally measured are calculated for  $r > r_0$ , and the agreement is poor. Because of the spatial distribution of laser radiation, it is reasonable to assume that the effective radius of the cylindrical plasma column is less than the effective  $1/e$  radius of the laser beam at focus. Inclusion of the spatial characteristics of the laser beam into theoretical models is again seen to be necessary. It is interesting to note that since the target overlay is of finite thickness, a small shear wave precursor should be detected for measurements taken outside of the focal region. This was observed, in fact, and the arrival time as a function of radius did behave temporally as would be expected for a shear wave with velocity  $c_s = 3.2$  mm/ $\mu$ sec.<sup>(61)</sup> Hence, the compressional wave histories were due entirely to blast wave effects, and no interference with shear wave signatures was observed.

#### Pressure Response of Plastic Targets

The pressure response of plastic targets is expected to be different from aluminum targets in air because of significant surface vaporization even under conditions which generate LSD waves. Lowder and Pettingill<sup>(43)</sup> observed a  $3/2$  power dependence of peak pressure on peak power density with PMMA targets and atmospheric pressure for long-pulse  $\text{CO}_2$ -laser irradiations. This may be contrasted with the  $2/3$  power dependence expected for a pure LSD-wave response as shown in Equation (11). For the data presented here, a fresh target was used on each laser shot unless otherwise noted. Noticeable surface ablation was observed for all conditions of ambient pressure and peak power density reported.

Representative pressure histories recorded with carbon gauge packages are shown in Figure 34. The rise time of the compressional wave is probably limited by the gauge response time, but is considerably faster



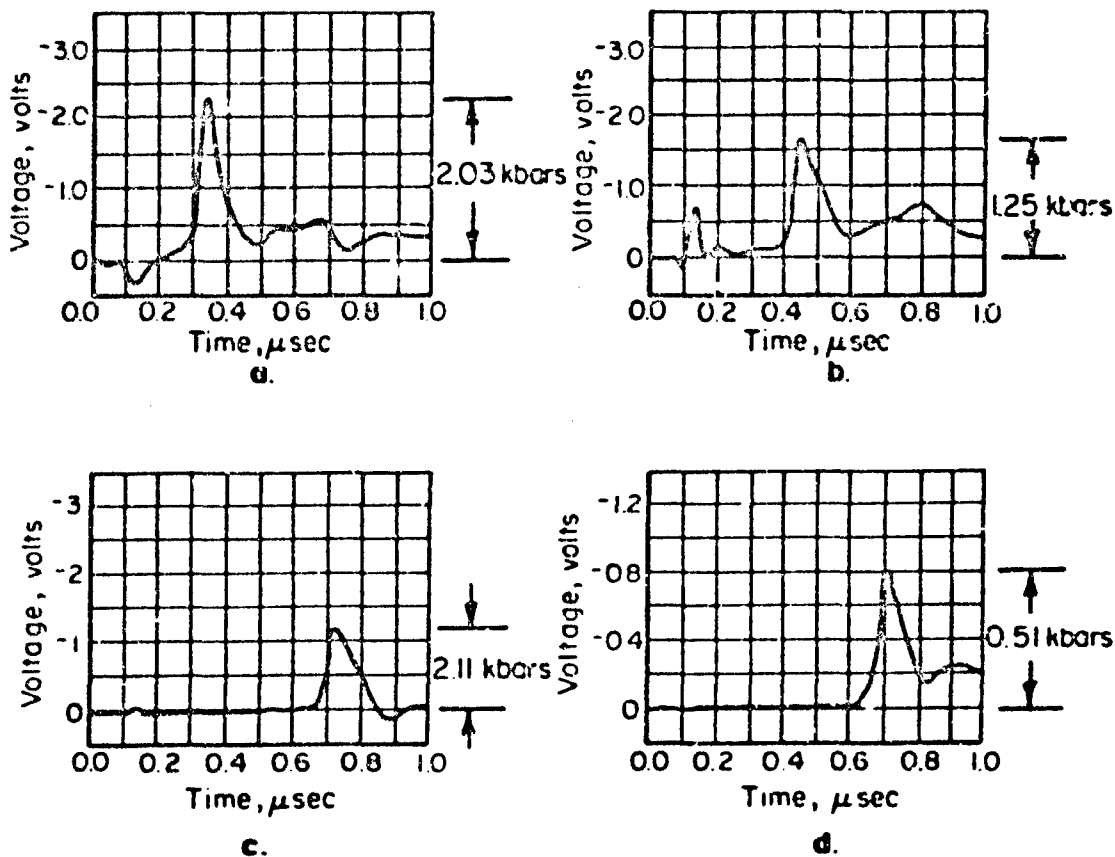


FIGURE 34. REPRESENTATIVE PRESSURE HISTORIES WITH PLASTIC TARGETS AND CARBON GAUGE PACKAGES: (a) AND (b), CELLULOSE ACETATE TARGETS,  $G_F = 3.48 \times 10^8 \text{ watt/cm}^2$ , AND AMBIENT PRESSURES OF 760 AND 125 TORR, RESPECTIVELY; (c) AND (d), PMMA TARGETS, 40 TORR AMBIENT PRESSURE, AND  $G_p = 3.48 \times 10^8 \text{ watt/cm}^2$  AND  $1.39 \times 10^8 \text{ watt/cm}^2$ , RESPECTIVELY. TRACE (c) SHOWS THE SECOND SHOT ON THIS TARGET, AND NO WELL-DEFINED LSD WAVE WAS OBSERVED. TRACE (d), ALTHOUGH THE SIXTH SHOT ON THE TARGET, WAS TAKEN FOR CONDITIONS WHICH DID PRODUCE AN LSD WAVE.

than with aluminum targets for the same conditions. Although the width of the compressional wave is less than observed in aluminum, tensile relief and blast wave overpressure effects are still easily recognizable. There is transient behavior in these records which occurs too early to be realistically interpreted as shock effects. Furthermore, this prompt signal is reduced in the second shot and is virtually absent in subsequent shots [Figure 34(c,d)]. Occurring only in the plastic irradiations, this prompt signal is thought to be electromagnetic in origin, possibly in the u.v. or r.f. wavelength regions. Why the transient is positive going at higher ambient pressures and negative going below a certain ambient pressure is unclear (it should be noted that carbon gauge pressure histories are displayed inverted since a compressional wave produces a negative-going signal). Interestingly, a first-shot prompt bias effect<sup>(3)</sup> was seen in the electrostatic probe data for nonmetallic targets which was not seen for metallic targets.

A comparison of carbon and quartz gauge measurements of the pressure histories in cellulose acetate targets is shown in Figure 35. Care must be exercised in the interpretation of results from the quartz gauge measurements when plastic target overlays are used due to the acoustic mismatch of the two dissimilar materials. If a stress wave is propagating through one material having an acoustic impedance  $Z_1$  toward an interface with a second material having an acoustic impedance  $Z_2$ , then reflection and transmission of the incident stress wave will occur at the boundary. If the duration of the stress wave is much less than the characteristic transit times through the two materials and if the wave is propagating normal to the interface, then the transmitted and reflected stresses,  $\sigma_t$  and  $\sigma_r$ , are related to the incident stress,  $\sigma_o$ , by<sup>(63)</sup>

$$\sigma_t/\sigma_o = 2 Z_2/(Z_1+Z_2) \quad ; \quad (17)$$

$$\sigma_r/\sigma_o = (Z_2-Z_1)/(Z_1+Z_2) \quad , \quad (18)$$

where the relevant acoustic impedances are specified in Table 6. For our case of a wave propagating from cellulose acetate into X-cut quartz,  $\sigma_t/\sigma_o = 1.7$  and  $\sigma_r/\sigma_o = 0.7$ ; hence, a compressional wave in cellulose

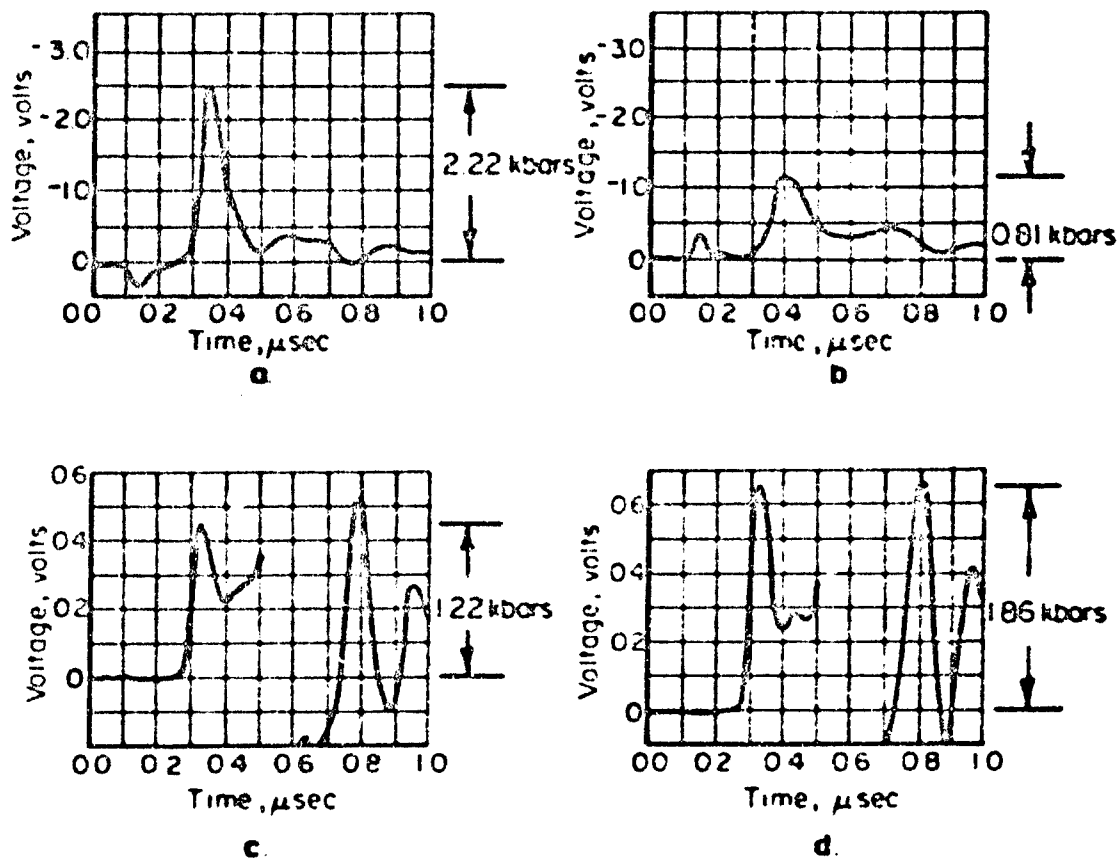


FIGURE 35. COMPARISON OF GAUGE RESPONSE WITH CELLULOSE ACETATE TARGETS FOR  $G_p = 1.39 \times 10^8 \text{ watt/cm}^2$ : (a) AND (b), PRESSURE HISTORIES TAKEN WITH CARBON GAUGE PACKAGES AT AMBIENT PRESSURES OF 760 AND 125 TORR, RESPECTIVELY; (c) AND (d), HISTORIES TAKEN WITH QUARTZ GAUGE PACKAGES FOR THESE SAME CONDITIONS

acetate will be transmitted into the quartz gauge at a higher pressure, and the width of the wave will be noticeably decreased.

The peak shock pressures in cellulose acetate and PMMA are shown as a function of the ambient pressure in Figure 36 and as a function of the peak power density in Figure 37. Also presented in the figure are LSD thresholds determined by photographic observation. It is important to note that at  $1.39 \times 10^8$  watt/cm<sup>2</sup>, there is an upper-limit pressure threshold for LSD waves. This implies that the LSD-wave threshold peak power density decreases with ambient pressure in the case of cellulose acetate as also observed by Maher et al.<sup>(16)</sup> for fused silica. The quartz gauge results have been left uncorrected for impedance mismatch and are presented for reference only. While discrepancies between the quartz gauge and carbon gauge results for plastics are not fully understood, the carbon gauge results alone appear to provide a valid representation of the response. The magnitude of the peak pressure response in all cases is very much greater than that which can be generated by LSD-wave pressures. This implies that the peak pressure response in the case of the plastics is dominated entirely by vapor blowoff. At  $G_p = 1.39 \times 10^8$  watt/cm<sup>2</sup>, the dependence of the peak shock pressure on ambient density has nearly a cylindrical blast wave proportionality of  $\rho^{-1/3}$  although strong LSD waves were not observed. At  $G_p = 3.48 \times 10^8$  watt/cm<sup>2</sup>, the dependence is more complex, presumably due to interference of the LSD wave with the target surface vaporization process. Likewise, the dependence of the peak shock pressure with laser peak power density at an ambient pressure of 760 torr appears to saturate at high intensities as shown in Figure 37. This saturation effect is also presumably a result of LSD-wave interference with vaporization. As may be noted in the figure, the highest value of peak pressure (2.2 kbar) occurs at  $1.39 \times 10^8$  watt/cm<sup>2</sup>, just below the LSD threshold level. This result is confirmed by the observation of the greatest extent of backsurface spallation occurring at this level. These short-pulse measurements thus give a different power dependence than observed in the long-pulse (1-5  $\mu$ sec) experiments of Lowder and Fettingill<sup>(43)</sup> mentioned above. For both  $D_g = 0.32$  and 0.8 cm, their data are accurately fitted by a  $3/2$  power dependence with peak power density; however, peak pressures of <0.2 kbar were measured<sup>(43)</sup> for  $G_p \leq 5 \times 10^8$  watt/cm<sup>2</sup>, whereas

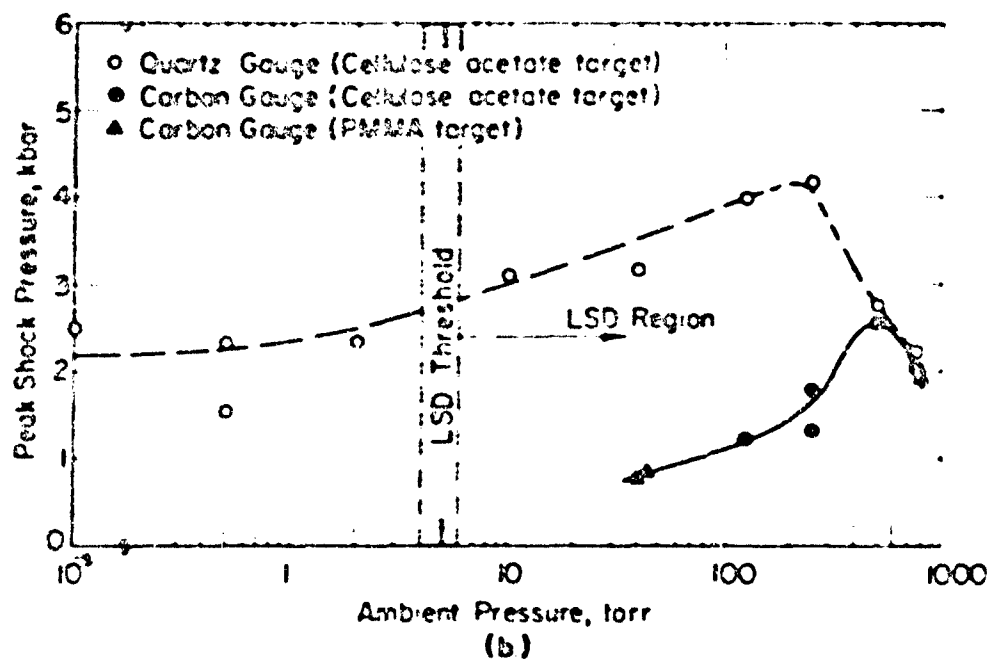
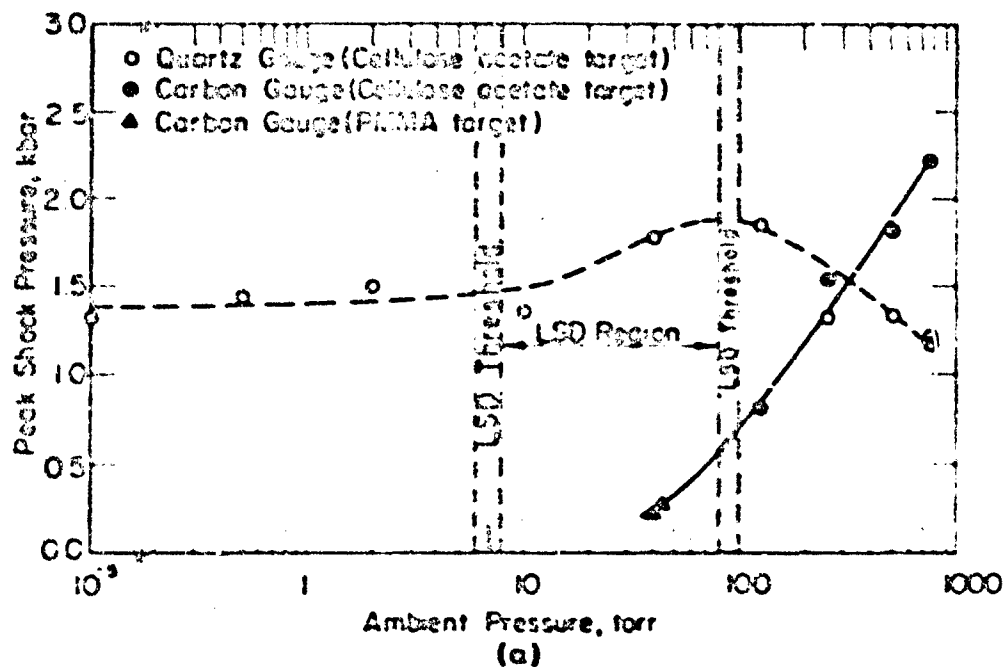


FIGURE 36. PEAK SHOCK PRESSURE IN CELLULOSE ACETATE AND PMMA AS A FUNCTION OF AMBIENT PRESSURE FOR

$$G_p = 1.39 \times 10^8 \text{ watt/cm}^2 \text{ (a) AND}$$

$$G_p = 3.48 \times 10^8 \text{ watt/cm}^2 \text{ (b)}$$

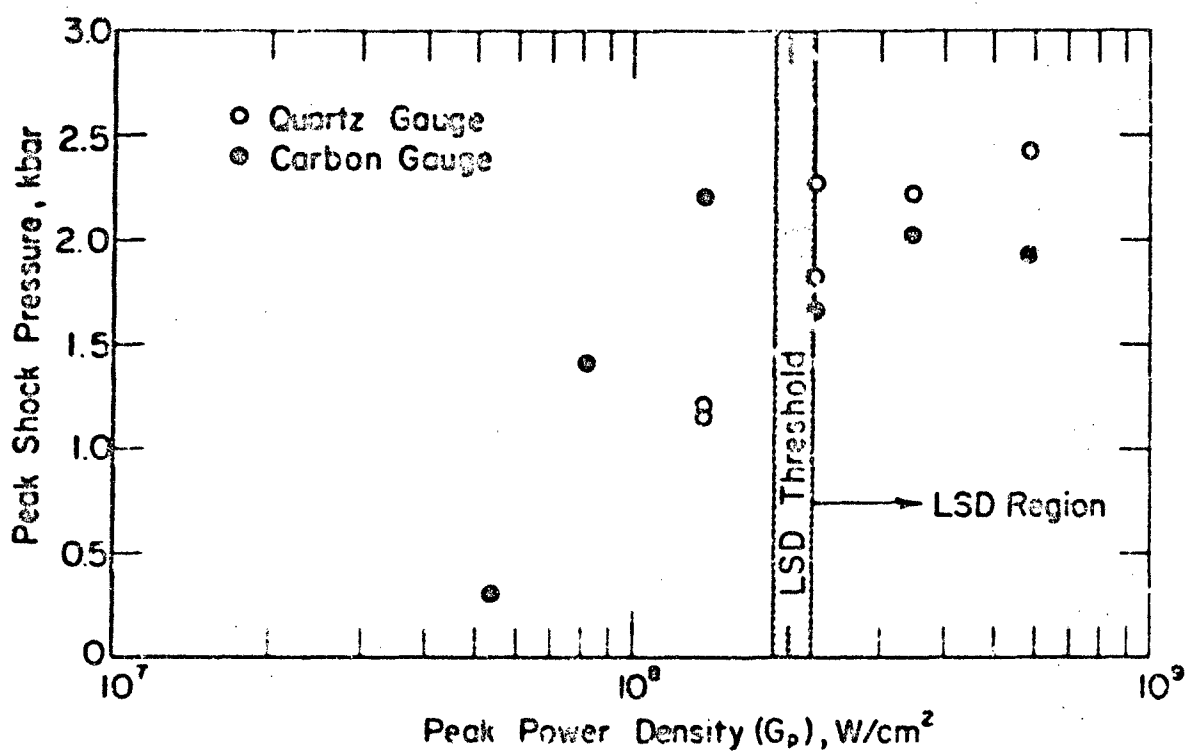


FIGURE 37. PEAK SHOCK PRESSURE IN CELLULOSE ACETATE AS A FUNCTION OF PEAK POWER DENSITY FOR AN AMBIENT PRESSURE OF 760 TORR

our data indicate peak pressures of  $\approx 2$  kbar for  $G_p \approx 5 \times 10^8$  watt/cm<sup>2</sup> and the short-duration TEA-laser pulse.

The effects of multiple shots on cellulose acetate targets are shown in Figure 38 for several experimental conditions. We have observed an increase in the peak shock pressure with the number of shots, especially at higher peak power densities and ambient pressures. After 3-5 shots, the peak shock pressure approaches an asymptotic limit with no further increases with additional shots, and the pressure histories become very reproducible.

#### LSD-Wave Initiation Times on Metallic and Nonmetallic Surfaces

We define the LSD initiation time as the delay between laser light arrival at the target and production of a plasma close to the surface. This protoplasma then launches an LSD wave under certain conditions of peak power density and ambient pressure. An initiation time can be calculated on the basis of pressure measurements as follows: the acoustic transit time through the target overlay and the laser trigger delay are subtracted from the time at which the first shock wave arrives at the gauges as recorded on the oscilloscope traces. These data are shown in Figures 39 and 40 for metallic and nonmetallic targets, respectively. In Figure 39, data points and error bars give the mean initiation values and standard deviation for several shots, while in Figure 40 the points are for single shots on fresh targets.

A comparison was made between initiation time measurements of Walters and Barnes<sup>(1,2)</sup> based on photometric, electronic, electrostatic, and spectroscopic techniques. These data confirm that initiation is prompt (30-60 nsec at atmospheric pressure) for practical aluminum targets with breakdown coming after a constant energy deposition of  $\approx 1.67$  J/cm<sup>2</sup>. The initiation time at 760 torr as inferred from quartz gauge pressure measurements is 10-20 nsec faster than observed by Walters and Barnes<sup>(1,2)</sup> as shown in Figure 39. The initiation times at lower ambient pressures are longer and represent a significant fraction of the laser pulse rise time.

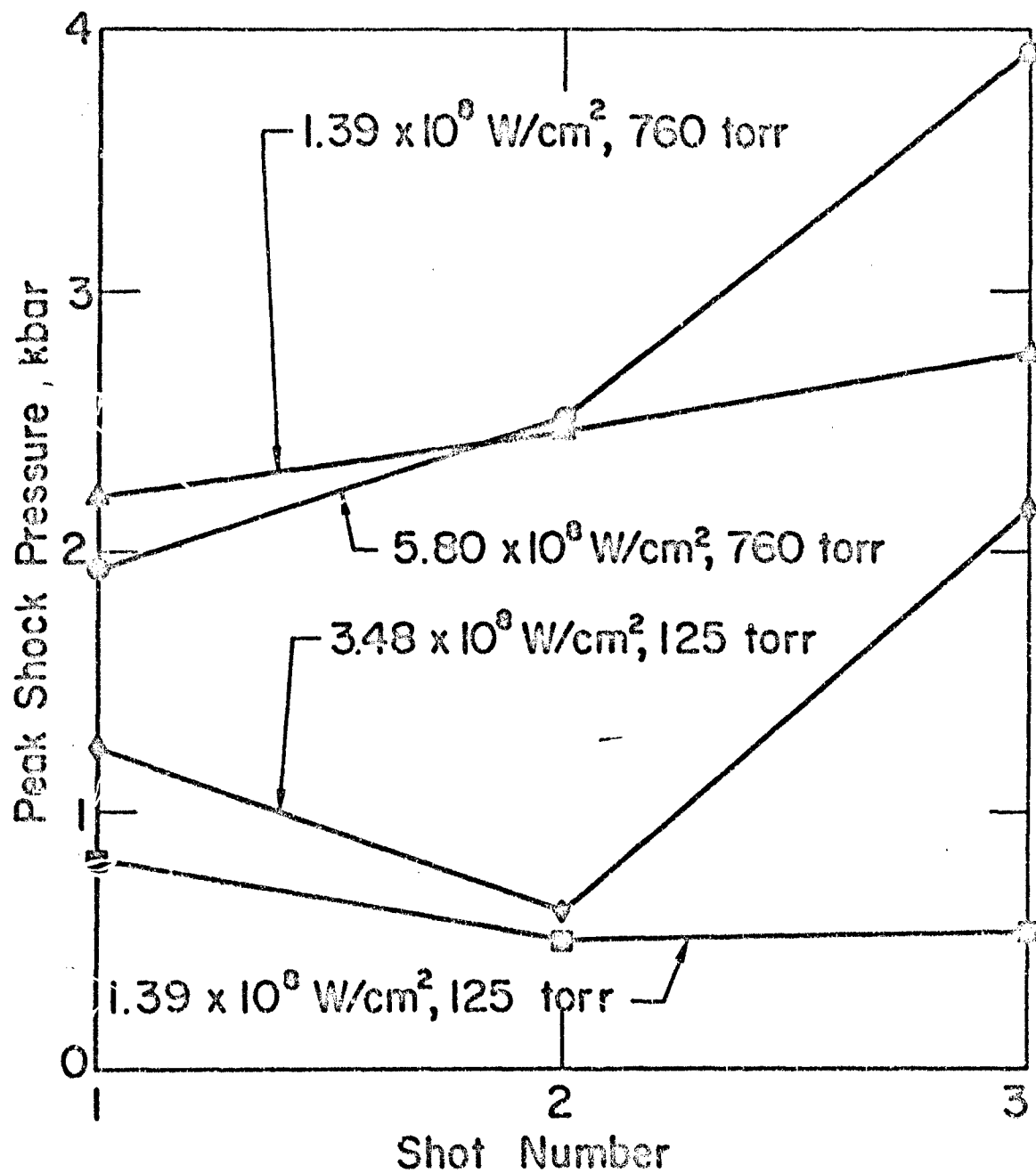


FIGURE 38. PEAK SHOCK PRESSURE IN CELLULOSE ACETATE AS A FUNCTION OF THE NUMBER OF SHOTS (CARBON GAUGE DATA)



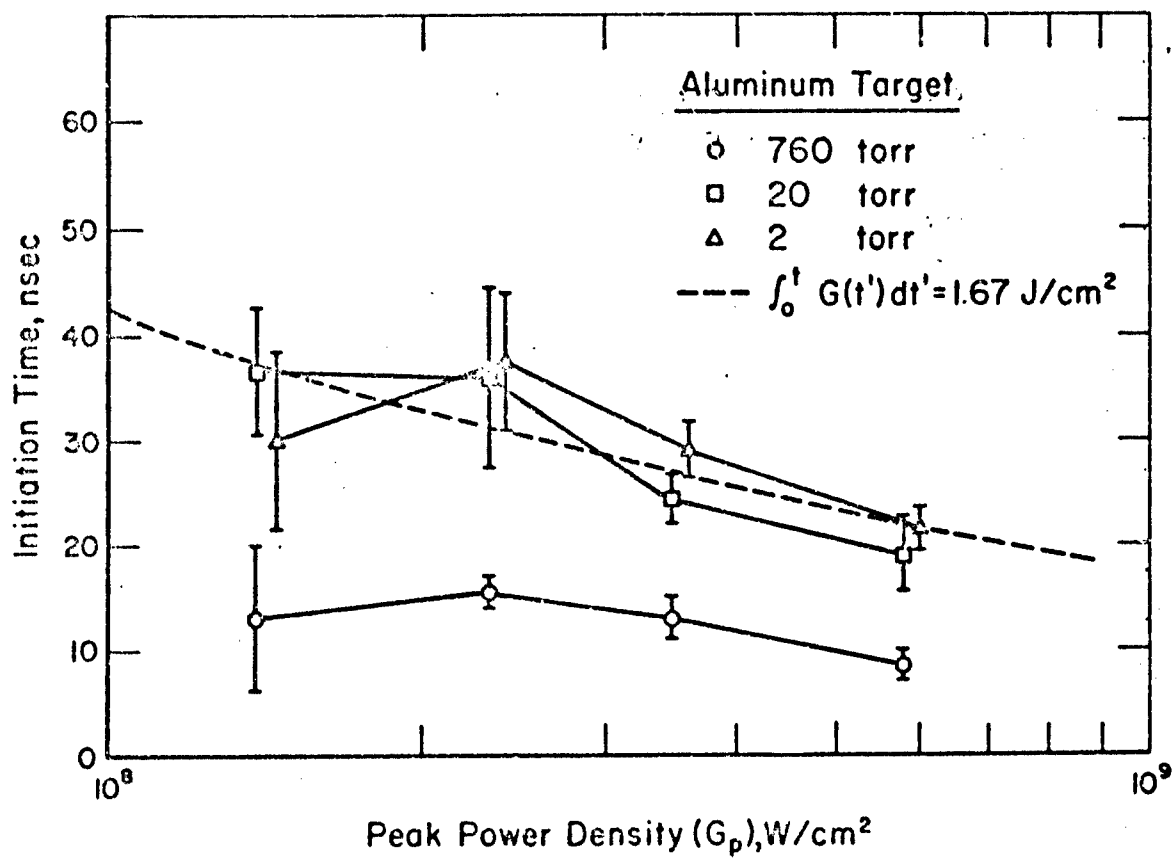


FIGURE 39. INITIATION TIME FOR ALUMINUM TARGETS AS A FUNCTION OF PEAK POWER DENSITY AND AMBIENT PRESSURE AS INFERRED FROM QUARTZ GAUGE MEASUREMENTS

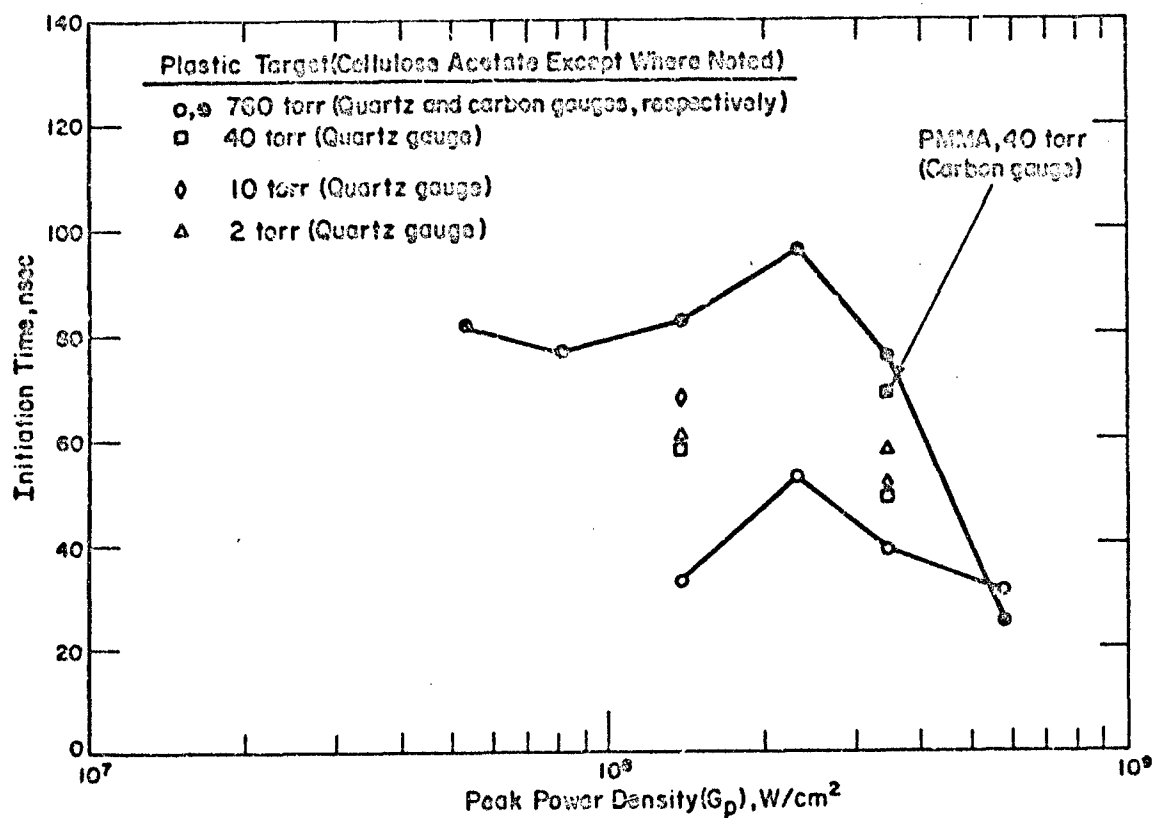


FIGURE 40. INITIATION TIME FOR PLASTIC TARGETS AS A FUNCTION OF PEAK POWER DENSITY AND AMBIENT PRESSURE AS INFERRED FROM QUARTZ AND CARBON GAUGE EXPERIMENTS

The change in initiation time with decreasing pressure is consistent with that observed in Reference (3). The disagreement between the absolute values of initiation time determined by the pressure records and previous methods is not understood, but may have resulted from uncertainties in property data used in the delay calculation. For nonmetallic targets, the initiation times are approximately 20-30 nsec longer than with aluminum targets for the same experimental conditions as shown in Figure 40. For the case of cellulose acetate, this result is consistent with the previous section (55 nsec at  $2.14 \times 10^8$  watt/cm<sup>2</sup>). Differences between carbon and quartz gauge measurements for an ambient pressure of 760 torr are also shown. As with metallic targets, the initiation times increase with decreasing ambient pressure. Most interesting is the behavior of initiation time with peak power density. The time of arrival of the pressure pulse actually increases slightly with increasing intensity until the LSD-initiation threshold is reached ( $\approx 1.6 \times 10^8$  watt/cm<sup>2</sup> for cellulose acetate). The initiation time then drops rapidly with increasing intensity. This may indicate breakdown in the very early stages of vaporization.

## V - CONCLUSIONS AND RECOMMENDATIONS

The primary conclusion from the research conducted in this program is that the experimental data on practical aluminum surfaces irradiated with 10.6- $\mu$  TEA laser pulses are most consistent with an initiation model wherein surface-emitted priming electrons are heated by inverse-bremsstrahlung absorption in the field of the neutral air molecules to the point where a nonequilibrium air-breakdown cascade occurs. Thermionic emission (or field emission at high peak-power density) at surface features is believed to be the process of free electron production at a large number of local initiation sites ( $\approx 10^4$  per  $\text{cm}^2$ ). The individual LSD plasmas are believed to "link up" as they move away from the surface and spread laterally although the latter process has not been studied extensively. Specific conclusions drawn from the research are listed below under the various areas of investigation.

### LSD-Wave Initiation on Metallics

- LSD-wave initiation for 10.6- $\mu$  TEA laser pulses is a local phenomenon apparently occurring at surface features such as laminations and pits.
- Initiation on practical aluminum surfaces at atmospheric pressure is prompt (30-60 nsec) with breakdown coming after a constant energy deposition of order  $1.7 \text{ J/cm}^2$ .
- Contaminants and oxide layers are not necessary for prompt initiation.
- A significant negative-charge emission, presumably electron emission, occurs prior to breakdown.
- There is no anomalous incidence angle effect on LSD-wave initiation.
- LSD-wave threshold at 10.6  $\mu$  for a smooth (but nonideal) copper surface was found to be  $2.3 \times 10^8 \text{ watt/cm}^2$ , which is considerably higher than that for a practical copper surface ( $.8 \times 10^8 \text{ watt/cm}^2$ ).

- Breakdown time is longer for a smooth copper surface than that for a practical aluminum surface.
- Hot spots occur on smooth surfaces, but are relatively few in number.
- On practical aluminum surfaces first appearance of bremsstrahlung radiation is consistent with other measurements of breakdown time.
- Nonequilibrium heating processes occur at early times as indicated by a delay between appearance of the bremsstrahlung and the NII radiation (130 nsec).
- No evidence has been found for the presence of ionized aluminum at atmospheric pressure, but a late-time neutral vapor cloud forms which radiates for as long as 200 microseconds.
- Ionized aluminum species (Al II and Al III) have been observed to appear 300-700 nsec after the beginning of the pulse for irradiations in air at pressures below the pressure threshold for LSD-wave initiation ( $\approx 10$  torr), but are not detectable at higher pressures.
- The initiation mechanism operative for practical aluminum surfaces is generally applicable to practical metallic surfaces (including tungsten, lead, copper, and zinc), although initiation times vary.
- Small amounts of neutral target vapor have been observed (without time-resolution) for all metals in atmospheric pressure irradiations.
- LSD-wave initiation on aluminum at  $1.06 \mu$  is dominated by breakdown in the vapor, although emission of electrons is observed and may play some role.

#### LSD-Wave Initiation on Nonmetallics

- Initiation of LSD-waves by 10.6- $\mu$  TEA laser pulses on acrylic plastic, fused silica, and polyimide occurs at local initiation sites with site densities two orders of magnitude less than that for metallic surfaces.
- The initiation sites are characterized by unvaporized "protected" areas often having embedded debris remnants and interference-fringe damage patterns. Purposely, embedded aluminum particles were found to produce the same type of pattern and a metallic-type LSD-wave initiation mechanism is believed to be operative.
- The initiation time for acrylic plastic was found to be similar to that for aluminum.
- Experimental results for cellulose acetate, phenolic resin, and alumina were found to be consistent with vapor heating and breakdown.
- The initiation time measured for cellulose acetate was considerably longer than that for aluminum at the same intensity (55 nsec as opposed to 33 nsec at  $2.1 \times 10^8$  watt/cm<sup>2</sup>).

#### LSD-Wave-Induced Pressure Response

- At low ambient air pressure, the effect of the introduction of an LSD wave on aluminum is an increase in pressure pulse risetime and a decrease in peak pressure. As ambient pressure is increased, the peak pressure response rises approximately in accordance with the blast-wave theory.
- Measured peak pressure levels are lower than predicted as would be expected for local initiation and a short pulse width.

- Radial pressure profiles measured for aluminum are in reasonable agreement with blast wave theory provided an appropriate effective spot radius is selected.
- Kilobar level pressures were produced in cellulose acetate targets by a vaporization contribution to the response. LSD-wave initiation at high intensity reduced the peak pressure significantly by retarding vaporization.
- LSD-wave initiation times inferred from the pressure data were in reasonable agreement with values determined by other methods.

While a fairly good understanding is in hand for initiation of LSD waves on metallic materials with 10.6- $\mu$  TEA laser pulses, a broader understanding of the various phenomena occurring at early times is believed essential to the development of the total picture of response of materials to pulsed lasers. In particular, it is recommended that future research efforts on LSD-wave initiation be directed toward additional detailed studies in the following areas.

- Wavelength and pulse risetime effects on initiation time
- Physics of metal vapor breakdown
- Liquid state reflectivity of metals
- Physics of thermionic emission into a background gas
- Nonmetallic initiation.

It is further recommended that existing theoretical models be utilized over a broader range of laser beam parameters and that the output be adjusted to provide predictions of variables which can be measured experimentally.

#### REFERENCES

- (1) C. T. Walters and R. H. Barnes, "An Investigation of Mechanisms of Initiation of Laser-Supported Absorption (LSA) Waves", Semiannual Report for the period April 23-October 22, 1973, Contract No. DAAH01-73-C-0776, Battelle-Columbus Laboratories (November, 1973).
- (2) C. T. Walters and R. H. Barnes, "An Investigation of Mechanisms of Initiation of Laser-Supported Absorption (LSA) Waves", Semiannual Report for the period October 23, 1973-June 30, 1974, Contract No. DAAH01-73-C-0776, Battelle-Columbus Laboratories (June, 1974).
- (3) C. T. Walters, R. H. Barnes, and R. E. Beverly III, "An Investigation of Mechanisms of Initiation of Laser-Supported Absorption (LSA) Waves", Semiannual Report for the period July 15, 1974-January 14, 1975, Contract No. DAAH01-73-C-0776, Battelle-Columbus Laboratories (January, 1975).
- (4) S. A. Ramsden and P. Savic, *Nature* 203, 1217 (1964).
- (5) Yu. P. Raizer, *Sov. Phys. JETP* 21, 1009 (1965).
- (6) J. W. Daiber and H. M. Thompson, *Phys. Fluids* 10, 1162 (1967).
- (7) P. E. Nielsen, and C. H. Canavan, "Ignition Conditions for Detonation Waves in Laser-Target Interaction", *Laser Division Digest, LRD-71-2*, Air Force Weapons Laboratory, December, 1971, p 123.
- (8) C. T. Walters, "Study of Initiation of Laser-Supported Detonation Waves", Technical Brief, Battelle-Columbus Laboratories, March, 1972.
- (9) C. T. Walters, "Studies in Strategic Technology", Monthly Management Report No. 20 on Contract DAAH01-71-C-0968, Battelle-Columbus Laboratories, December 8, 1972.
- (10) R. B. Hall, Boeing Aerospace Corporation, Private Communication, August, 1972.
- (11) H. M. Musal, Lockheed Missile and Space Company, Private Communication, December, 1972.
- (12) A. A. Boni, Systems, Science and Software, Private Communication, December, 1972.
- (13) A. L. Stoessell, ARPA, Private Communication, December, 1972.
- (14) B. Steverding, *J. Appl. Phys.* 45, 3507 (1974).



- (15) A. J. Barabukhov, F. V. Denkin, V. I. Kono, and A. A. Lyubin, Sov. Phys. JETP 30, 469 (1974).
- (16) W. E. Maher, R. B. Hall, and R. R. Johnson, J. Appl. Phys. 45, 2138 (1974).
- (17) A. Edwards, N. Ferriter, J. A. Fleck, Jr., and A. M. Winslow, "A Theoretical Description of the Interaction of a Pulsed Laser and a Target in an Air Environment", UCRL-51489, Lawrence Livermore Laboratory (November 26, 1973).
- (18) P. D. Thomas and H. M. Musal, "A Theoretical Study of Laser-Target Interaction", First Semiannual Technical Report on Contract No. DAAN01-72-C-0930, Lockheed Missiles and Space Company (December 22, 1972).
- (19) P. D. Thomas and H. M. Musal, "A Theoretical Study of Laser-Target Interaction", Final Technical Report on Contract No. DAAN01-73-C-0930, Lockheed Missiles and Space Company (August 31, 1973).
- (20) P. D. Thomas, H. M. Musal, and Y. S. Chou, "Laser Beam Interaction Part II", LMSC-D401354, Lockheed Missiles and Space Company (April, 1974).
- (21) P. D. Thomas and H. M. Musal, "A Theoretical Study of Laser-Target Interaction", Final Technical Report on Contract No. DAAN01-73-C-0930, Lockheed Missiles and Space Company (August, 1974).
- (22) H. S. Carslaw and J. C. Jaeger, Conduction of Heat in Solids, Oxford University Press (1959).
- (23) T. J. Weiting and J. T. Schriempf, "Free-Electron Theory and Laser Interactions with Metals", NRL Progress, June, 1972.
- (24) V. J. Bergel'son, A. P. Golub', I. B. Nemchinov, and S. P. Popov, Sov. J. Quant. Electron. 3, 289 (1974).
- (25) R. R. Rudder, Private Communication, August, 1973.
- (26) P.S.P. Wei and R. H. Hall, J. Appl. Phys. 44, 2311 (1973).
- (27) C. T. Walters, Appl. Phys. Letters 25, 696 (1974).
- (28) D. W. Gregg and S. J. Thomas, J. Appl. Phys. 37, 2787 (1966).
- (29) N. C. Anderholm, Appl. Phys. Letters 16, 113 (1970).
- (30) F. Neuman, Appl. Phys. Letters 4, 167 (1964).
- (31) C. H. Skeen and C. M. York, Appl. Phys. Letters 12, 369 (1968).

- (32) P. S. Eacey, E. D. Jones, J. C. Bushnell, and G. W. Gobeli, Appl. Phys. Letters 16, 120 (1970).
- (33) E. D. Jones, Appl. Phys. Letters 18, 33 (1971).
- (34) R. R. Rudder, Air Force Weapons Laboratory Laser Digest, Report No. LRD-71-2, 1971, p 148 (unpublished).
- (35) R. R. Rudder, J. A. Howland, and A. L. Augustoni, Air Force Weapons Laboratory Laser Digest, Report No. AFWL-Tr-72-243, 1972, p 92 (unpublished).
- (36) R. R. Rudder, Air Force Weapons Laboratory Laser Digest, Report No. AFWL-TR-73-273, 1973, p 137 (unpublished).
- (37) R. R. Rudder, Air Force Weapons Laboratory Laser Digest, Report No. AFWL-TR-74-241, 1974, p 135 (unpublished).
- (38) S. A. Metz, Appl. Phys. Letters 22, 211 (1973).
- (39) A. N. Pirri, R. Schlier, and D. Northam, Appl. Phys. Letters 21, 79 (1972).
- (40) J. F. Ready, Appl. Phys. Letters 25, 558 (1974).
- (41) R. W. O'Neil, L. C. Marquet, J. E. Lowder, D. E. Lencioni, C. W. Kilcline, H. Kleiman, and T. W. Hilton, MIT Lincoln Laboratory Report No. LTP-17, 1972 (unpublished).
- (42) J. E. Lowder, D. E. Lencioni, T. W. Hilton, and R. J. Hull, J. Appl. Phys. 44, 2759 (1973).
- (43) J. E. Lowder and L. C. Pattingill, Appl. Phys. Letters 24, 204 (1974).
- (44) L. R. Hettche, J. T. Schriempf, and R. L. Stegman, J. Appl. Phys. 44, 4079 (1973).
- (45) R. L. Stegman, J. T. Schriempf, and L. R. Hettche, J. Appl. Phys. 44, 3675 (1973).
- (46) S. A. Metz, L. R. Hettche, R. L. Stegman, and J. T. Schriempf, J. Appl. Phys. 46, 1634 (1975).
- (47) B. S. Holmes, Stanford Research Institute, Monthly Report No. 10 on Contract F29601-74-C-0051, ARPA Order No. 1905, 1975 (unpublished).
- (48) S. Marcus and J. E. Lowder, J. Appl. Phys. 46, 2293 (1975).
- (49) A. N. Pirri, Phys. Fluids 16, 1435 (1973).

- (50) P. E. Nielsen and G. H. Canavan, Air Force Systems Command Technical Report No. AFSC-TR-73-003, Vol. I, 1973 (unpublished).
- (51) P. E. Nielsen, Air Force Weapons Laboratory Laser Digest, Report No. AFWL-TR-73-273, 1973, p 102 (unpublished).
- (52) G. H. Canavan, P. E. Nielsen, and R. D. Harris, Air Force Weapons Laboratory Laser Digest, Report No. LRD-72-1, 1972, p 125 (unpublished).
- (53) P. E. Nielsen, Air Force Weapons Laboratory Laser Digest, Report No. AFWL-TR-72-243, 1972, p 97 (unpublished).
- (54) P. E. Nielsen, Air Force Weapons Laboratory Laser Digest, Report No. AFWL-TR-73-131, 1973, p 173 (unpublished).
- (55) P. E. Nielsen, Air Force Weapons Laboratory Laser Digest, Report No. AFWL-TR-74-241, 1974, p 150 (unpublished).
- (56) P. E. Nielsen, J. Appl. Phys. (to be published).
- (57) A. Edwards, N. Ferriter, J. A. Fleck, Jr., and A. H. Winslow, Lawrence Livermore Laboratory Report No. UCRL-51489, 1973 (unpublished).
- (58) A. W. Blackstock, H. R. Kratz, M. B. Feenay, Rev. Sci. Instr. 35, 105 (1964).
- (59) R. A. Graham, J. Appl. Phys. 46, 1901 (1975).
- (60) J. A. Charest, Dynasen, Inc., Private Communication.
- (61) B. J. Kohn, Air Force Weapons Laboratory Report No. AFWL-TR-69-38, 1969 (unpublished).
- (62) Y. P. Raizer, Sov. Phys. JETP 21, 1009 (1965).
- (63) M. P. Felix, Rev. Sci. Instrum. 45, 1106 (1974).

## APPENDIX A

### TIME-INTEGRATED SPECTRA

Time-integrated spectra are presented here for emissions from type 2024 aluminum alloy targets irradiated in air, nitrogen, and helium, and from copper, zinc, tungsten, and lead targets irradiated in nitrogen. Gas pressures ranged from one atmosphere down to vacuum pressures of less than  $1 \times 10^{-5}$  torr. The irradiations were performed using a  $10.6 \mu$   $\text{CO}_2$  TEA laser at peak intensities ranging from  $5.35 \times 10^8$  down to about  $2.94 \times 10^7$  watt/cm<sup>2</sup>.

A-2



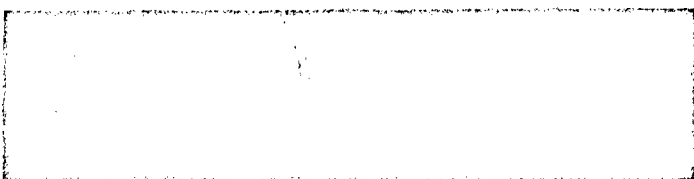
(a)  
1 atm  
 $G_p = 7.49 \times 10^7 \text{ watt/cm}^2$



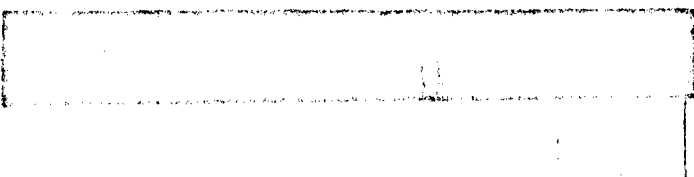
(b)  
100 torr  
 $G_p = 1.28 \times 10^8 \text{ watt/cm}^2$



(c)  
2 torr  
 $G_p = 3.21 \times 10^8 \text{ watt/cm}^2$



(d)  
2 torr  
 $G_p = 2.14 \times 10^8 \text{ watt/cm}^2$



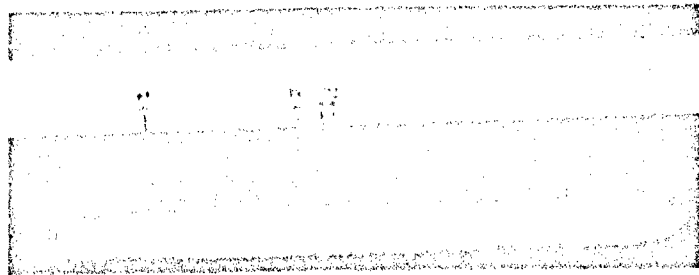
(e)  
 $1 \times 10^{-5} \text{ torr}$   
 $G_p = 3.21 \times 10^8 \text{ watt/cm}^2$

3400 3300 3200 3100 3000 2900 2800 2700 2600 2500 Å

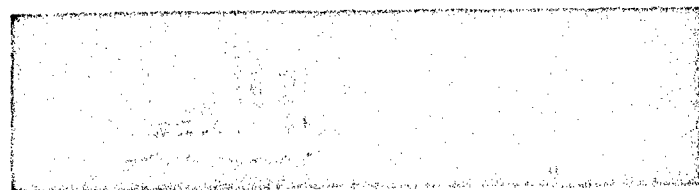
Wavelength, Å

FIGURE A-1. SPECTRA COVERING RANGE FROM 2450 TO 3350 Å  
FOR ALUMINUM TARGET IN DRY AIR

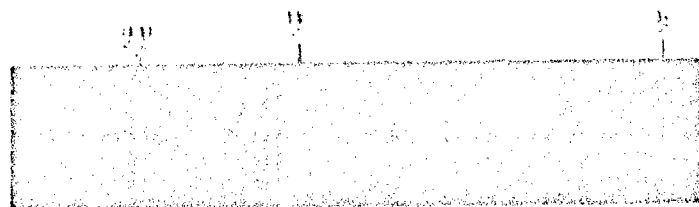
A-3



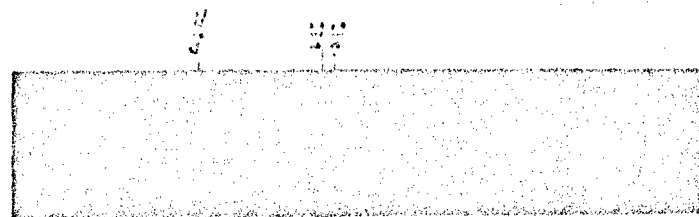
(a)  
1 atm  
 $G_p = 5.35 \times 10^8 \text{ watt/cm}^2$



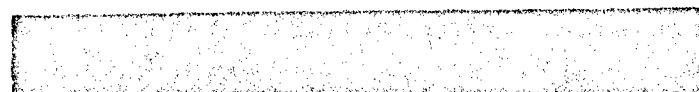
(b)  
100 torr  
 $G_p = 2.14 \times 10^8 \text{ watt/cm}^2$



(c)  
10 torr  
 $G_p = 1.28 \times 10^8 \text{ watt/cm}^2$



(d)  
2 torr  
 $G_p = 3.21 \times 10^8 \text{ watt/cm}^2$

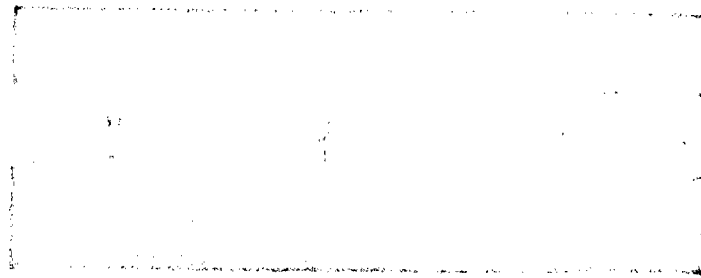


(e)  
 $1 \times 10^{-5} \text{ torr}$   
 $G_p = 3.21 \times 10^8 \text{ watt/cm}^2$

4400 4300 4200 4100 4000 3900 3800 3700 3600 3500 34  
Wavelength, Å

FIGURE A-2. SPECTRA COVERING RANGE FROM 3450 TO 4350 Å  
FOR ALUMINUM TARGET IN DRY AIR

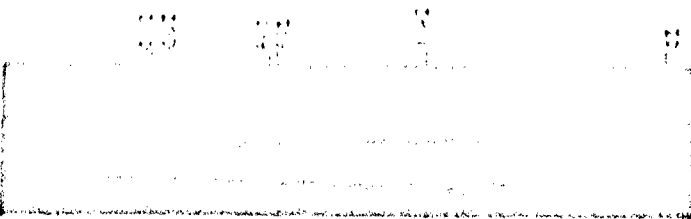
A-4



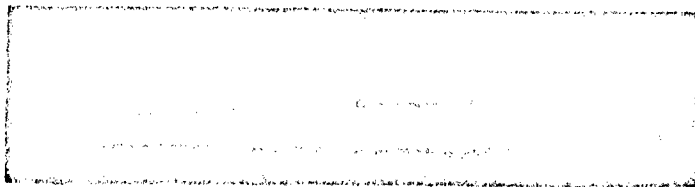
(a)  
1 atm  
 $G_p = 5.35 \times 10^8 \text{ watt/cm}^2$



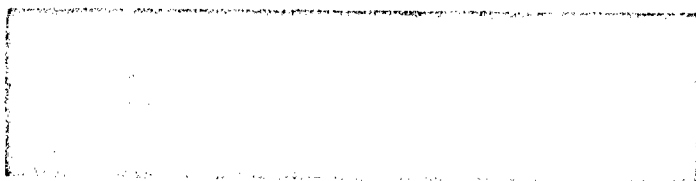
(b)  
10 torr  
 $G_p = 5.35 \times 10^8 \text{ watt/cm}^2$



(c)  
2 torr  
 $G_p = 5.35 \times 10^8 \text{ watt/cm}^2$



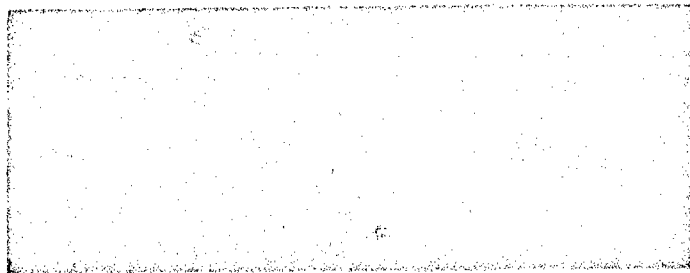
(d)  
 $<1 \times 10^{-5} \text{ torr}$   
 $G_p = 5.35 \times 10^8 \text{ watt/cm}^2$



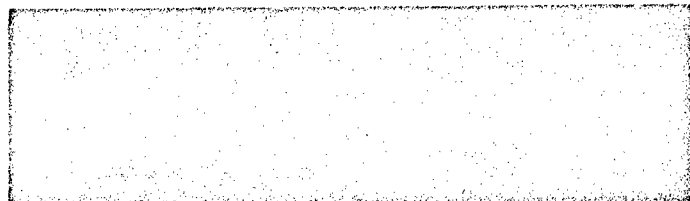
(e)  
1 atm  
 $G_p = 4.92 \times 10^7 \text{ watt/cm}^2$

Wavelength, Å

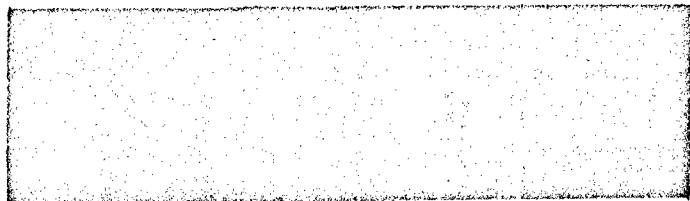
FIGURE A-3. SPECTRA COVERING RANGE FROM 2450 TO 3350Å  
FOR ALUMINUM TARGET IN NITROGEN



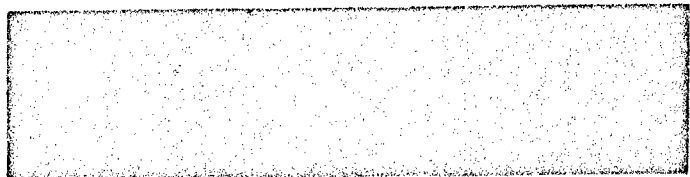
(f)  
10 torr  
 $G_p = 2.14 \times 10^8 \text{ watt/cm}^2$



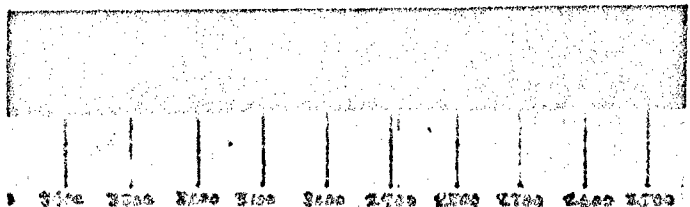
(g)  
2 torr  
 $G_p = 3.21 \times 10^8 \text{ watt/cm}^2$



(h)  
 $< 1 \times 10^{-5} \text{ torr}$   
 $G_p = 3.21 \times 10^8 \text{ watt/cm}^2$



(i)  
1 atm  
 $G_p = 2.94 \times 10^7 \text{ watt/cm}^2$



Wavelength, Å

(j)  
2 torr  
 $G_p = 2.14 \times 10^8 \text{ watt/cm}^2$

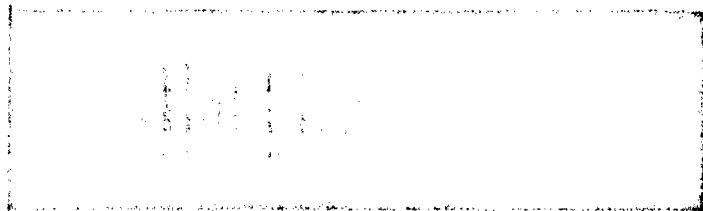
FIGURE A-3. (CONTINUED)



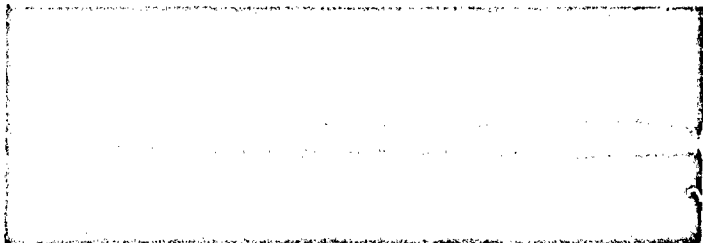
A-6



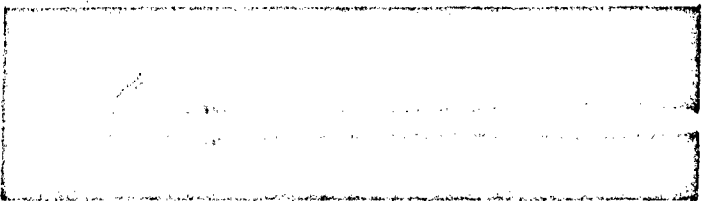
(a)  
1 atm  
 $G_p = 5.35 \times 10^8 \text{ watt/cm}^2$



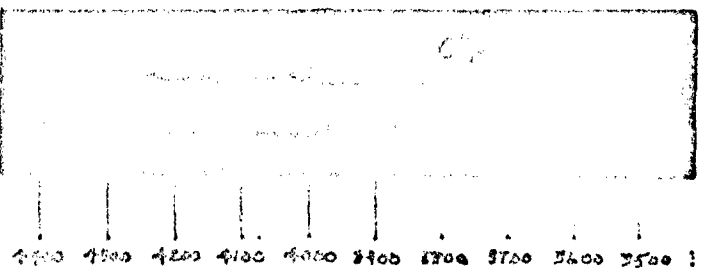
(b)  
10 torr  
 $G_p = 5.35 \times 10^8 \text{ watt/cm}^2$



(c)  
2 torr  
 $G_p = 5.35 \times 10^8 \text{ watt/cm}^2$



(d)  
 $< 1 \times 10^{-5} \text{ torr}$   
 $G_p = 5.35 \times 10^8 \text{ watt/cm}^2$

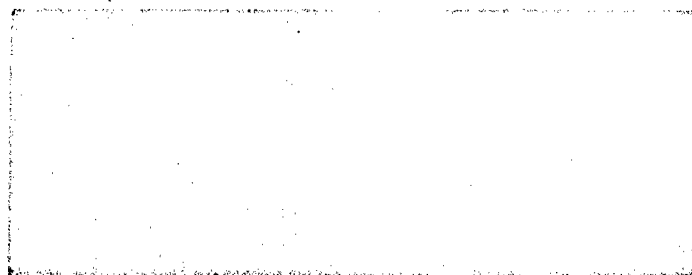


(e)  
1 atm  
 $G_p = 7.49 \times 10^7 \text{ watt/cm}^2$

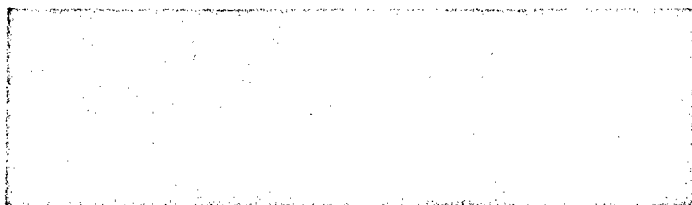
4350 4300 4250 4200 4150 4100 4050 4000 3950 3900 3850 3800 3750 3700 3650 3600 3550  
Wavelength, Å

FIGURE A-4. SPECTRA COVERING RANGE FROM 3450 TO 4350 Å  
FOR ALUMINUM TARGET IN NITROGEN

A-7



(f)  
10 torr  
 $G_p = 1.23 \times 10^8 \text{ watt/cm}^2$



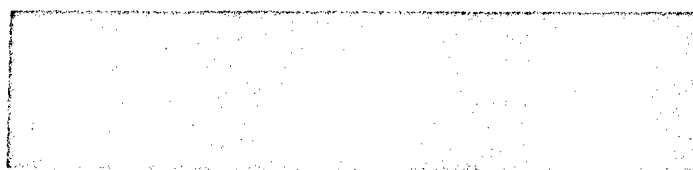
(g)  
2 torr  
 $G_p = 3.21 \times 10^8 \text{ watt/cm}^2$



(h)  
 $< 1 \times 10^{-5} \text{ torr}$   
 $G_p = 3.21 \times 10^8 \text{ watt/cm}^2$



(i)  
1 atm  
 $G_p = 2.94 \times 10^7 \text{ watt/cm}^2$

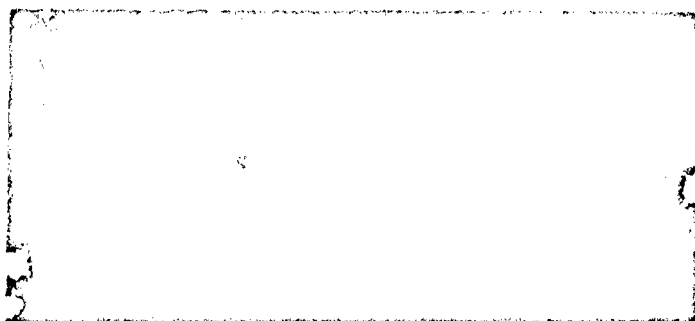


(j)  
2 torr  
 $G_p = 2.14 \times 10^8 \text{ watt/cm}^2$

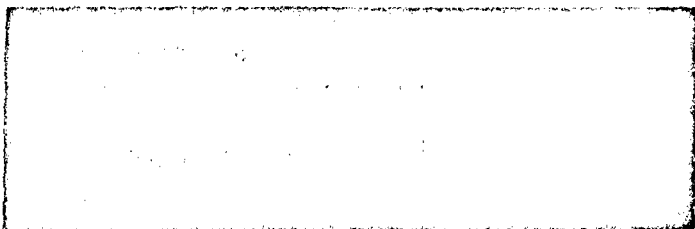
4100 4150 4200 4250 4300 4350 4400 4450 4500 4550 4600  
Wavelength, Å

FIGURE A-4. (CONTINUED)

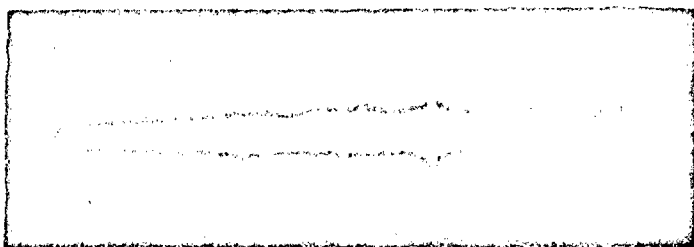
A-8



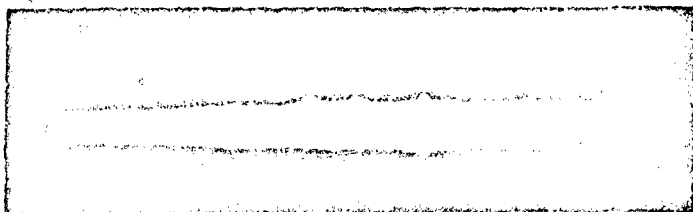
(a)  
1 atm  
 $G_p = 5.35 \times 10^8 \text{ watt/cm}^2$



(b)  
100 torr  
 $G_p = 5.35 \times 10^8 \text{ watt/cm}^2$



(c)  
10 torr  
 $G_p = 5.35 \times 10^8 \text{ watt/cm}^2$



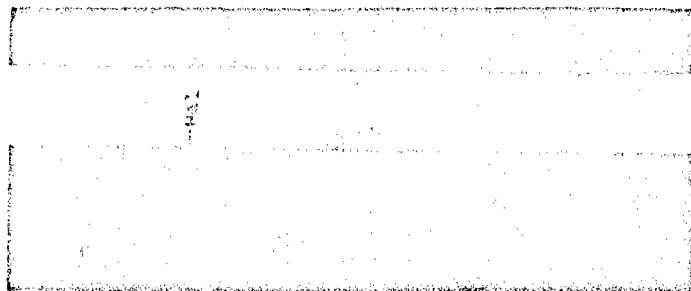
(d)  
2 torr  
 $G_p = 5.35 \times 10^8 \text{ watt/cm}^2$

3350 3300 3250 3200 3150 3100 3050 3000 2950 2900 2850 2800 2750 2700 2650 2600 2550 2500 2450

Wavelength, Å

FIGURE A-5. SPECTRA COVERING RANGE FROM 2450 TO 3350 Å  
FOR ALUMINUM TARGET IN HELIUM

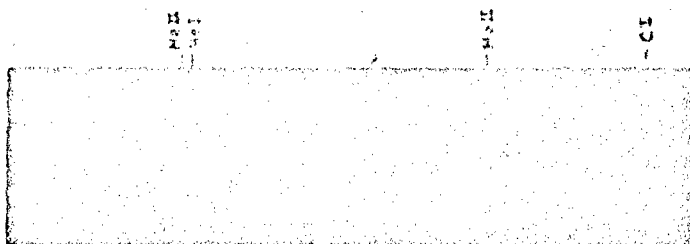
A-9



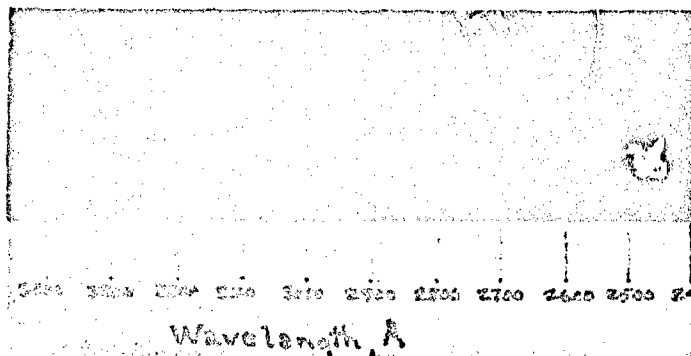
(e)  
1 atm  
 $G_p = 4.92 \times 10^7 \text{ watt/cm}^2$



(f)  
100 torr  
 $G_p = 2.14 \times 10^8 \text{ watt/cm}^2$

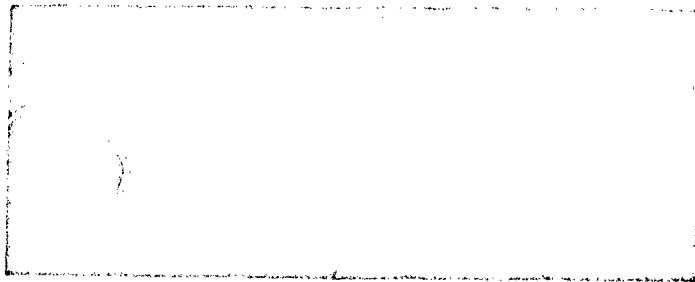


(g)  
10 torr  
 $G_p = 3.21 \times 10^8 \text{ watt/cm}^2$

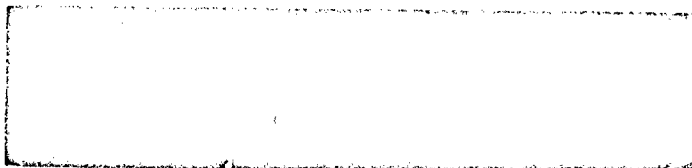


(h)  
2 torr  
 $G_p = 3.21 \times 10^8 \text{ watt/cm}^2$

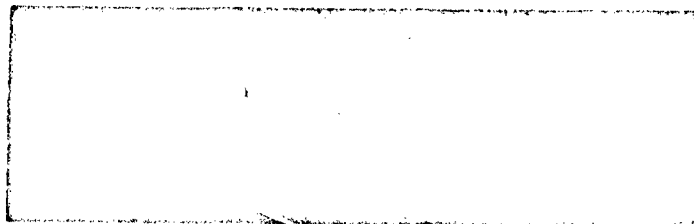
FIGURE A-5. (CONTINUED)



(i)  
100 torr  
 $G_p = 7.49 \times 10^7 \text{ watt/cm}^2$



(j)  
10 torr  
 $G_p = 2.14 \times 10^8 \text{ watt/cm}^2$

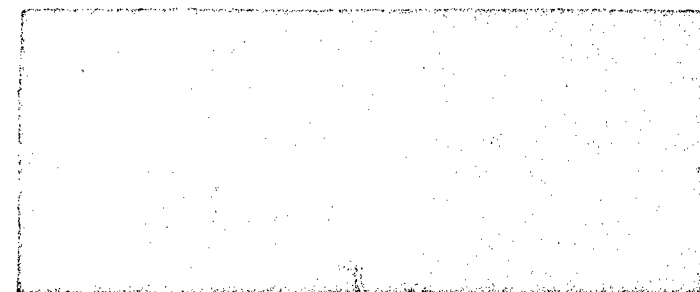


(k)  
2 torr  
 $G_p = 2.14 \times 10^8 \text{ watt/cm}^2$

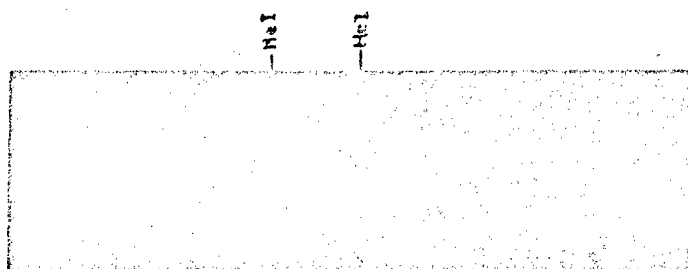
3400 3300 3200 3100 3000 2900 2800 2700 2600 2500 2400

Wavelength, Å

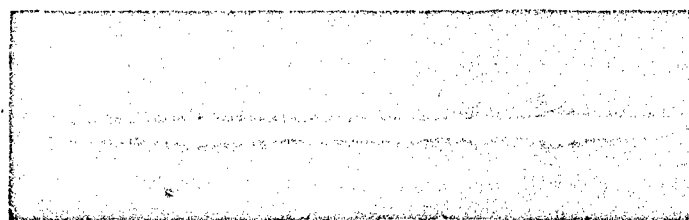
FIGURE A-5. (CONTINUED)



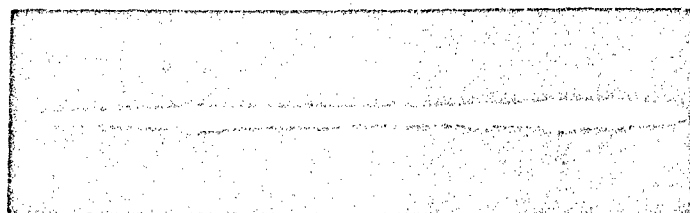
(a)  
1 atm  
 $G_p = 3.21 \times 10^8 \text{ watt/cm}^2$



(b)  
100 torr  
 $G_p = 5.35 \times 10^8 \text{ watt/cm}^2$



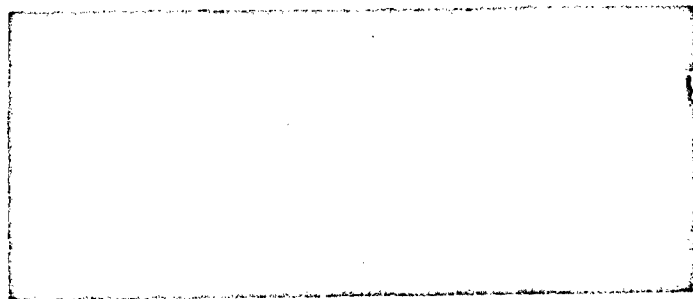
(c)  
10 torr  
 $G_p = 5.35 \times 10^8 \text{ watt/cm}^2$



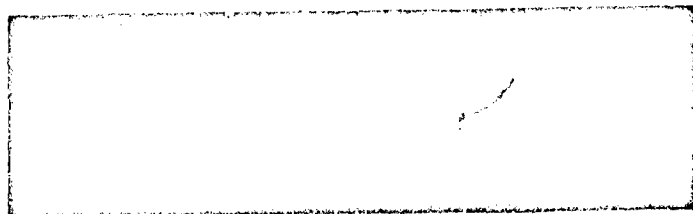
(d)  
2 torr  
 $G_p = 5.35 \times 10^8 \text{ watt/cm}^2$

4350 4300 4250 4200 4150 4100 4050 4000 3950 3900 3850 3800 3750 3700 3650 3600 3550 3500 3450  
Wavelength, Å

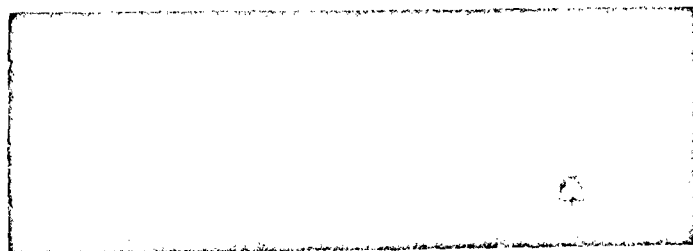
FIGURE A-6. SPECTRA COVERING RANGE FROM 3450 TO 4350 Å  
FOR ALUMINUM TARGET IN HELIUM



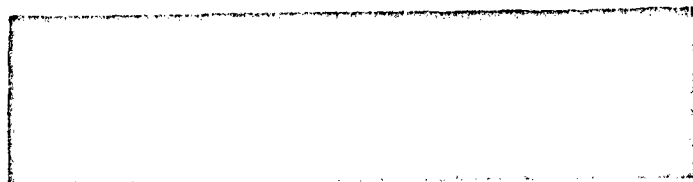
(e)  
1 atm  
 $G_p = 4.92 \times 10^7 \text{ watt/cm}^2$



(f)  
100 torr  
 $G_p = 2.14 \times 10^8 \text{ watt/cm}^2$



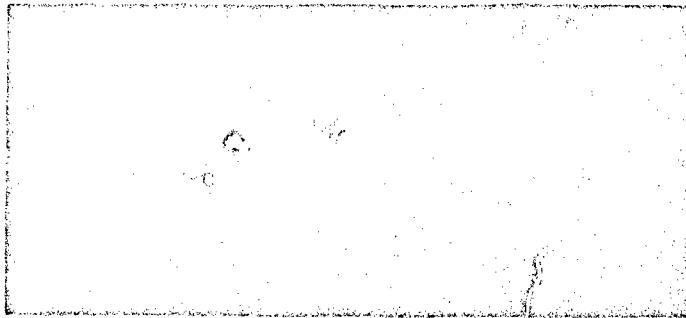
(g)  
10 torr  
 $G_p = 3.21 \times 10^8 \text{ watt/cm}^2$



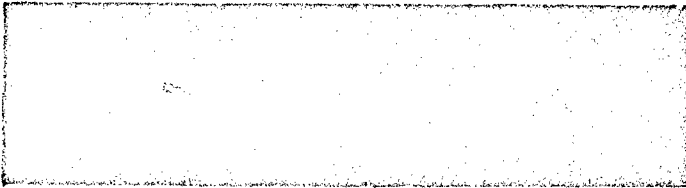
(h)  
2 torr  
 $G_p = 3.21 \times 10^8 \text{ watt/cm}^2$

4700 4600 4500 4400 4300 4200 4100 4000 3900 3800 3700 3600 3500 Å  
Wavelength, Å

FIGURE A-6. (CONTINUED)



(i)  
100 torr  
 $G_p = 1.28 \times 10^8 \text{ watt/cm}^2$



(j)  
100 torr  
 $G_p = 7.49 \times 10^7 \text{ watt/cm}^2$

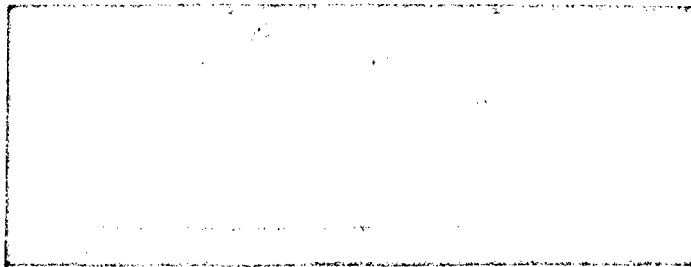


(k)  
10 torr  
 $G_p = 2.14 \times 10^8 \text{ watt/cm}^2$

4100 4150 4200 4250 4300 4350 4400 4450 4500 4550 4600 4650 4700 4750 4800  
Wavelength, Å

FIGURE A-6. (CONTINUED)





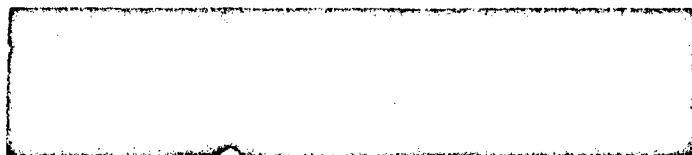
(a)  
1 atm  
 $G_p = 5.35 \times 10^8 \text{ watt/cm}^2$



(b)  
10 torr  
 $G_p = 1.28 \times 10^8 \text{ watt/cm}^2$

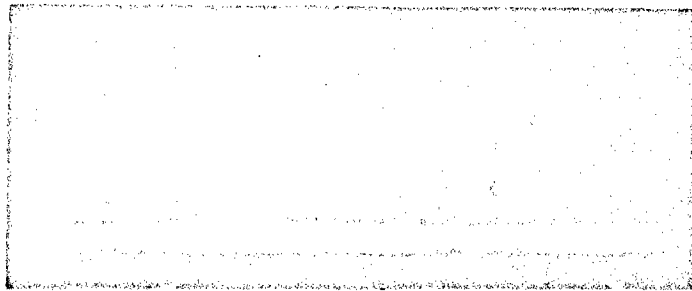


(c)  
2 torr  
 $G_p = 5.35 \times 10^8 \text{ watt/cm}^2$



(d)  
2 torr  
 $G_p = 3.21 \times 10^8 \text{ watt/cm}^2$

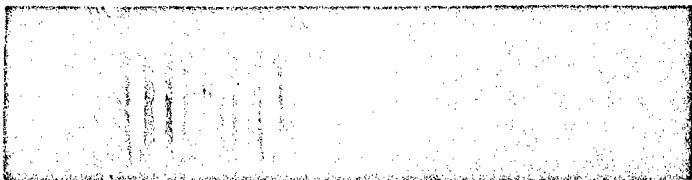
FIGURE A-7. SPECTRA COVERING RANGE FROM 2450 TO 3350 Å  
FOR COPPER TARGET IN NITROGEN



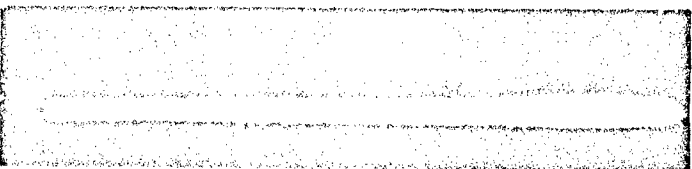
(a)  
1 atm  
 $G_p = 5.35 \times 10^8 \text{ watt/cm}^2$



(b)  
100 torr  
 $G_p = 1.28 \times 10^8 \text{ watt/cm}^2$

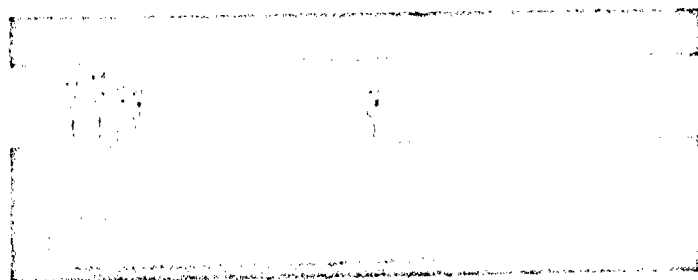


(c)  
10 torr  
 $G_p = 1.28 \times 10^8 \text{ watt/cm}^2$

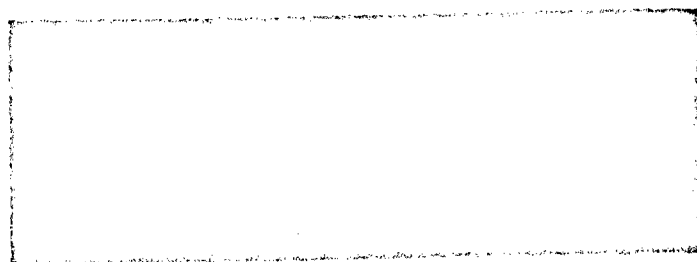


(d)  
2 torr  
 $G_p = 5.35 \times 10^8 \text{ watt/cm}^2$

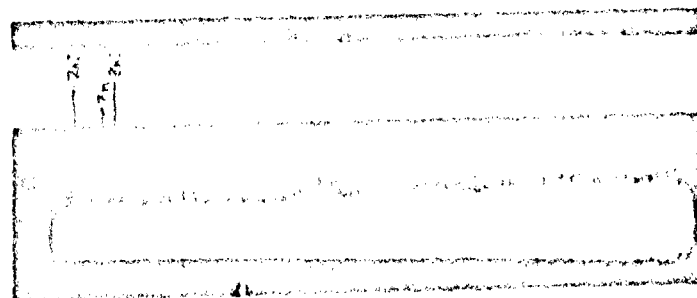
FIGURE A-8. SPECTRA COVERING RANGE FROM 3450 TO 4350 Å  
FOR COPPER TARGET IN NITROGEN



(a)  
1 atm  
 $G_p = 5.35 \times 10^8 \text{ watt/cm}^2$



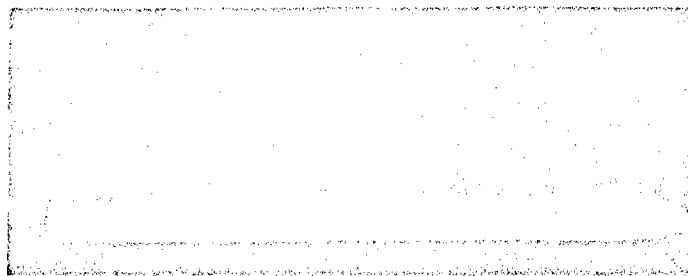
(b)  
100 torr  
 $G_p = 7.49 \times 10^7 \text{ watt/cm}^2$



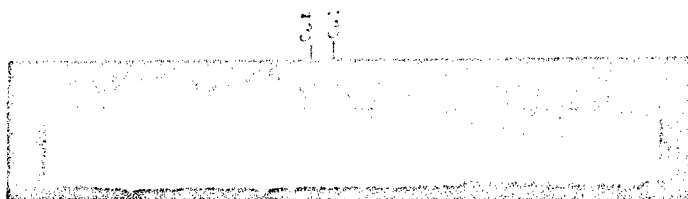
(c)  
2 torr  
 $G_p = 5.35 \times 10^8 \text{ watt/cm}^2$

FIGURE A-9. SPECTRA COVERING RANGE FROM 2450 TO 3350Å  
FOR ZINC TARGET IN NITROGEN

A-17



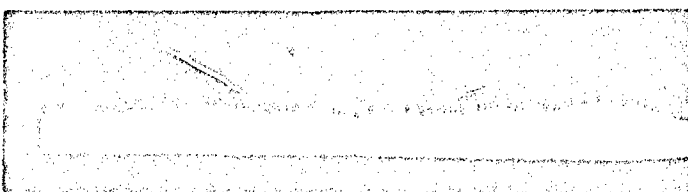
(a)  
1 atm  
 $G_p = 5.35 \times 10^8 \text{ watt/cm}^2$



(b)  
10 torr  
 $G_p = 5.35 \times 10^8 \text{ watt/cm}^2$



(c)  
10 torr  
 $G_p = 1.28 \times 10^8 \text{ watt/cm}^2$



(d)  
2 torr  
 $G_p = 5.35 \times 10^8 \text{ watt/cm}^2$

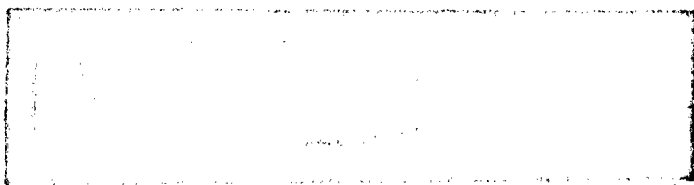
Wavelength A

FIGURE A-10. SPECTRA COVERING RANGE FROM 3450 TO 4350Å  
FOR ZINC TARGET IN NITROGEN

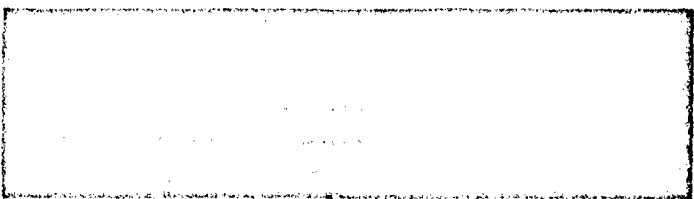
A-18



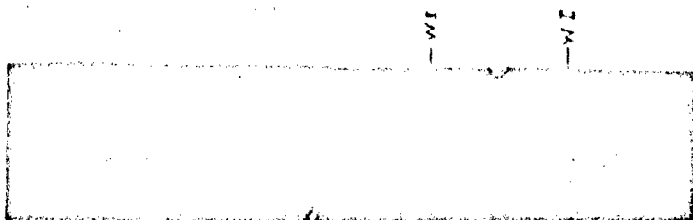
(a)  
1 atm  
 $G_p = 5.35 \times 10^8 \text{ watt/cm}^2$



(b)  
10 torr  
 $G_p = 5.35 \times 10^8 \text{ watt/cm}^2$



(c)  
2 torr  
 $G_p = 5.35 \times 10^8 \text{ watt/cm}^2$



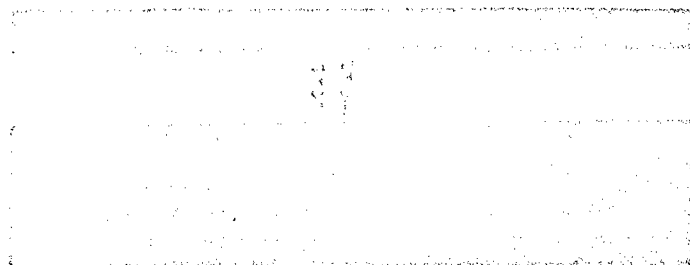
(d)  
 $< 1 \times 10^{-5} \text{ torr}$   
 $G_p = 5.35 \times 10^8 \text{ watt/cm}^2$



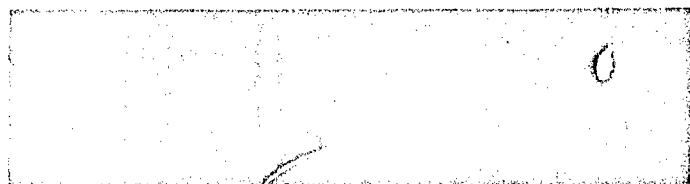
(e)  
 $< 1 \times 10^{-5} \text{ torr}$   
 $G_p = 3.21 \times 10^8 \text{ watt/cm}^2$

Wavelength, Å

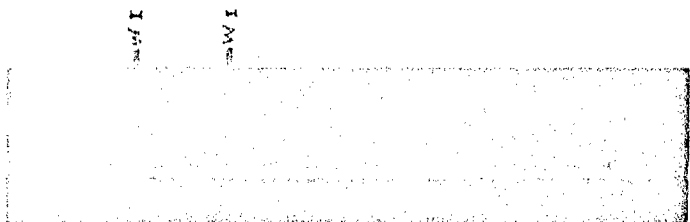
FIGURE A-11. SPECTRA COVERING RANGE FROM 2450 TO 3350Å  
FOR TUNGSTEN TARGET IN NITROGEN



(a)  
1 atm  
 $G_p = 3.21 \times 10^8 \text{ watt/cm}^2$



(b)  
10 torr  
 $G_p = 1.28 \times 10^8 \text{ watt/cm}^2$



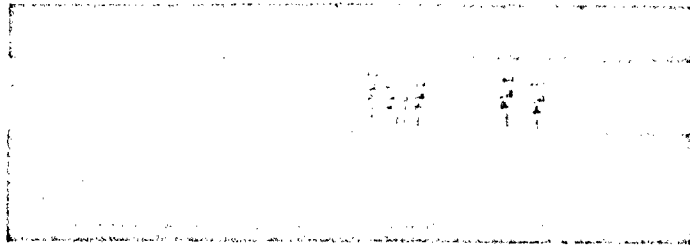
(c)  
2 torr  
 $G_p = 5.35 \times 10^8 \text{ watt/cm}^2$



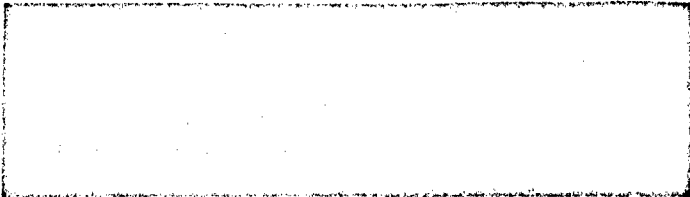
(d)  
2 torr  
 $G_p = 3.21 \times 10^8 \text{ watt/cm}^2$

Wavelength, Å

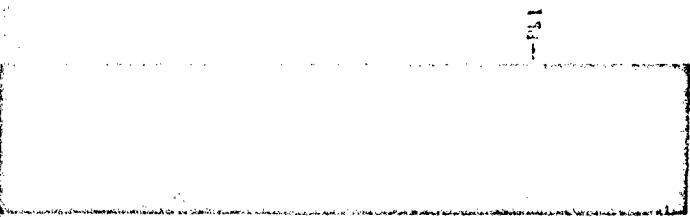
FIGURE A-12. SPECTRA COVERING RANGE FROM 3450 TO 4350 Å  
FOR TUNGSTEN TARGET IN NITROGEN



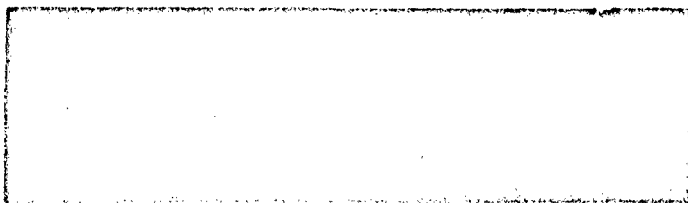
(a)  
1 atm  
 $G_p = 5.35 \times 10^8 \text{ watt/cm}^2$



(b)  
10 torr  
 $G_p = 2.14 \times 10^8 \text{ watt/cm}^2$



(c)  
10 torr  
 $G_p = 4.92 \times 10^7 \text{ watt/cm}^2$

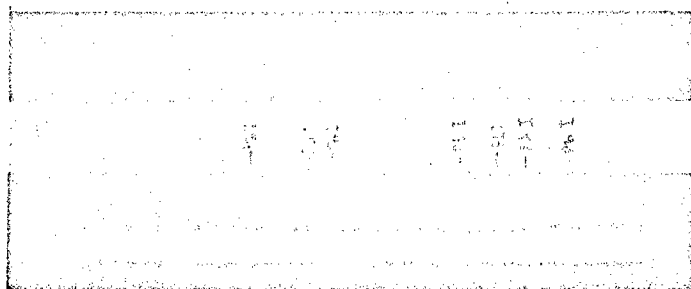


(d)  
<1 x 10<sup>-5</sup> torr  
 $G_p = 4.92 \times 10^7 \text{ watt/cm}^2$

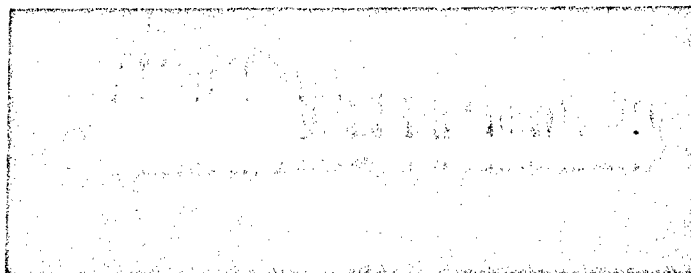
3300 3250 3200 3150 3100 3050 3000 2950 2900 2850 2800 2750 2700 2650 2600 2550 2500  
Wavelength, Å

FIGURE A-13. SPECTRA COVERING RANGE FROM 2450 TO 3350Å  
FOR LEAD TARGET IN NITROGEN

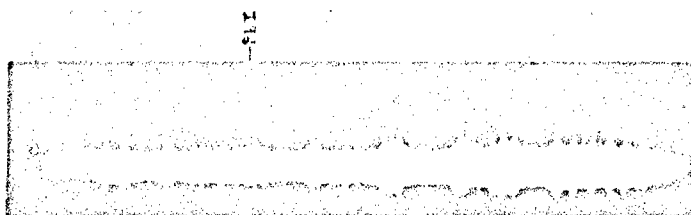
A-21



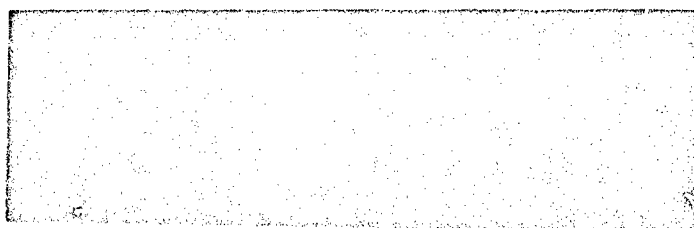
(a)  
1 atm  
 $G_p = 5.35 \times 10^8 \text{ watt/cm}^2$



(b)  
10 torr  
 $G_p = 3.21 \times 10^8 \text{ watt/cm}^2$



(c)  
2 torr  
 $G_p = 1.28 \times 10^8 \text{ watt/cm}^2$



(d)  
<  $1 \times 10^{-5}$  torr  
 $G_p = 4.92 \times 10^7 \text{ watt/cm}^2$

4350 4300 4250 4200 4150 4100 4050 4000 3950 3900 3850 3800 3750 3700 3650 3600 3550 3500 3450  
Wavelength, Å

FIGURE A-14. SPECTRA COVERING RANGE FROM 3450 TO 4350 Å  
FOR LEAD TARGET IN NITROGEN



END

DATE

FILMED

6-2-76

NTIS